

APPLICATION OF CuFe_2O_4 FOR PHOTOCATALYTIC FENTON DEGRADATION OF

GLYCEROL

KONG ZI YING

Thesis submitted in fulfilment of the requirements for the award of the degree of

Master of Engineering (Chemical)

UMP

Faculty of Chemical & Natural Resources Engineering

UNIVERSITI MALAYSIA PAHANG

AUGUST 2015

UNIVERSITI MALAYSIA PAHANG

DECLARATION OF THESIS COPYRIGHT

Author's full name : Kong Zi Ying

Date of birth : 18/09/1989

Title : Application of CuFe_2O_4 for Photocatalytic Fenton
Degradation of Glycerol

Academic Session : SEM II 2014/2015

I declare that this thesis is classified as:

CONFIDENTIAL (Contains confidential information under the Official Secret Act 1972)*

RESTRICTED (Contains restricted information as specified by the organization where research was done)

OPEN ACCESS I agree that my thesis to be published as online open access (full text)

I acknowledged that Universiti Malaysia Pahang reserves the right as follows

:

1. The thesis is the property of Universiti Malaysia Pahang.
2. The Library of Universiti Malaysia Pahang has the right to make copies for the purpose of research only.
3. The Library has the right to make copies of the thesis for academic exchange.

Certified by,

STUDENT SIGNATURE
KONG ZI YING
(890918-13-6102)
DATE: 22/8/2015

SIGNATURE OF SUPERVISOR
DR CHENG CHIN KUI
NAME OF SUPERVISOR
DATE: 22/8/2015

SUPERVISOR'S DECLARATION

We hereby declare that we have checked this thesis and in my opinion, this thesis is adequate in terms of scope and quality for the award of the degree of Master of Engineering (Chemical).

Signature :
Name of Supervisor : Cheng Chin Kui
Position : Associate Professor
Date : 22/8/2015

Signature :
Name of Co-supervisor: MD Maksudur Rahman Khan
Position : Associate Professor
Date : 22/8/2015

STUDENT'S DECLARATION

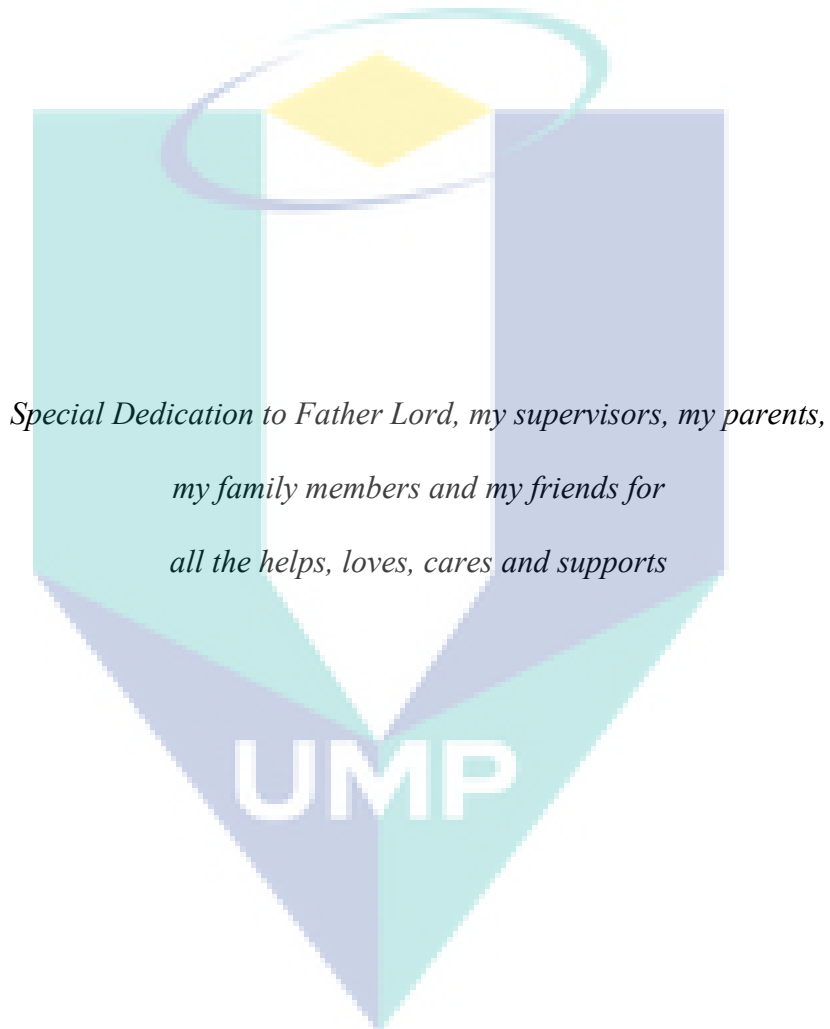
I hereby declare that the work in this thesis is my own except for quotations and summaries which have been duly acknowledged. The thesis has not been accepted for any degree and is not concurrently submitted for award of other degree.

Signature :
Name : Kong Zi Ying
ID Number : MKC13021
Date : 22/8/2015

The logo of Universiti Malaysia Perlis (UMP) is a large, stylized shield shape. It is divided into four quadrants: top-left is light blue, top-right is light purple, bottom-left is light purple, and bottom-right is light blue. The letters 'UMP' are written in white, bold, sans-serif font across the center of the shield.

UMP

DEDICATION



ACKNOWLEDGEMENTS

First and foremost, thanks to God for giving the strength and spirit which allows me to complete my master study in Chemical Engineering from Universiti Malaysia Pahang (UMP). Besides that, I would like to express my appreciation to Almighty God for giving me good health, strength and perseverance to complete this thesis.

In addition, I have been guided, helped and supported by many people, researchers and academicians in completing the research project and also during the thesis writing. My deepest appreciation goes to my supervisors, Dr Cheng Chin Kui and Dr. MD Maksudur Rahman Khan for their advice, guidance, and motivation throughout the preparation of this thesis and the research work. With their hands-on guidance, my master project was successfully completed culminating in this well-written thesis.

My sincere appreciation also extends to all the technical staffs in lab and many others who have provided assistance at various occasions during my experimental works. Their views and tips are helpful indeed, to improve the quality of my work.

Last but not least, I would also like to thank my lab mate, Bamidele Victor Ayodele for accompanying me to accomplish the research project, as well as providing me valuable suggestions, tips and helps during the research. Besides that, I also feel grateful towards my parents and family for their love and supporting me all the times. I would not be able to complete the work without their mental support and also words of encouragement. Finally, I would like to show my utmost gratitude to the Almighty God for giving me good health, strength, wisdom and perseverance to complete this thesis.

ABSTRACT

The liquid waste from biodiesel production contains primarily glycerol and requires treatment before discharge into waterway. This study reports on the glycerol decomposition using photocatalytic Fenton technique. Visible light-responsive CuFe_2O_4 photocatalyst was synthesized using a sol-gel method employing Cu:Fe ratio of 1:2 by mol. The photocatalyst was characterized using N_2 -physisorption, FESEM-EDX, XRD, UV-Vis DRS and particle size distribution. The BET specific surface area of CuFe_2O_4 was $102.4 \text{ m}^2/\text{g}$. The morphology of the CuFe_2O_4 showed irregularly-shaped nanoparticles with good homogeneity in particle size distribution. The results indicate that the solid catalyst exhibited high crystallinity with CuFe_2O_4 as the main crystallite compound. The band gap energy of the CuFe_2O_4 was 1.58 eV and the average particle size of the photocatalyst was around $100 \text{ }\mu\text{m}$. In the presence of xenon lamp (250 W), the performance of photocatalytic Fenton degradation of different concentrations of glycerol aqueous solution, different concentrations of hydrogen peroxide and different photocatalyst loadings were studied. The samples in the experiment were analysed using HPLC. The results showed that a minimal amount of photocatalyst loadings (0.1 g/L) was needed to initiate the photocatalytic Fenton reaction. By increasing the concentration of glycerol solution, the degradation of glycerol diminished; however increasing the concentration of H_2O_2 has increased the glycerol degradation. The degradation at initial glycerol concentration of 27.36 mM shows 60.0% while at 67.41 mM glycerol concentration shows 27.0%. Besides that, adding 819.5 mM H_2O_2 showed 30% degradation while adding 163.9 mM H_2O_2 only showed 5% degradation. In addition, statistical evaluation was also carried out to understand the significance of the kinetics results. Full factorial analysis was introduced to screen the factors in the photocatalytic Fenton degradation of glycerol. The best condition to show higher degradation rate were 27.41 mM glycerol concentration, 819.5 mM H_2O_2 concentration and 5.0 g/L photocatalyst loadings in the experiment of four hours. Glycerol concentration and concentration of H_2O_2 affect the glycerol decomposition.

ABSTRAK

Sisa cecair iaitu gliserol yang dihasil ketika penghasilan biodiesel memerlukan rawatan yang sewajarnya sebelum pembuangan. Kerja ini melaporkan penguraian gliserol dengan menggunakan teknik fotopemangkinan. CuFe_2O_4 fotomangkin yang responsif terhadap cahaya telah disintesis dengan menggunakan kaedah sol-gel dengan nisbah mol Cu:Fe 1:2. Kaedah penyerapan fizikal seperti N_2 -physisorption, FESEM-EDX, XRD, UV-Vis DRS dan taburan size zarah telah digunakan untuk menganalisis ciri-ciri fotopemangkin CuFe_2O_4 . Keluasan permukaan spesifik BET oleh CuFe_2O_4 adalah $102.4 \text{ m}^2/\text{g}$. Morfologi CuFe_2O_4 menunjukkan nanopartikel berbentuk tidak teratur dengan kehomogenan yang baik dalam taburan saiz zarah. Keputusan dari XRD menunjukkan bahawa CuFe_2O_4 adalah sebatian utama kristal. Tenaga jurang jalur daripada CuFe_2O_4 adalah 1.58 eV dan purata taburan size zarah adalah antara $100 \mu\text{m}$. Pengaruh dari kepekatan larutan akueus gliserol, kepekatan hidrogen peroksida dan kuantiti pemangkin terhadap prestasi degradasi fotopemangkinan-Fenton dalam kehadiran sinaran lampu xenon (250 W) telah dikaji. Sampel eksperimen diuji dengan menggunakan HPLC. Hasil kajian menunjukkan bahawa kuantiti fotopemangkin yang minima (0.1 g/L) diperlukan untuk memulakan tindak balas fotopemangkinan Fenton. Degradasi gliserol berkurang dengan penambahan kepekatan larutan gliserol, tetapi, peningkatan kepekatan H_2O_2 telah meningkatkan degradasi gliserol. Penggunaan kepekatan awal gliserol dengan 27.36 mM dan 67.41 mM membawa kepada 60% dan 27% degradasi, masing-masing. Di samping itu, penambahan $819.5 \text{ mM H}_2\text{O}_2$ menunjukkan degradasi gliserol sebanyak 30% manakala penambahan $163.9 \text{ mM H}_2\text{O}_2$ hanya menunjukkan degradasi 5% . Selain itu, analisis statistik juga dilaksanakan untuk mengetahui kepentingan dalam kinetic data tindakbalas kimia yang diperolehi. Analisis faktorial penuh telah diperkenalkan untuk mengkaji faktor-faktor dalam degradasi gliserol. Hasil kerja ini menunjukkan bahawa keadaan dimana kepekatan gliserol pada 27.41 mM , kepekatan H_2O_2 pada 819.5 mM dan kuantiti fotopemangkin pada 5.0 g/L adalah terbaik untuk kadar degradasi gliserol yang tinggi dalam eksperimen selama empat jam. Kesimpulannya, penguraian gliserol akan dipengaruhi oleh kepekatan gliserol dan H_2O_2 .

TABLE OF CONTENTS

SUPERVISOR'S DECLARATION	I
STUDENT'S DECLARATION	II
DEDICATION	III
ACKNOWLEDGEMENTS	IV
ABSTRACT	V
ABSTRAK	VI
TABLE OF CONTENTS	VII
LIST OF TABLES	XI
LIST OF FIGURES	XIV
LIST OF SYMBOLS	XVII
LIST OF ABBREVIATIONS	XIX
CHAPTER 1 INTRODUCTION	1
1.1 Background of The Study	1
1.2 Problem Statement	4
1.3 Research Objective	4
1.4 Research Scopes	5
1.5 Organization of Thesis	6
CHAPTER 2 LITERATURE REVIEW	7
2.1 Introduction	7

2.2	Glycerol	7
2.3	Synthesis of Glycerol	7
	2.3.1 Transesterification Reaction	9
	2.3.2 Saponification	13
	2.3.3 Hydrolysis	13
	2.3.4 Production from Propene	15
	2.3.5 Fermentation from Sugar	15
2.4	Properties of Glycerol	16
2.5	Application of Glycerol	16
	2.5.1 Food Industry	18
	2.5.2 Pharmaceutical and Personal Care Applications	19
	2.5.3 Chemical Intermediate	19
	2.5.4 Gases	19
2.6	Previous Study	19
2.7	Photo-treatment	22
2.8	Mechanism of Photocatalysis	23
2.9	Photocatalyst	25
2.10	Titanium Oxide	26
2.11	Applications of Photocatalyst	28
2.12	Ferrite Based Photocatalyst	30
2.13	Copper Ferrite As Photocatalyst	31
	2.13.1 Previous Study	32
2.14	Advanced Oxidation Process	34
	2.14.1 Fenton Reaction	36
	2.14.2 Photo-Fenton Reaction	37
	2.14.3 Properties of Hydrogen Peroxide	37
	2.14.4 Previous Study	38
CHAPTER 3 METHODOLOGY		40
3.1	Introduction	40
3.2	Materials	40
	3.2.1 Chemicals	40
	3.2.2 Gases	41
3.3	Photocatalyst Preparation	42
3.4	Catalyst Characterization	42

3.4.1	N ₂ Physisorption	42
3.4.2	UV-vis DRS	43
3.4.3	Field Emission Scanning Electron Microscopy (FESEM) - Energy Dispersive X-ray (EDX)	44
3.4.4	X-ray Diffraction (XRD)	45
3.4.5	Particle Size Analyser	46
3.4.6	Summary of the Catalyst Characterization	47
3.5	Photocatalytic Fenton Reaction Studies	48
3.5.1	Photocatalytic Reactor	48
3.5.2	Sample Analysis	49
3.6	Photocatalytic Fenton Reaction	50
3.6.1	Experimental Procedure	50
3.6.2	Photocatalytic Fenton Degradation of Glycerol	50
3.6.3	Adsorption Study	51
3.6.4	Effect of Operating Parameters	51
3.6.4.1	Effect of Photocatalyst	52
3.6.4.2	Effect of Initial Glycerol Concentration	52
3.6.4.3	Effect of Initial H ₂ O ₂ Concentration	52
3.6.5	Factorial Analysis for Degradation of Glycerol	52
3.6.5.1	Validation Experiments	53
3.6.6	Measurement of Photocatalytic Reaction Performance	55
3.7	Samples Detection using HPLC	55
CHAPTER 4 RESULTS AND DISCUSSION		56
4.1	Introduction	56
4.2	Fresh Catalyst Characterization	56
4.2.1	N ₂ -Physisorption	56
4.2.2	FESEM-EDX Analysis	59
4.2.3	XRD Analysis	62
4.2.4	Optical Properties	63
4.2.5	Particle Size Distribution	64
4.3	Photocatalytic Fenton Activity Evaluation	65
4.3.1	Transport Resistance Considerations	65
4.3.1.1	External Mass Transfer	66
4.3.1.2	Pore (Intra-particle) Diffusion Limitation	67
4.3.2	Adsorption Study	68
4.3.3	Effects of Initial Catalyst Loading	71
4.3.4	Effects of Initial Concentration of Glycerol	75
4.3.5	Effects of Initial H ₂ O ₂ Concentration	78
4.3.6	Power Law Modelling	80
4.3.7	Mechanisms of Photocatalytic Fenton Degradation of Glycerol	83
4.4	Experimental design analysis	87

4.4.1	Experimental Design Table	87
4.4.2	Factorial Analysis on Glycerol Degradation	87
4.4.3	Statistical Analysis and Analysis of Variance (ANOVA)	87
4.4.4	Response Surface of Glycerol Degradation	92
4.4.5	Prediction of Best Point	95
CHAPTER 5 CONCLUSIONS AND RECOMMENDATIONS		96
5.1	Conclusions	96
5.2	Recommendations	98
REFERENCES		99
APPENDICES		
A	Catalyst Preparation	107
B	HPLC Calibration	108
C	BET report	111
D	Mastersizer Report	113
E	XRD Report	114
F	Experimental Data	115
G	Calculation for External Mass Transfer	121
H	Calculation for Internal Mass Transfer	123
I	Publications and Conferences	124



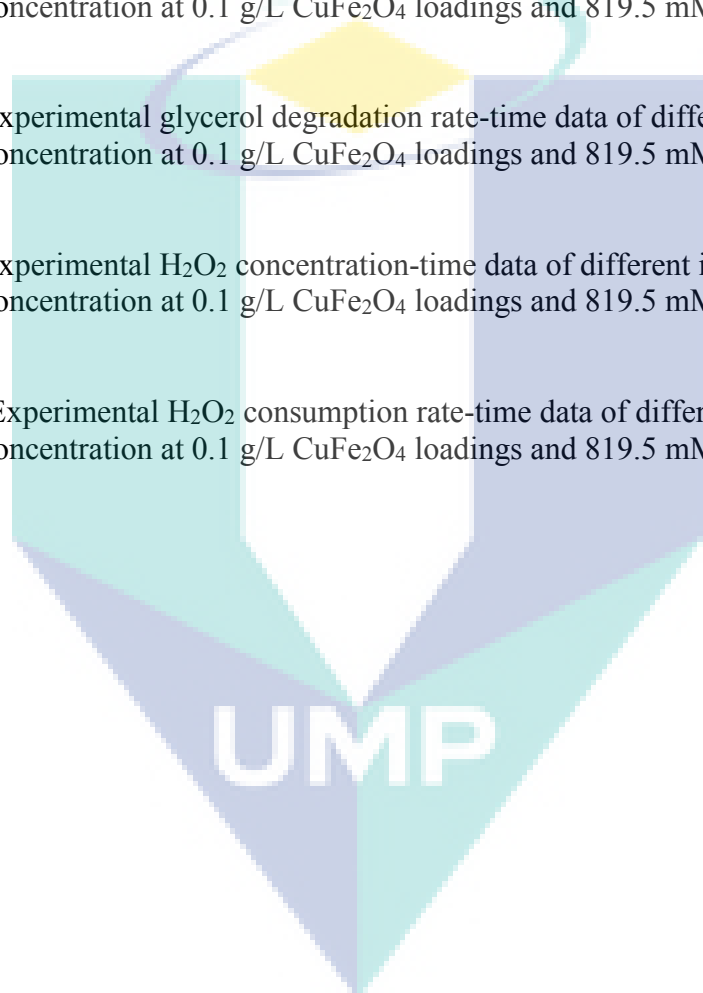
UMP

LIST OF TABLES

Table No.	Title	Page
2.1	Advantages and disadvantages of different type of catalyst used in transesterification process	11
2.2	Properties of glycerol	17
2.3	Previous work done by researchers	20
2.4	Application of TiO ₂ photocatalysis	29
2.5	Band gap energy for different ferrite based photocatalyst	30
2.6	Previous study done by researcher	32
2.7	Types and classification of advanced oxidation processes	35
2.8	Standard reduction potential of oxidants compared with normal hydrogen electrode (NHE, E° = 0 V)	36
2.9	Properties of hydrogen peroxide	38
2.10	Previous work done by researcher	39
3.1	List of chemicals	41
3.2	Lists of gases	41
3.3	Summary of catalyst characterization techniques	48
3.4	Factor and their designated low and high value	53
3.5	Proposed runs by Design Expert	54
4.1	Summary of parameters used in mass and heat transport criteria	68

4.2	Summary of initial rate of glycerol degradation computed from the differentiation of transient concentration profiles of glycerol	81
4.3	Values of kinetic parameters from power law equation	82
4.4	Values of kinetic parameters Eq. (4.10)	85
4.5	Result in Experimental Design	88
4.6	ANOVA analysis of model	90
4.7	Parameter used to test goodness of fit of the model	92
4.8	Suggested best condition of factor in glycerol degradation	95
4.9	Comparison between predicted and experimental value for best condition	95
C.1	Data from BET surface analyser	111
D.1	Data from Mastersizer Analysis Report	113
E.1	XRD Data	114
F.1	Experimental glycerol concentration-time data of different photocatalyst loadings at 68.4 mM glycerol concentration and 819.5 mM H ₂ O ₂ concentration	115
F.2	Experimental glycerol degradation rate-time data of different photocatalyst loadings at 68.4 mM glycerol concentration and 819.5 mM H ₂ O ₂ concentration	115
F.3	Experimental H ₂ O ₂ concentration-time data of different photocatalyst loadings at 68.4 mM glycerol concentration and 819.5 mM H ₂ O ₂ concentration	116
F.4	Experimental H ₂ O ₂ consumption rate-time data of different photocatalyst loadings at 68.4 mM glycerol concentration and 819.5 mM H ₂ O ₂ concentration	116
F.5	Experimental glycerol concentration-time data of different initial H ₂ O ₂ concentration at 68.4 mM glycerol concentration and 0.1 g/L CuFe ₂ O ₄ loadings	117
F.6	Experimental glycerol degradation rate-time data of different initial H ₂ O ₂ concentration at 68.4 mM glycerol concentration and 0.1 g/L CuFe ₂ O ₄ loadings	117

F.7	Experimental H ₂ O ₂ concentration-time data of different initial H ₂ O ₂ concentration at 68.4 mM glycerol concentration and 0.1 g/L CuFe ₂ O ₄ loadings	118
F.8	Experimental H ₂ O ₂ consumption rate-time data of different initial H ₂ O ₂ concentration at 68.4 mM glycerol concentration and 0.1 g/L CuFe ₂ O ₄ loadings	118
F.9	Experimental glycerol concentration-time data of different initial glycerol concentration at 0.1 g/L CuFe ₂ O ₄ loadings and 819.5 mM H ₂ O ₂ concentration	119
F.10	Experimental glycerol degradation rate-time data of different initial glycerol concentration at 0.1 g/L CuFe ₂ O ₄ loadings and 819.5 mM H ₂ O ₂ concentration	119
F.11	Experimental H ₂ O ₂ concentration-time data of different initial glycerol concentration at 0.1 g/L CuFe ₂ O ₄ loadings and 819.5 mM H ₂ O ₂ concentration	120
F.12	Experimental H ₂ O ₂ consumption rate-time data of different initial glycerol concentration at 0.1 g/L CuFe ₂ O ₄ loadings and 819.5 mM H ₂ O ₂ concentration	120



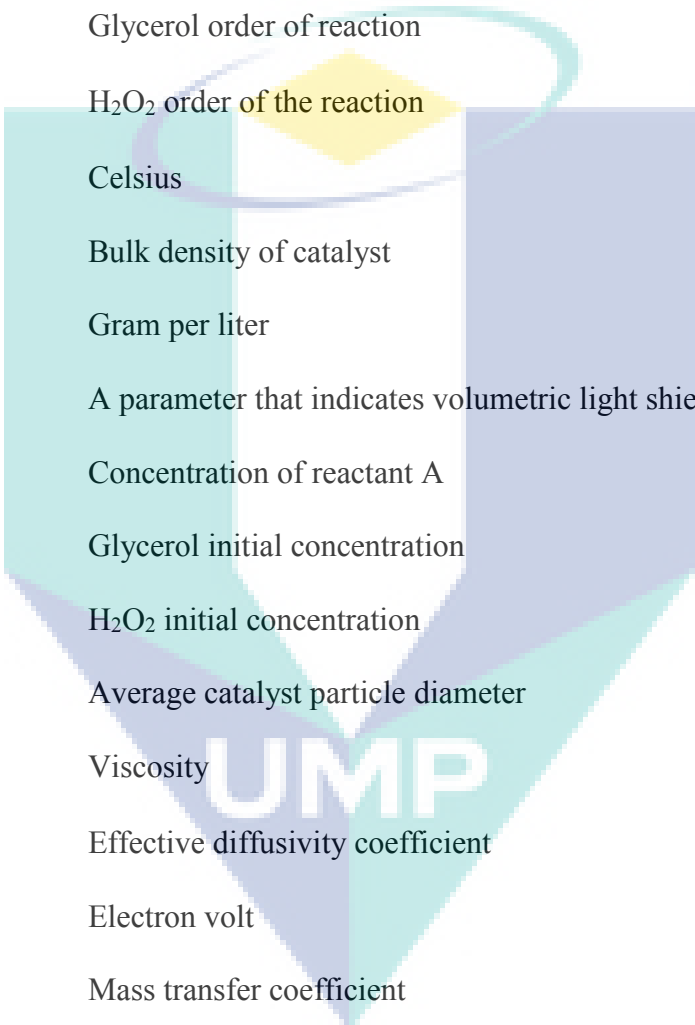
LIST OF FIGURES

Figure No.	Title	Page
2.1	Glycerol production from different process	8
2.2	Glycerol production via transesterification process	9
2.3	Glycerol production and its prices	10
2.4	Saponification process	14
2.5	Hydrolysis process	14
2.6	Glycerol produced from propene	15
2.7	Fermentation of sugar	15
2.8	Application of global glycerol	18
2.9	Glycerol as chemical intermediate	21
2.10	Photosynthesis vs photocatalysis	22
2.11	Mechanism of photocatalysis	23
2.12	Solar energy spectrum	26
2.13	Different ferrite based photocatalyst with different band gap energy	31
3.1	FESEM-EDX system	45
3.2	Sketch of LD instrument part	47
3.3	The experiment setup for photoreaction studies	49

3.4	The setup of photoreaction	51
4.1	Isotherm of CuFe_2O_4 from N_2 Physisorption analysis	58
4.2	Specific surface area determination of CuFe_2O_4 by 2-Parameters Line model	59
4.3	(a) to (c) FESEM image of the fresh CuFe_2O_4 at different magnification levels; (d) EDX image of the fresh CuFe_2O_4 photocatalyst	61
4.4	XRD pattern of CuFe_2O_4 solid sample	62
4.5	Graph of absorbance versus wavelength for as-synthesized CuFe_2O_4	63
4.6	Monodispersity of particle size distribution of the CuFe_2O_4	64
4.7	Transient profiles of (a) $\text{C}_3\text{H}_8\text{O}_3$ concentration, (b) $\text{C}_3\text{H}_8\text{O}_3$ adsorption (%), (c) H_2O_2 concentration and (d) H_2O_2 adsorption (%) at 0.1 g/L CuFe_2O_4 photocatalyst, 68.41 mM glycerol and 819.5 mM H_2O_2 under dark environment	70
4.8	Transient profiles of (a) glycerol concentration and (b) glycerol degradation (%) at different photocatalyst loadings	72
4.9	(a) H_2O_2 concentration (b) H_2O_2 utilization versus time at different photocatalyst loadings	73
4.10	Glycerol photocatalytic Fenton degradation rate at different photocatalyst	75
4.11	Transient profiles of (a) glycerol concentration and (b) glycerol degradation (%) at different initial glycerol concentrations	76
4.12	Transient profiles of (a) H_2O_2 concentration and (b) H_2O_2 utilization at different initial glycerol concentration	77
4.13	(a) Glycerol concentration (b) glycerol degradation versus time at different initial H_2O_2 concentration	79

4.14	(a) H ₂ O ₂ concentration (b) H ₂ O ₂ utilization versus time at different initial H ₂ O ₂ concentration	80
4.15	Parity plot showing the adequacy of power law modelling	82
4.16	Residual plot showing random distribution of error	83
4.17	Parity plot showing the adequacy of Langmuir-Hinshelwood modelling	86
4.18	Residual plot showing random distribution of error	86
4.19	Pareto chart for t-value of effects	89
4.20	Comparison between predicted result and experimental result of factorial design	93
4.21	Response surface plot of glycerol degradation as a function of: (a) different H ₂ O ₂ concentration and time at fixed initial glycerol concentration and photocatalyst loading; (b) different initial glycerol concentration and H ₂ O ₂ concentration at fixed time and photocatalyst loading	94
B.1	PLC chromatogram obtained from the HPLC instrument	108
B.2	Standard calibration curves for (a) C ₃ H ₈ O ₃ solution and (b) H ₂ O ₂ solution	109
C.1	Surface Area (B.E.T.) 2 Parameter Line	112

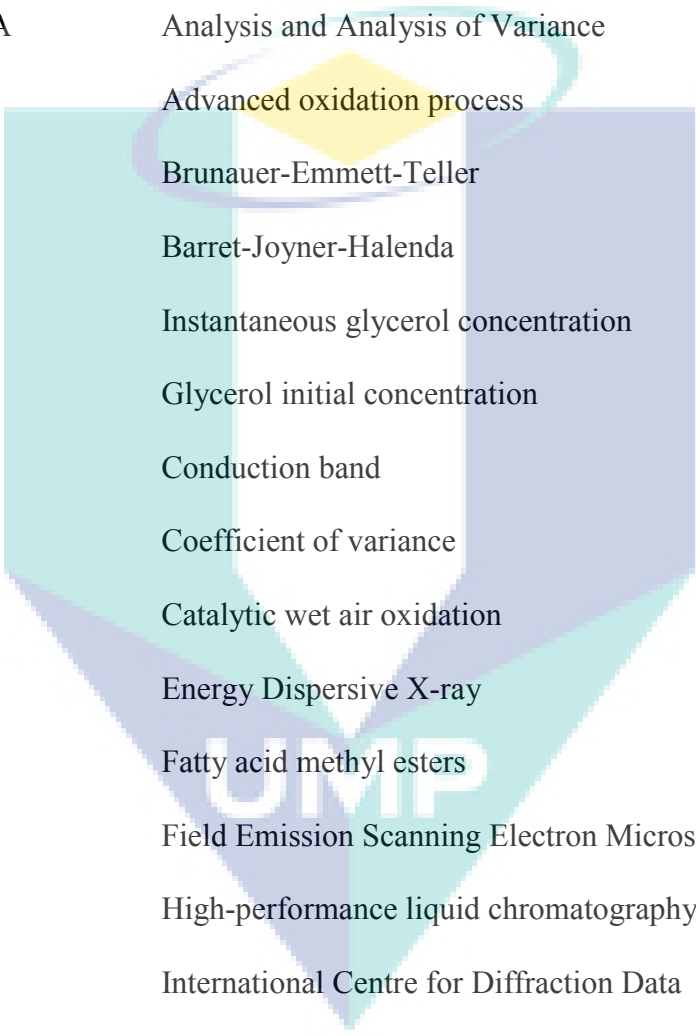
LIST OF SYMBOLS



α	Glycerol order of reaction
β	H ₂ O ₂ order of the reaction
°C	Celsius
ρ_b	Bulk density of catalyst
g/L	Gram per liter
A	A parameter that indicates volumetric light shielding effect
C_A	Concentration of reactant A
$C_{glycerol}$	Glycerol initial concentration
$C_{H_2O_2}$	H ₂ O ₂ initial concentration
d_p	Average catalyst particle diameter
μ	Viscosity
D_{eff}	Effective diffusivity coefficient
eV	Electron volt
k_c	Mass transfer coefficient
k_{app}	Apparent specific reaction rate
k_{rxn}	Reaction rate constant
K	Pseudo-rate constant
$K_{glycerol}$	Adsorption constant for glycerol
$K_{H_2O_2}$	Adsorption constant for H ₂ O ₂

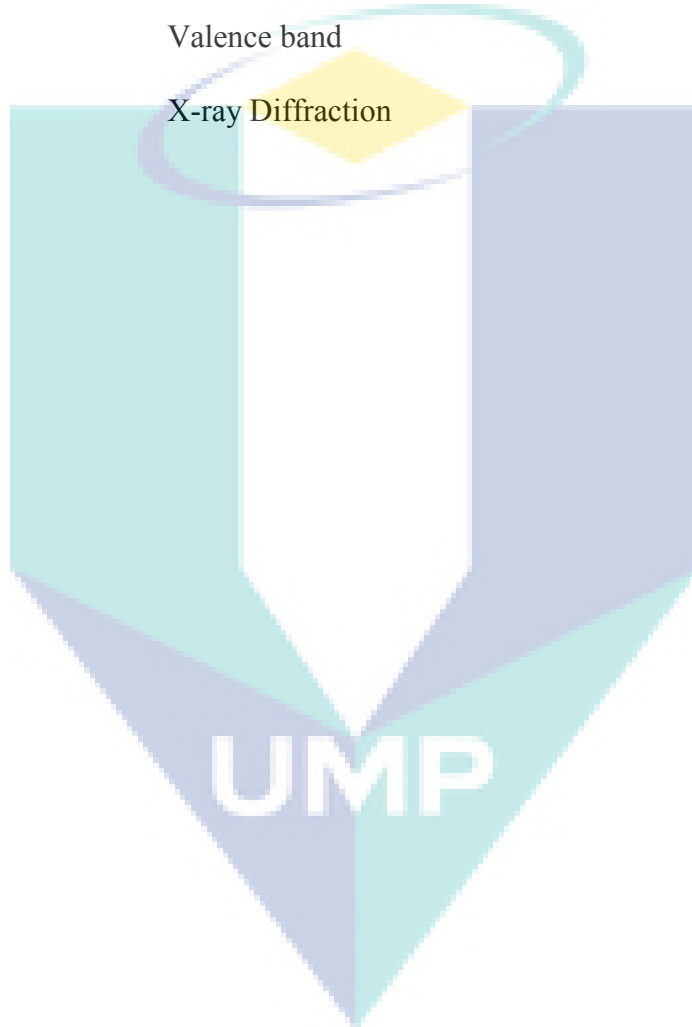
mg	Milligram
mM	Millimolar
n	Reaction rate order
$-r_{glycerol}^o$	Initial rate of glycerol photocatalytic Fenton degradation
ρ_c	Density of the solid catalyst particle
ρ_b	bulk density of catalyst
ρ_w	Density of water
d_p	average catalyst particle diameter
T	Temperature
D_{AB}	Diffusion coefficient
D_{eff}	effective diffusivity coefficient
k_c	mass transfer coefficient
U	velocity
C_A	concentration of reactant A
ε	Constant

LIST OF ABBREVIATIONS



ANOVA	Analysis and Analysis of Variance
AOP	Advanced oxidation process
BET	Brunauer-Emmett-Teller
BJH	Barret-Joyner-Halenda
Ca	Instantaneous glycerol concentration
Ca ₀	Glycerol initial concentration
CB	Conduction band
CV	Coefficient of variance
CWAO	Catalytic wet air oxidation
EDX	Energy Dispersive X-ray
FAME	Fatty acid methyl esters
FESEM	Field Emission Scanning Electron Microscopy
HPLC	High-performance liquid chromatography
ICDD	International Centre for Diffraction Data
LC	Liquid chromatography
LD	Laser diffraction
LH	Langmuir-Hinshelwood
LHS	Left-hand side
NHE	Normal hydrogen electrode

PRESS	Prediction residual error sum of squares
RI	Refractive index
UMP	Universiti Malaysia Pahang
UV	Ultraviolet
VB	Valence band
XRD	X-ray Diffraction



CHAPTER 1

INTRODUCTION

1.1 BACKGROUND OF THE STUDY

Today, most of the energy demand is derived primarily from fossil-based resources. In the United States alone, the largest energy consumer in the world, fossil fuel utilization about 67% in 2014. In contrast, renewable energy only corresponds to a meagre 7% (U.S. Energy Information Administration, 2015). Inevitably, with increasing global energy consumption due to the rising population growth (1% per annum), eventually fossil-based resources will become scarce and renewable options are necessary to complement the energy supply. Moreover, large scale use of fossil fuels has led to global warming. To reverse this trend, environment regulations have become more stringent and the search for renewable energy intensified. In this respect, the use of renewable biofuels presents itself as one of the most promising solutions as it can decrease the production of greenhouse gases.

Various biofuels have been proposed as alternative fuels, hydrogen, methanol, ethanol and biodiesel. In particular, biodiesel shows tremendous potential as a liquid transportation fuel due to its renewability, environmental-friendliness attributed to the low carbon dioxide (CO₂) emission, easy storage and economic viability in the event of fossil fuel shortage. In the United States, a 500-fold surge in biodiesel manufacture is registered. However, during the transesterification, glycerol is produced in the amount of one mole of glycerol for every three moles of fatty acid methyl esters (FAME). Moreover, glycerol is also produced via saponification or hydrolysis process. Traditionally, glycerol is used in

food industry, pharmaceutical and personal care, paints, paper, textile, etc. In addition, it is also used as a chemical intermediate to produce downstream chemicals such as acrolein, acetaldehyde, propionaldehyde, allyl alcohol, methanol, ethanol, formaldehyde (Bühler et al., 2002), lactic acid, 1,2-propanediol (Yuan et al., 2010), glycolipids (Liu et al., 2011) and other chemicals. Nonetheless, the quantity involved is limited.

Due to this scenario, the world demand on glycerol is expected to remain bearish (Quispe et al., 2013; Yang et al., 2012). Consequently, glycerol which is co-produced at 10 wt.% during biodiesel synthesis, most likely will end up as waste (Daskalaki and Kondarides, 2009). Although it has been claimed that glycerol poses no hazard as waste water because it is completely biodegradable in sewage treatment plants and is not even regarded as a danger to water (H₂O) supply in some countries, its presence in wastewater is liable to payment of duty because of its high oxygen demand: COD=127 mg of oxygen (O₂) per gram: BOD = 780 mg of O₂ per gram (Sevas Educational Society, 2003). Crude glycerol content ranged between 38% and 96% (Yang et al., 2012). Furthermore, the purification of glycerol to achieve USP glycerine grade is economically expensive as it requires vacuum distillation application. Therefore, a green method to treat glycerol waste is clearly desirable. Significantly, the use of light source as the driving force behind the glycerol decomposition is a sufficiently green technique.

In recent years, advanced oxidation process (AOP) has been described as a promising option to remove organic pollutants from the contaminated H₂O compared to the conventional method (Chacó et al., 2006). AOP is a physicochemical process to degrade pollutants in wastewater by oxidation with O₂ or the use of high energy oxidants that are able to generate •OH radicals. The •OH radicals will subsequently attack organic pollutant in wastewater to mineralize it into simple products such as CO₂, and H₂O. Common AOPs are comprised of photocatalytic technique, Fenton reaction, photo-Fenton, ozonation, photochemical and electrochemical oxidation methods (Ameta et al., 2012).

Fenton technology, one of the AOPs, is a well-known method for the treatment of industrial wastewater. Fenton's reagent is a mixture of hydrogen peroxide (H₂O₂) and

ferrous ion (Fe^{2+}) that generates hydroxyl radicals ($\bullet\text{OH}$) under normal ambient condition. The use of ferrous ion which is non-toxic, and H_2O_2 which is an environmental-friendly agent, offers main advantage feature of the process. However, Fenton process has two disadvantages which are limited by low pH range (pH of 2 to 3), and producing a large iron sludge at the end of the process (Wang et al., 2014). When Fenton reacts with ultraviolet (UV) radiation, visible light or a combination of both, the process is known as a photo-Fenton process. When photocatalyst is used in photo-Fenton process, the overall process is termed as a photocatalytic Fenton process. Hence, heterogeneous Fenton-like photocatalysis is foreseen being able to overcome the two disadvantages of the typical Fenton technology.

Various kinds of heterogeneous catalysts such as nanoparticle zerovalent iron, iron oxides and iron-immobilized clays have been investigated for degrading organic pollutants (Xu and Wang, 2012). However, these heterogeneous catalysts showed weak catalytic activity. Besides that, leaching of Fe contents from the bulk catalysts to the solution and the difficulty to separate them from the treated H_2O leads to depletion of their catalytic activity in the long term (Wang et al., 2014). Consequently, the development of a new breed of catalyst that can enhance the activity of heterogeneous catalyst, for example copper ferrite photocatalyst is attractive.

Copper ferrite (CuFe_2O_4) is a photocatalyst that possesses significant activity under the visible light. As comparing to well-known photocatalyst such as titanium oxide (TiO_2), copper ferrite can absorb visible light which represent 46% of solar energy spectrum while TiO_2 only can absorb UV light which is 5%. CuFe_2O_4 possess narrow energy band gaps (1.32 eV), hence able to absorb a large portion of light spectrum. Therefore, it is more feasible to use the visible light in photocatalytic Fenton reaction due to aforementioned reason. Due to its chemical stability, CuFe_2O_4 has been employed in many prior works particularly in the areas of dye decolouration and organic decomposition, i.e. Mahmoodi (2011) studied the dyes decolouration using copper ferrite, Shen et al. (2013) evaluated the photocatalytic conversion of benzene, Guan et al. (2013) have investigated the degradation

of atrazine by copper ferrite, whilst Wang et al. (2014) have studied the degradation of imidacloprid, just to name a few.

Due to the absence of previous works pertaining to the use of photocatalytic Fenton technique for degrading the glycerol, in this research, CuFe_2O_4 was prepared via sol-gel method and was subsequently employed as a photocatalyst in heterogeneous Fenton-like reaction for decomposing lab-prepared glycerol solution (as a model compound) for reaction investigation in order to serve as a baseline study.

1.2 PROBLEM STATEMENT

1. A large scale production of biodiesel will generate excess glycerol. Glycerol purification is a cost-prohibitive process. Furthermore, mass production of glycerol by-product will pile severe downward pressure on glycerol price, consequently glycerol will become a waste problem to the biodiesel industry.
2. Most of the earlier works on advanced oxidation process or also known as AOP utilizes UV-responsive TiO_2 material. However, this is impractical as natural solar spectrum is comprised of meagre 5% UV light, whilst the proportion of visible light on the other hand, is 46%; hence represents a more feasible source of energy.
3. The application of copper ferrite in photocatalytic Fenton degradation of glycerol represents a new, unexplored knowledge frontier; hence warrants a scientific investigation. In the lab, this objective can be achieved via investigation into lab-prepared glycerol solution as a model compound.

1.3 RESEARCH OBJECTIVE

The overall thrust of this thesis are:

1. To prepare and characterize copper ferrite photocatalyst.

2. To study the reaction of copper ferrite photocatalyst in photocatalytic Fenton degradation of glycerol.
3. To study the kinetic model of glycerol degradation by Power Law model and Langmuir-Hinshelwood model.
4. To perform the statistical analysis using factorial analysis.

1.4 RESEARCH SCOPE

In order to achieve the outlined objectives, the specific scopes of this project are:

1. To synthesize and to undertake detailed characterization of the CuFe_2O_4 photocatalyst (N_2 physisorption, UV-vis DRS, FESEM-EDX, XRD and particle size analyser) with a view to relate its physicochemical attributes to the kinetic and reaction mechanism of photocatalytic Fenton degradation of glycerol.
2. To study the (i) effect of glycerol concentration ranging from 27.36 mM to 68.41 mM, (ii) effect of photocatalyst loadings in between 0.1 to 5.0 g/L, and (iii) effect of hydrogen peroxide concentration from 163.9 to 819.5 mM, towards photocatalytic Fenton treatment of glycerol.
3. To study the factors (experiment time, glycerol concentration, hydrogen peroxide concentration and copper ferrite loadings) in degradation of glycerol by using Design Expert version 7.0.0.

1.5 ORGANIZATION OF THESIS

The flow of the chapters is presented as follow:

Chapter 2 offers an overall literature review of the topic. Chapter 2 provides a review on the literature on the topic of glycerol, synthesis of glycerol, properties of glycerol, application of glycerol, definition of photo-treatment, mechanism of photocatalysis, photocatalyst definition, titania as a photocatalyst, application of photocatalyst, study on ferrite based photocatalyst, copper ferrite as photocatalyst and lastly, Fenton reaction.

Chapter 3 explains the experimental details. This encompasses catalyst preparation, catalyst characterization techniques and glycerol photocatalysis experimental set up and procedures. Besides, HPLC analysis for determining glycerol concentration as well as, two level full factorial design, are also explained in this chapter.

Chapter 4 is dedicated to the physicochemical property determination of CuFe_2O_4 photocatalyst and investigation of the kinetics of the photocatalytic Fenton degradation of glycerol. Result on analysis of full factorial design is also further discussed at the end of this chapter.

Finally, chapter 5 concludes the findings of current study followed by some recommendations for future studies.

CHAPTER 2

LITERATURE REVIEW

2.1 INTRODUCTION

This chapter consists of 13 sections with the following headings; glycerol definition, synthesis of glycerol, properties of glycerol, application of glycerol, definition of photo-treatment, mechanism of photocatalysis, photocatalyst definition, titania as a photocatalyst, application of photocatalyst, study on ferrite based photocatalyst, copper ferrite as photocatalyst and advanced oxidation process.

2.2 GLYCEROL

Glycerol also known as glycerine is a colourless, odourless and highly viscous liquid, which is relatively soluble in water due to the three hydroxyl group in the molecular structure. It is usually obtained as a by-product in the production of biodiesel via transesterification reaction and in oleochemical plants via saponification and hydrolysis reaction. The glycerol produced through these processes often contains impurities such as oil, soap, alkaline, salt or iodols.

2.3 SYNTHESIS OF GLYCEROL

Glycerol is produced in two ways, which are natural glycerin (as a by-product) and synthetic glycerol (Quispe et al., 2013). Natural glycerin is obtained from

transesterification, saponification and hydrolysis. Natural glycerin is generally produced by reacting fats and oils to obtain soaps. Figure 2.1 shows the production of glycerol from 1999 to 2009 through different method. Nowadays, transesterification is the most common method to generate glycerol. These three processes are explained in detail in sections 2.3.1-2.3.3. Synthetic glycerol is obtained from propylene and fermentation from sugar.

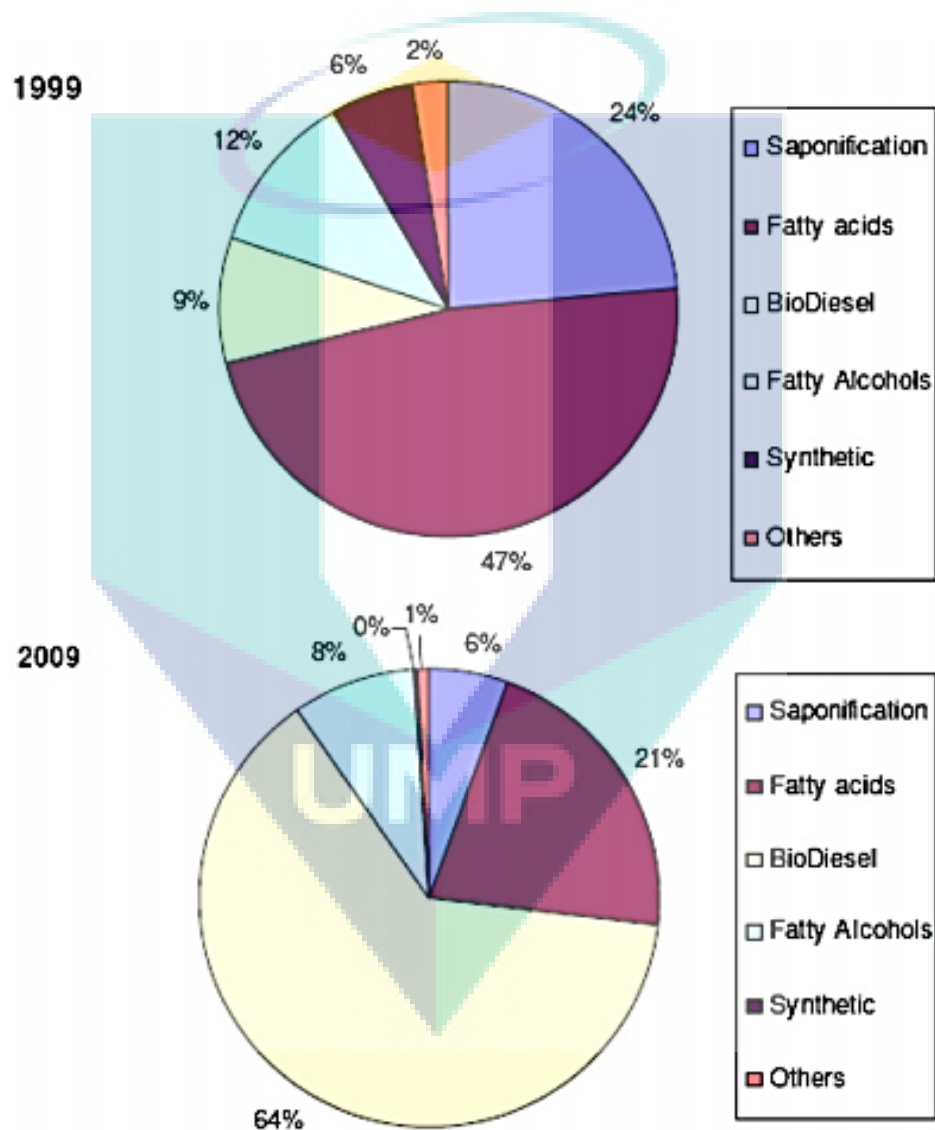


Figure 2.1: Glycerol production from different process

Source: Ciriminna et al. (2014)

2.3.1 Transesterification Reaction

Glycerol is the main by-product generated during transesterification process in biodiesel production. Transesterification reaction is a reaction between vegetable oils or animals fats with alcohol such as methanol and ethanol in the presence of catalyst as presented in Figure 2.2 (Li et al., 2006). The reaction is carried out in either a batch or continuous reactor. The product of this reaction will be separated into two phases as a result of different density. The first phase at the top layer is biodiesel-rich phase whereas the second phase is the glycerol-rich phase (Tan et al., 2013). Approximately 10% glycerol is produced from production of biodiesel. Nowadays, most of the glycerol is purified and recovered from biodiesel production. Moreover, increasing biodiesel production will also increase glycerol production. In 2016, it is estimated 4 billion gallons of crude glycerol will be produced and this will pull-down the market price of glycerol (López et al., 2009). Figure 2.3 shows the world glycerol production and its price from 2001-2011. As shown from the graph, production of glycerol increases yearly and this resulted to decrease its market prices comparing between year 2001 and 2011.

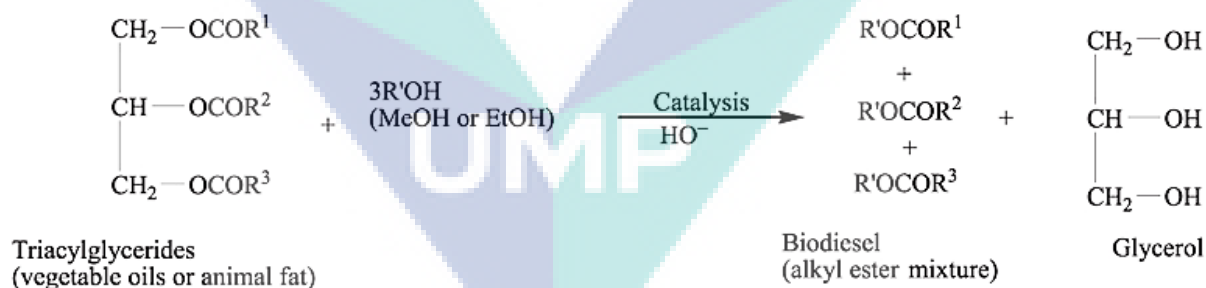


Figure 2.2: Glycerol production via transesterification process

Source: Meireles & Pereira (2013)

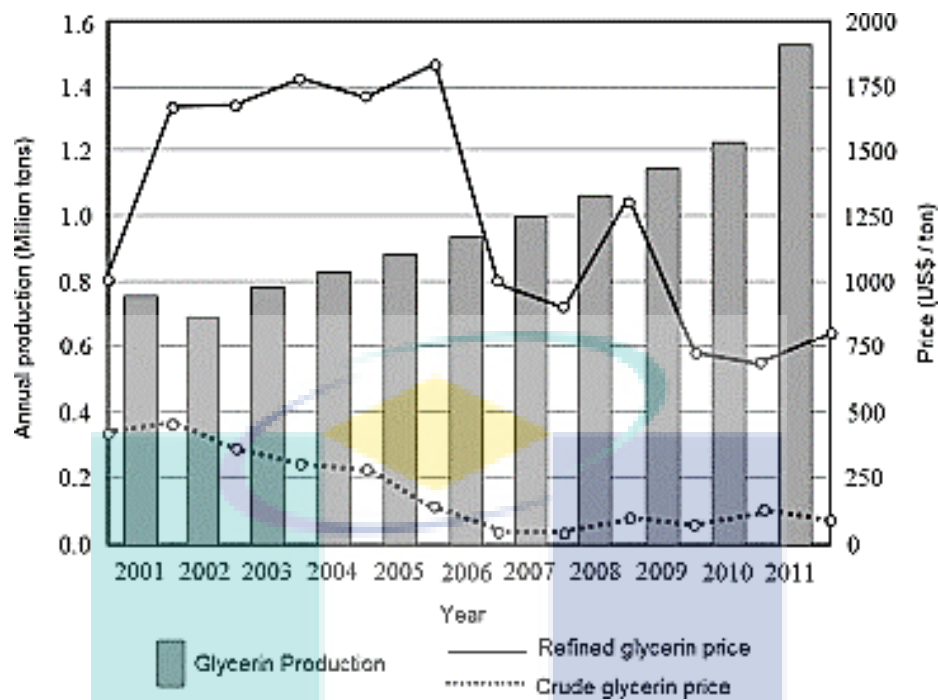


Figure 2.3: Glycerol production and its prices

Source: Quispe et al. (2013)

There are three type transesterification namely acid catalyzed, base catalyzed and enzymatic catalyzed. Table 2.1 shows the advantages and disadvantages of different types of catalyst used in transesterification process.

Table 2.1: Advantages and disadvantages of different type of catalyst used in transesterification process

Types of Catalyst	Examples	Advantages	Disadvantages
Homogeneous base catalyst	<ul style="list-style-type: none"> • NaOH • KOH 	<ul style="list-style-type: none"> • Reaction rate is fast • The reaction can occur at mild reaction condition and less energy intensive • Achieve high conversion • Catalyst are commercial 	<ul style="list-style-type: none"> • Sensitive to FFA content in the oil • If the FFA content in the oil is more than 2 wt.%, soap will formed • Too much soap formation will decrease the biodiesel yield
Heterogeneous base catalyst	<ul style="list-style-type: none"> • CaO • MgO 	<ul style="list-style-type: none"> • Reaction rate is faster than acid catalyzed transesterification • The reaction can occur at mild reaction condition and less energy intensive • The catalyst is easy separate from product • The catalyst can be reuse and regenerate 	<ul style="list-style-type: none"> • Poisoning the catalyst when exposed to ambient air • Sensitive to FFA content in the oil • If the FFA content in the oil is more than 2 wt.%, soap will formed • Too much soap formation will decrease the biodiesel yield • Leaching of catalyst active sites

Table 2.1: Advantages and disadvantages of different type of catalyst used in transesterification process (continued)

Types of Catalyst	Examples	Advantages	Disadvantages
Homogeneous acid catalyst	<ul style="list-style-type: none"> • H_2SO_4 • HCl 	<ul style="list-style-type: none"> • Insensitive to FFA and water content in the oil • Preferred if using low grade oil • Esterification and transesterification occur at the same time • Reaction can occur at mild reaction condition and less energy intensive 	<ul style="list-style-type: none"> • Reaction rate is slow • Corrosive catalyst such as H_2SO_4 used can lead to corrosion on reactor and pipelines • Separation of catalyst from product is problematic
Heterogeneous acid catalyst	<ul style="list-style-type: none"> • ZrO_2 • TiO_2 • SnO_2 • Zeolite 	<ul style="list-style-type: none"> • Insensitive to FFA and water content in the oil • Preferred if using low grade oil • Esterification and transesterification occur at the same time • Catalyst is easily separate from product • Catalyst can be reuse and regenerate 	<ul style="list-style-type: none"> • Complicated catalyst synthesis procedures lead to higher cost • Require high reaction temperature, high alcohol to oil molar ratio • Long reaction time • Energy intensive • Leaching of catalyst active sites

Table 2.1: Advantages and disadvantages of different type of catalyst used in transesterification process (continued)

Types of Catalyst	Examples	Advantages	Disadvantages
Enzyme	<ul style="list-style-type: none"> • Mucor miehei • C. antarctica • Bacillus subtilis 	<ul style="list-style-type: none"> • Insensitive to FFA and water content in the oil • Preferred if using low grade oil • Transesterification can be carried out at low reaction temperature • Only simple purification step is required 	<ul style="list-style-type: none"> • Reaction rate is slow • High cost • Sensitive to alcohol

Source: Lam et al. (2010) and Tan et al. (2013)

2.3.2 Saponification

Saponification is a process that produces soap from fats. Saponification is the reaction of fats and oils (triglycerides) using alkali catalyst such as NaOH to produce salts of fatty acid (soap) and glycerol as presented in Figure 2.4 (Tamalampudi et al., 2008)

2.3.3 Hydrolysis

Hydrolysis is the separation of chemical bonds by adding water. Hydrolysis often involves the reaction of fat/oils (triglyceride) with water to obtain glycerol and fatty acids. This reaction is a reversible reaction whereby a molecule of steam breaks a fatty acid off

the glycerine backbone of a triglyceride, resulting in a free fatty acid and glycerol (Gregg and Goodwin, 2008). Figure 2.5 shows the hydrolysis process in producing glycerol.

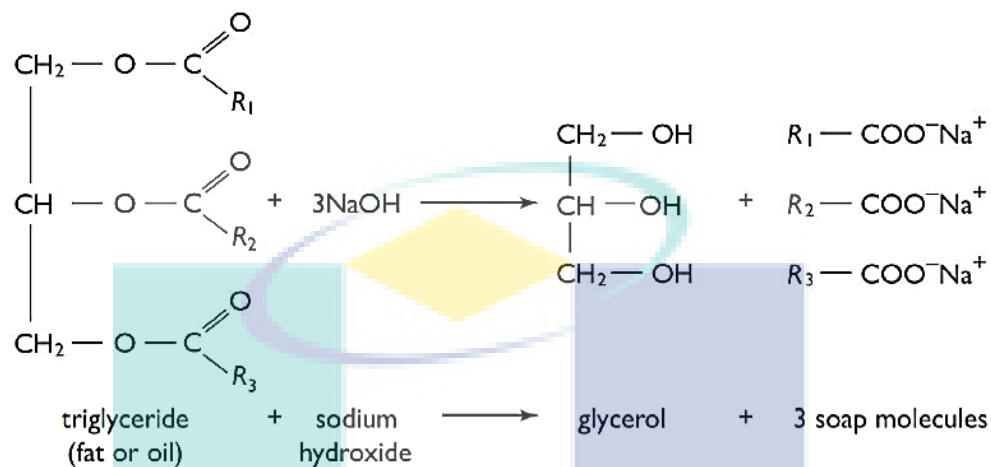


Figure 2.4: Saponification process

Source: "Saponification" (2015)

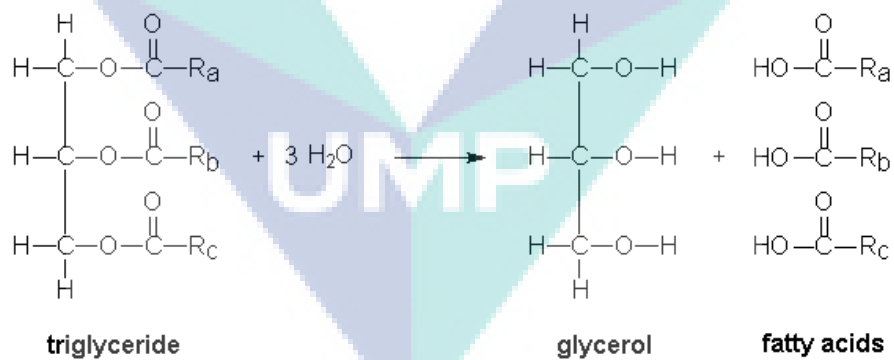


Figure 2.5: Hydrolysis process

Source: Russell (2012)

2.3.4 Production from Propene

Glycerol produced from propene will undergo a few intermediates stages. Propene is firstly chlorination to allyl chloride and then isomerized to allyl alcohol. After that, epoxidation occurs with peracetic acid and lastly hydrolyzed to glycerol. Glycerol produced from propene is shown in Figure 2.6.

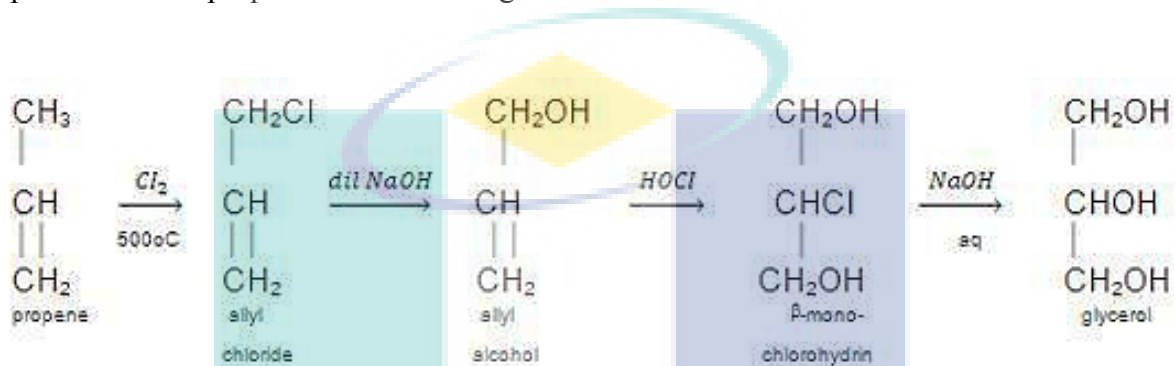


Figure 2.6: Glycerol produced from propene

Source: askIITians (2015)

2.3.5 Fermentation from Sugar

Fermentation of sugar gives 3% of glycerol. The yield will increase to 25% if the fermentation process adding yeast for example sodium sulphite (Na_2SO_3). Figure 2.7 shows the fermentation of sugar producing glycerol.



Figure 2.7: Fermentation of sugar

2.4 PROPERTIES OF GLYCEROL

Glycerol with a formula $C_3H_8O_3$, is completely soluble in water and alcohol. It is slightly soluble in ether, ethyl acetate, and dioxane and insoluble in hydrocarbons (Pagliaro et al., 2008). It is also a low toxicity alcohol (Tan et al., 2013). Since glycerol has three hydroxyl groups, glycerol undergoes all the usual reactions of alcohols. The two terminal primary hydroxyl groups are more reactive than the internal secondary hydroxyl group. In addition, glycerol is non-toxic. Table 2.2 shows the physical properties of glycerol.

2.5 APPLICATION OF GLYCEROL

Glycerol is the main by-product from biodiesel production. Biodiesel production has been projected to increase in the future and hence glycerol as the by-product will also increase. Since glycerol production is increasing on an annual basis, past researches have been explored new markets or new applications of glycerol into value-added products such as food industry, pharmaceutical and personal care applications, tobacco, paints, papers, textiles, leather and others (Wang et al., 2001; Yang et al., 2012). As compare to others petro-chemically produced hydrocarbons, glycerol is a highly functionalized molecule and thus a number of chemicals can be produced from glycerol (Tan et al., 2013). Figure 2.8 shows the application of global glycerol for the year 2009 and 2015.

Table 2.2: Properties of glycerol

Physical Properties	
Odor	odorless
Appearance	colourless liquid
Molecular weight	92.09 g/mol
Density (20°C)	1.26 g/cm ³
Viscosity	1499 c.p. at 20°C (100% glycerol)
Melting point	18.17°C
Boiling point (760 mm Hg)	290°C
Vapor pressure	0.0025 mm Hg at 50°C, 0.195 mm Hg at 100°C 4.3 mm Hg at 150°C, 46 mm Hg at 200°C
Refractive index	1.474
Surface tension	63.4 dyne/cm at 20°C (100% glycerol)
Compressibility (28.5°C)	2.1×10 MPa
Specific heat	0.5779 cal/gm at 26°C (99.94% glycerol)
Heat of vaporization	21060 cal/mol at 55°C, 18170 cal/mol at 195°C
Heat of formation	159.6 kcal/gm mol
Heat of combustion	1662 kJ/mol
Heat of fusion	18.3 kJ/mol
Thermal conductivity	0.29 W/°K
Flash point	177°C
Fire point	204°C

Source: Gregory (1991), Organization for Economic Cooperation and and Development (2002), and The Soap and Detergent Association (1990)

2.5.1 Food Industry

In food industry, glycerol serves as humectant, solvent, sweetener, and preservative (The Soap and Detergent Association, 1990). Glycerol is used as a humectant for baking which helps to keep the freshness of the bakery products. It can also be added to soft drinks and desserts as a solvent for flavors and food colorings. Glycerol acts as a sweetener in either foods or drinks due to its sweetness. Its sweetness is around 60% of that of normal white sugar (sucrose). Besides that, preservative function of glycerol can be employed in the candies and icing making to prevent crystallization (Gregory, 1991). Glycerol is labeled as E number E422 when it is added to foods. According to Yang et al. (2012) glycerol is used as dry pet foods either in non-ruminant diets or ruminant diets. It provides energy by converting glucose.

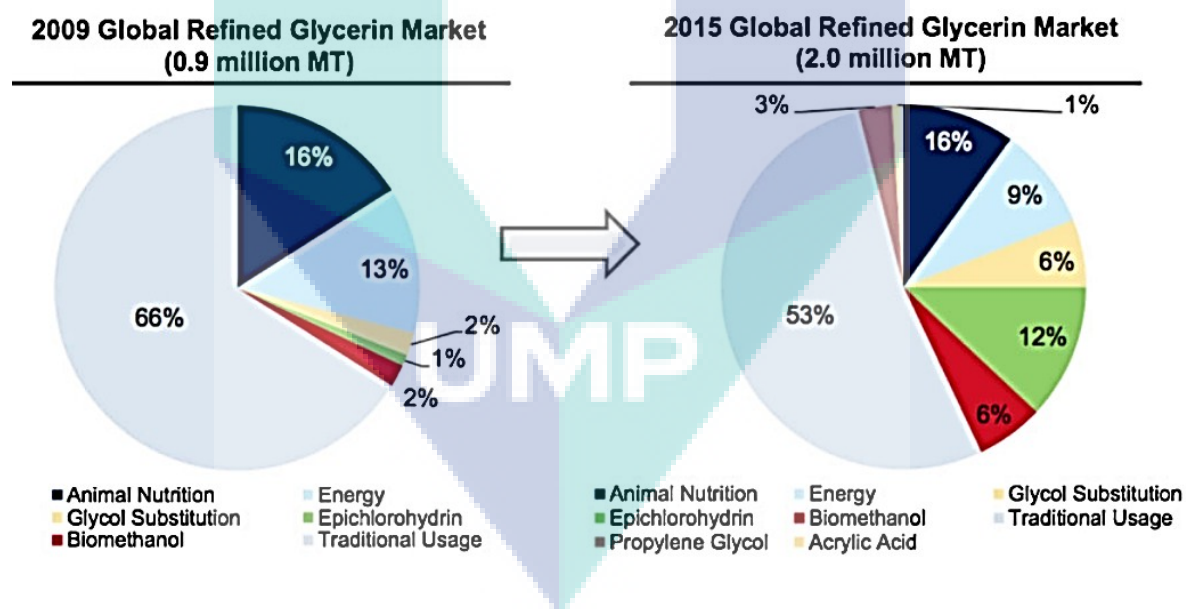


Figure 2.8: Application of global glycerol

Source: Ciriminna et al. (2014)

2.5.2 Pharmaceutical and Personal Care Applications

Besides application in food industry, glycerol is also widely use in pharmaceutical and personal care application. In pharmaceutical, glycerol is used as drugs ingredients. The capsule of the medicine is plasticized with glycerin. Due to its non-toxic, non-irritating and odorless properties, glycerol is widely use in cosmetics and other toiletry application. In personal pare application, glycerin is a main ingredient in toothpaste. Others personal care for example skin creams, deodorants, lotions are the function of glycerol (Ciriminna et al., 2014; Pagliaro et al., 2008; Quispe et al., 2013; Tan et al., 2013).

2.5.3 Chemical Intermediate

Glycerol can be used as chemical intermediate for production of several value-added chemical through different types of chemical reactions. For the example, 1,3-propanediol can be produced by fermentation, dehydroxylation and hydrogenolysis of glycerol (Tan et al., 2013). Besides that, glycerol can be converted to acrolein, ethanol, epichlorohydrin and others. Figure 2.9 shows conversion of glycerol to value-added chemicals.

2.5.4 Gases

Glycerol can be converted into gases such as hydrogen, carbon dioxide, carbon monoxide, methane via steam reforming, dry reforming, and partial oxidation process. These processes require high temperature around 700 °C to be operated.

2.6 PREVIOUS STUDY

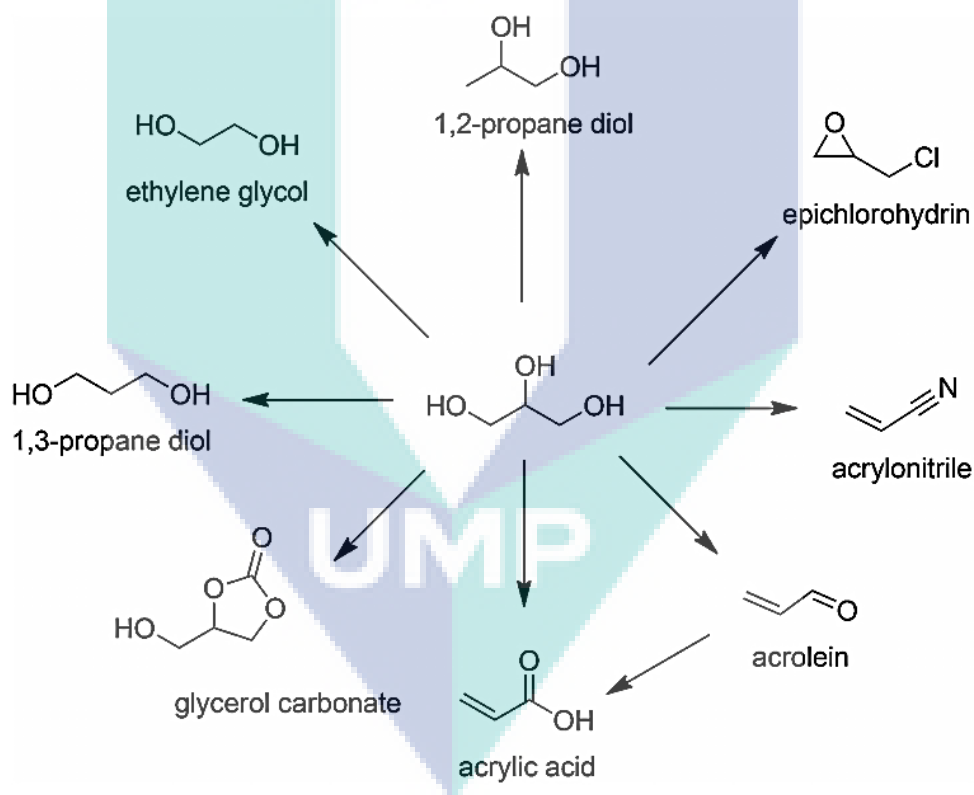
In the past few years, researchers have done some research on degradation of glycerol using different types of photocatalyst, with details listed in the Table 2.3.

Table 2.3: Previous work done by researchers

Title	Authors	Parameter	Conclusion
Cobalt doped TiO ₂ : A stable and efficient photocatalyst for continuous hydrogen production from glycerol: Water mixtures under solar light irradiation	Sadanandam et al., 2013	<ul style="list-style-type: none"> • Cobalt (0.2, 0.5, 1, 2, 3 and 5 wt%) was doped on TiO₂ • Under solar and UV light irradiation • 5% (v/v) glycerol: water mixtures 	Optimal hydrogen production activity is obtained for 1 wt% cobalt doped TiO ₂ under solar light irradiation. When these catalysts are studied under UV irradiation, a 3e4 fold increase in activity is observed.
Partial photocatalytic oxidation of glycerol in TiO ₂ water suspensions	Augugliaro et al., 2010	<ul style="list-style-type: none"> • TiO₂ • Hg lamp and Philips fluorescent lamps • glycerol in the concentration range of 10–180 mM 	TiO ₂ commercial samples showed the best performances both for reaction rates and products selectivity.
Glycerol as a probe molecule to uncover oxidation mechanism in photocatalysis	Minero et al., 2012	<ul style="list-style-type: none"> • TiO₂ • Philips TL K 05 fluorescent lamp • glycerol 	Different TiO ₂ specimens have different selectivity toward glycerol transformation.
Sonochemical synthesis of Cd _{1-x} Zn _x S solid solutions for application in photocatalytic reforming of glycerol to produce hydrogen	Lopes et al., 2015	<ul style="list-style-type: none"> • Pure CdS and ZnS and Cd(1-x)Zn(x)S • HgXe arc lamp • 50% v/v glycerol 	The maximum hydrogen evolution rate achieved was 239 mmol/gh, when the solid solution Cd(0.6)Zn(0.4)S.

Table 2.3: Previous work done by researcher (continued)

Title	Authors	Parameter	Conclusion
Route of glycerol conversion and product generation via TiO ₂ -induced photocatalytic oxidation in the presence of H ₂ O ₂	Jedsukontorn et al., 2015	<ul style="list-style-type: none"> • 1–3 g/L TiO₂ • 0.3–1.5 M H₂O₂ concentration • UV light • 0.3 M glycerol 	The presence of H ₂ O ₂ in the photocatalytic process can enhance conversion of glycerol and product generation via radical-mediated oxidation.

**Figure 2.9:** Glycerol as chemical intermediate

Source: Sheldon (2014)

2.7 PHOTO-TREATMENT

Photo-treatment defined as a treatment which requires light in the reaction. Photocatalysis is one of the photo-treatment in the presence of photocatalyst. This technology has generated an interest in environmental issues nowadays. Photocatalysis defined as the acceleration of photoreaction in the presence of a catalyst. The difference between photocatalysis and photosynthesis is that chlorophyll turns water and carbon dioxide to oxygen and glucose in the presence of sunlight while photocatalysis creates strong oxidation agent to breakdown organic matter into carbon dioxide and water in the presence of photocatalyst, light and water. Figure 2.10 shows the difference between photosynthesis and photocatalysis.

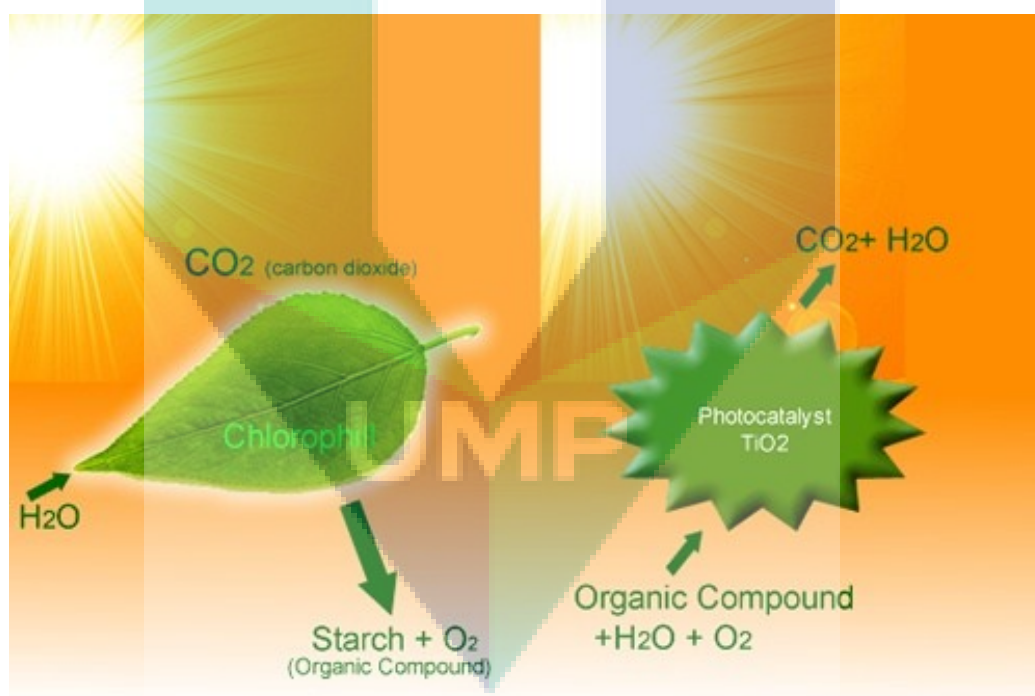


Figure 2.10: Photosynthesis vs photocatalysis

Source: Clean Correct (2015)

2.8 MECHANISM OF PHOTOCATALYSIS

Mechanism of photocatalysis has been explained by Haque et al. (2003). A photocatalyst will accelerate the photoreaction by contact substrate to exciting state with a photoproduct. The molecular orbital of heterogeneous photocatalyst which commonly is semiconductors has a band structure. These bands are valence band (VB) and conduction band (CB) which is characterized by band gap energy (E_{bg}). The semiconductors may be photoexcited to form electron-donor sites (reducing sites) and electron-acceptor sites (oxidizing sites), providing great scope for redox reaction. When the semiconductor is illuminated with light ($h\nu$) of greater energy than that of the band gap, an electron is promoted from the VB to the CB leaving a positive hole in the valence band and an electron in the conduction band as illustrated in Figure 2.11.

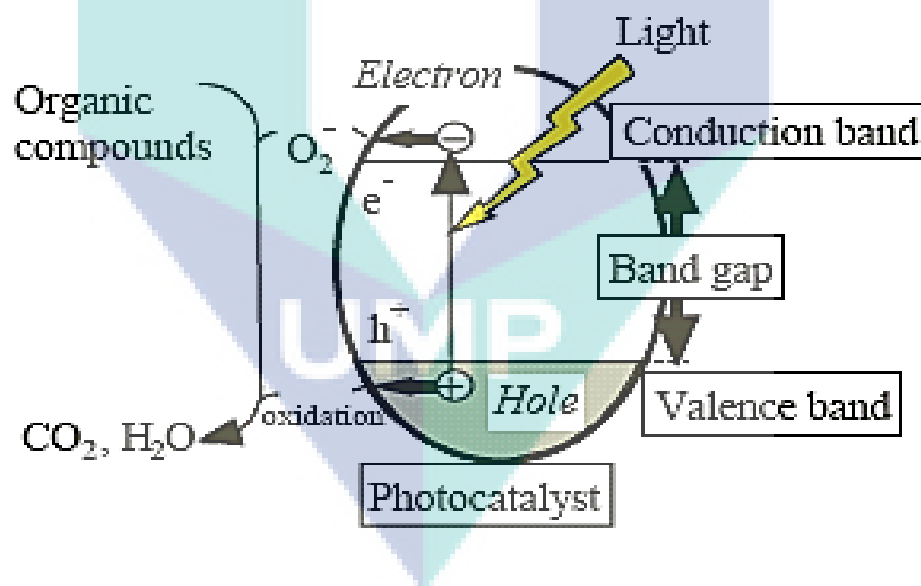
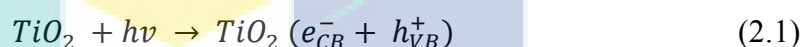


Figure 2.11: Mechanism of photocatalysis

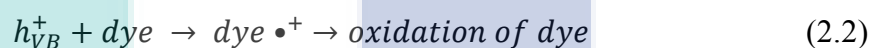
Source: TitanPE Tech. (Shanghai) Inc (2008)

The electron and hole may migrate to the catalyst surface if the charge separation is maintained. h^+_{VB} react with H_2O or $\bullet OH$ to produce hydroxyl radical and e^-_{CB} is reacted with oxygen to generate superoxide radical anion ($O_2^{\bullet -}$). The mechanism equation is explained as:

In the first step, semiconductor materials such as TiO_2 absorbs light and cause the electron-hole pair being generated at the photocatalyst surface (Eq. (2.1))



Secondly, the high oxidation potential of the hole (h^+_{VB}) causes the direct oxidation of the organic matter such as dye and some reactive intermediates are generated (Eq. (2.2)).



Then, hydroxyl radical generate by breakdown the water molecules (Eq. (2.3)) and reacting hydroxyl ion (OH^-) with a hole (Eq. (2.4)).



As a result of reaction of hydroxyl radicals with organic based impurities, the partial or complete mineralization of the organic compounds takes place. Besides that, superoxide anions are generated by the reduction of the molecular O_2 , which may take place by the presence of electrons in the conduction band at the surface of photocatalyst (Eq. (2.4)).

2.9 PHOTOCATALYST

Photocatalyst is a catalyst that needs light in an experiment. Catalyst increases the rate of the reaction without being consumed in the chemical reaction. Hence, photocatalyst is a substance that increases the rate of the reaction under the light permission. There are two type of photocatalyst which are homogeneous photocatalyst and heterogeneous photocatalyst. The reactants and photocatalysts exist in the same phase is called homogenous photocatalysis while reactants and photocatalysts are in different phase is heterogeneous photocatalysis. The common homogeneous photocatalyst is called photo-Fenton system which includes Fe^{+} in H_2O_2 solution. At another side, the most common heterogeneous photocatalysts are semiconductors and transition metal oxides for example TiO_2 . When selecting a photocatalyst in a photocatalysis reaction, the band gap energy of the photocatalyst determines the wavelength of light that can be absorb (Casbeer et al., 2012). As shown in Figure 2.11, there is a band gap difference between VB and CB. Wavelength of the light can be calculated by dividing 1240 eV to band gap energy. Figure 2.12 shows the energy spectrum of the sunlight. It shows that UV light accounts 5% of the total energy while visible light accounts 46% of the total energy.

The logo of UMP (Universiti Malaysia Perlis) is a large, stylized letter 'U' composed of several overlapping triangles in shades of teal, light blue, and yellow. The letters 'UMP' are printed in white, bold, sans-serif font across the bottom of the 'U' shape.

UMP

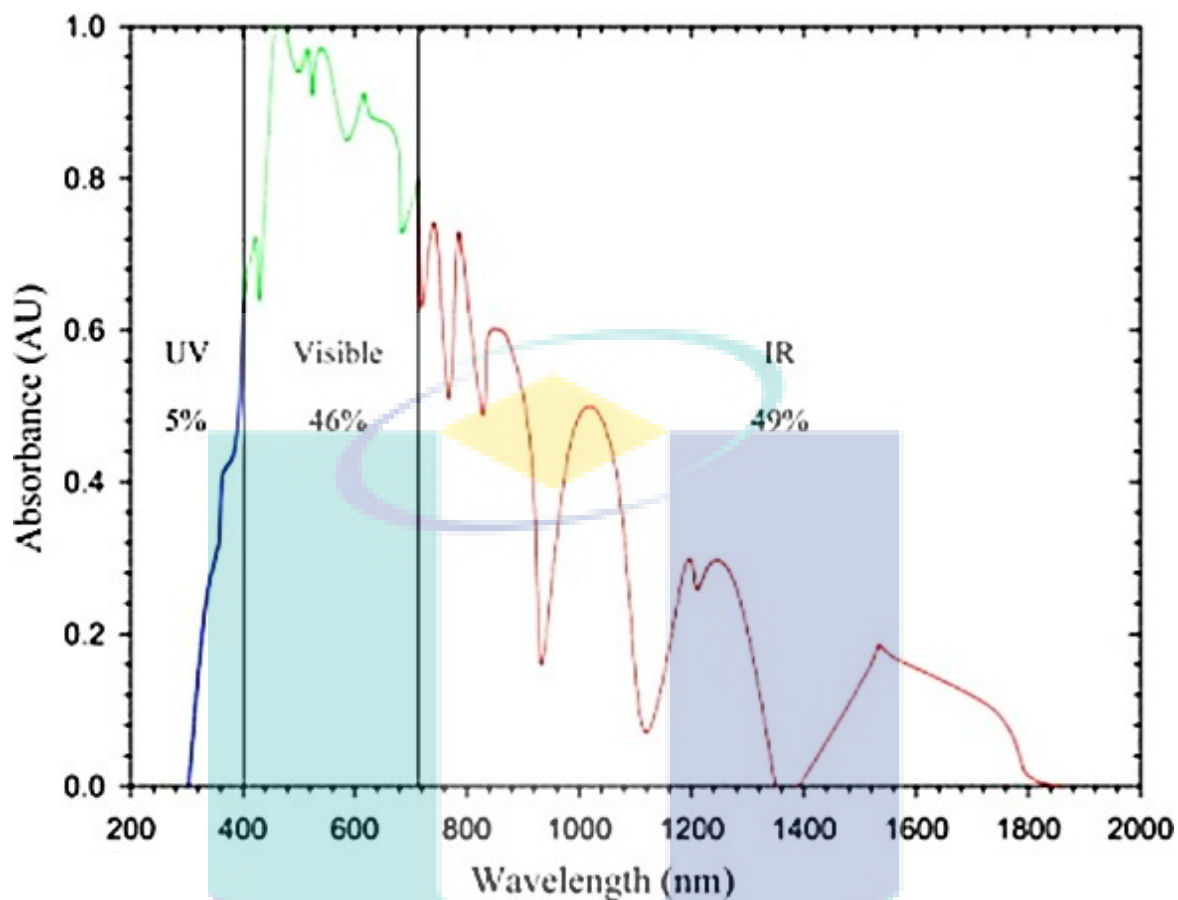


Figure 2.12: Solar energy spectrum

Source: Casbeer et al. (2012)

2.10 TITANIUM OXIDE

The common photocatalyst used in photoreaction is titanium dioxide photocatalyst. Titanium dioxide also known as titanium (IV) oxide or titania with a chemical formula TiO_2 . It is inexpensive, chemically stable, harmless, and has no absorption in the visible region. In addition, TiO_2 is a white color powders that its chemical stability only holds in the dark (Hashimoto et al., 2005). Besides that, TiO_2 has strong oxidizing abilities for the decomposition of organic pollutants, superhydrophilicity, chemical stability, long durability, nontoxicity, low cost, and transparency to visible light. TiO_2 is active under UV

light and particularly effective for photocatalytically breaking down organic compounds. For example, if one puts catalytically active TiO_2 powder into a shallow pool of polluted water and allows it to be illuminated with sunlight, the water will gradually become purified. According to Nakata & Fujishima (2012), TiO_2 photocatalysis is widely used in a variety of applications (refers to Table 2.4). TiO_2 adsorb light undergoing chemical reaction to obtain hydrogen, hydrocarbons, remove pollutants and bacteriaom wall surfaces and in air and water.

However, effective commercial applications of TiO_2 based photocatalyst are hampered by two serious disadvantages. The first is the agglomeration of ultrafine powders resulting in an adverse effect on catalyst performance (Aazam, 2014). The second is the wide band gap of TiO_2 (> 3.1 eV) that restricts its photocatalytic application to the UV zone (200 to 400 nm), which accounts for merely 5% of the solar energy spectrum. Hence, developing an efficient solar energy by modified titania is important. To enlarge the photoactivity of TiO_2 in the photo-treatment, nitrogen-doped titania has been used. By doping TiO_2 with nitrogen, the photocatalytic activity in solar energy can be increased, therefore provides good opportunities for extensive applications such as oxidation of CO, ethanol, gaseous 2-propanol, acetaldehyde, and NO_x and the decomposition of dyes such as methylene blue (Cong et al., 2007).

According to Sato (1986), for the first time, a titania-based material from the mixtures of titanium hydroxide and ammonium calcined at about 400°C showed higher photocatalytic activity in the visible light region (Sato, 1986). Recently, many researchers have studied different techniques to produce nitrogen-doped titanias such as hydrolytic process (Sakthivel and Kisch, 2003), mechanochemical technique (Yin et al., 2004), reactive DC magnetron sputtering (Chen et al., 2004), high temperature treatment of titania under NH_3 flow (Diwald et al., 2004), solvothermal process (Aita et al., 2004) and calcination of a complex of Ti_4p with a nitrogen-containing ligand (Sano et al., 2004).

2.11 APPLICATIONS OF PHOTOCATALYST

Photocatalyst is used in a variety of applications. The most application of photocatalyst is used in reducing environmental pollution. The application can be divided into indoor environment and outdoor environment. The examples for indoor environment are deodorization, antibacterial function, purification of polluted water and air purification. Antifouling protection of exterior, decomposition of dioxins in emission gas from waste incinerators and purification of car exhaust emission are the examples of outdoors environments (Kameyama, 2006). Besides reducing environmental issues, photocatalysis can also be used in bacterial inactivation, producing gas for example H_2 , CH_4 and CO_2 , the inactivation and others applications (Casbeer et al., 2012).

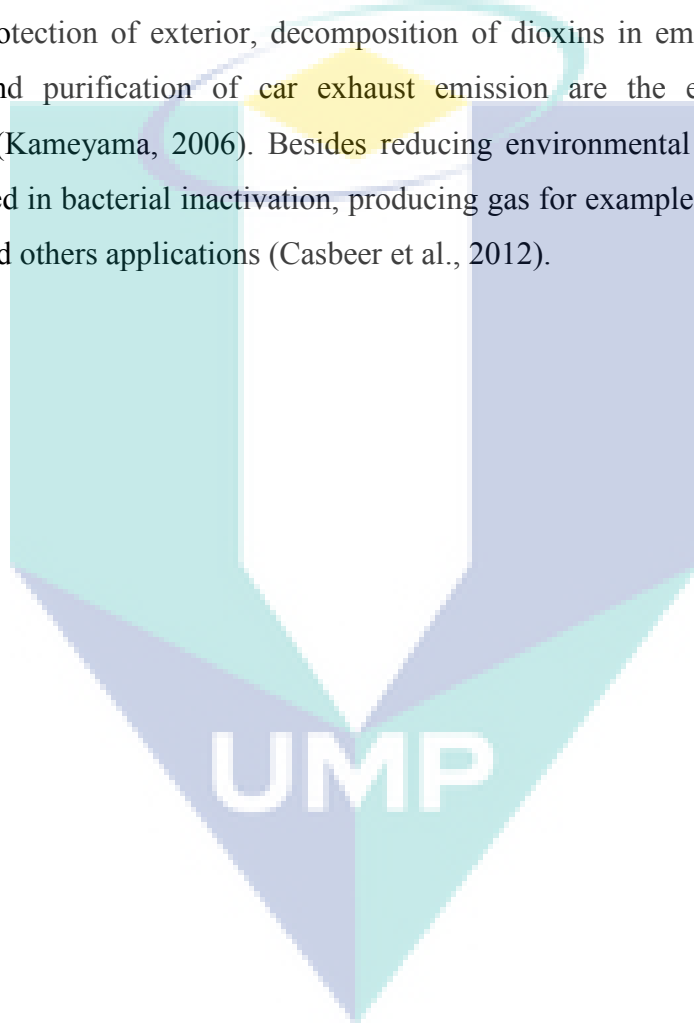


Table 2.4: Application of TiO₂ photocatalysis

Environmental Application	
Air purification	<ul style="list-style-type: none"> • Deodorizing • Removal of air pollutants
Water purification	<ul style="list-style-type: none"> • Removal of hazardous substances • Disinfection
Electric appliance	<ul style="list-style-type: none"> • Refrigerator • Fluorescent light
Residence (exterior)	<ul style="list-style-type: none"> • Painting/Tile • Glass/Tent
Road	<ul style="list-style-type: none"> • Tunnel lighting • Sound insulation wall • Removal of NO_x
Printing	<ul style="list-style-type: none"> • Offset printing
Car	<ul style="list-style-type: none"> • Side mirror
Residence (interior)	<ul style="list-style-type: none"> • Curtain • Wall paper • Removal of residual pesticides • Deodorization
Medical	<ul style="list-style-type: none"> • Hydroponic culture • Cancer treatment • Catheter/Operating room
Energy Application	
Energy conversion	<ul style="list-style-type: none"> • Solar cell
Water splitting	<ul style="list-style-type: none"> • Hydrogen evolution

Source: Nakata and Fujishima (2012)

2.12 FERRITE BASED PHOTOCATALYST

Ferrite based catalyst is a new class of photocatalyst that can function under visible light but much detail remain unknown when it is doped with metal such as magnesium, zinc, copper and others metal. Most of the research of photocatalyst is related to TiO_2 . But, TiO_2 has a wide a wide band gap (3.03 eV rutile and 3.18 eV anatase) and can therefore absorb only a small portion of sunlight (Shihong et al., 2009). Therefore, developing new photocatalysts is important to improve the characteristics of photocatalyst so it can be utilized by visible light. Figure 2.13 and Table 2.5 shows different ferrite based photocatalyst with its band gap energy. As shown from the table, CuFe_2O_4 has a lower band gap energy which is 1.32 eV.

Table 2.5: Band gap energy for different ferrite based photocatalyst

Ferrite	Band Gap (EV)
CaFe_2O_4	1.9
MgFe_2O_4	2.18
ZnFe_2O_4	1.92
NiFe_2O_4	2.19
CuFe_2O_4	1.32

Source: Casbeer et al. (2012)

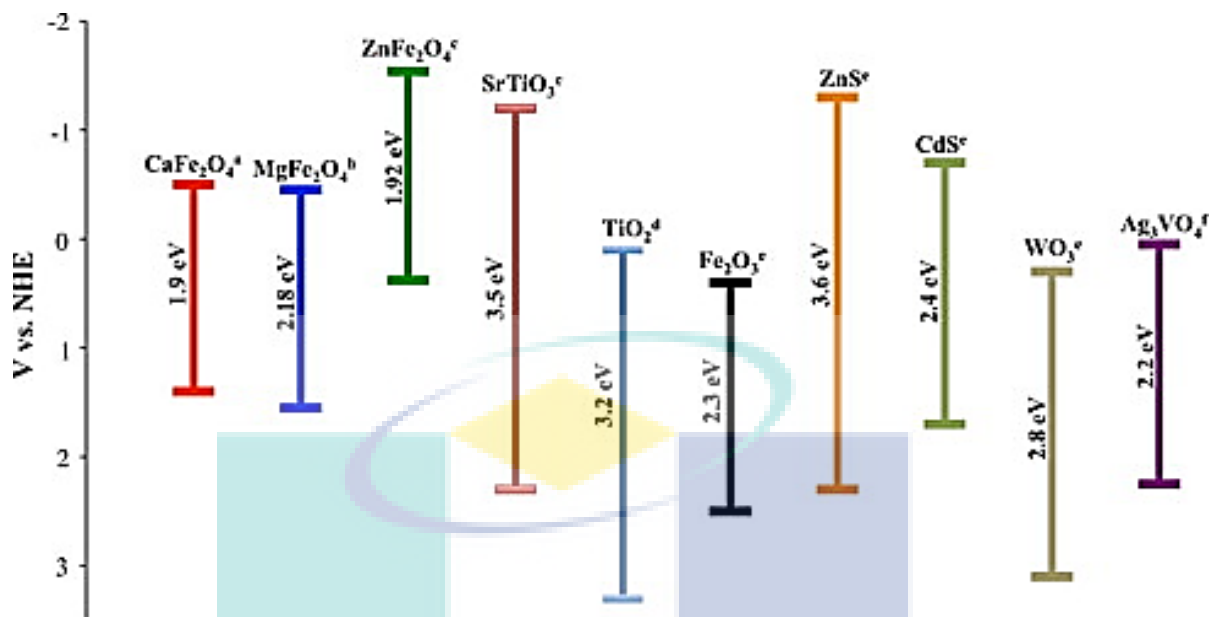


Figure 2.13: Different ferrite based photocatalyst with different band gap energy

Source: Casbeer et al. (2012)

2.13 COPPER FERRITE AS PHOTOCATALYST

Copper ferrite (CuFe_2O_4) is a magnetic spinel material with tetragonal and cubic structures and black in colour. CuFe_2O_4 shows phase transitions, change semiconducting properties, shows electrical switching and tetragonality variation when treated under different conditions in addition to interesting magnetic and electrical properties with chemical and thermal stabilities (Sartale et al., 2003).

Copper ferrite can be prepared by three ways which are solid state reaction, co-precipitation method and sol-gel approach (Yang et al., 2009). The copper over iron ratio is 1:2. The different between these three methods is their calcination temperature. The calcination temperature for solid state method is 1000°C for 2 times while others dry at 80°C and later calcined at 850°C . Besides that, by co-precipitation method, acid or alkaline is added until pH around 9 while sol-gel method, citric acid is added to produce a

transparent mixed sol. According to Yang et al. (2009), copper ferrite synthesized via sol-gel method is better than others two method due to its particle size. Copper ferrite by solid state method has a particle size of 1 μm while by co-precipitation method are irregular in size but by sol-gel method, the nanoparticles are uniform and about 80 nm size.

2.13.1 Previous Study

In the past few years, researchers have done some research on copper ferrite in solving environmental issues and the summary of works is listed in Table 2.6.

Table 2.6: Previous study done by researcher

Title	Authors	Parameter	Conclusion
Magnetic ordered mesoporous copper ferrite as a heterogeneous Fenton catalyst for the degradation of imidacloprid	Y. Wang et al., 2014	<ul style="list-style-type: none"> • CuFe_2O_4 and CoFe_2O_4 • H_2O_2 • Imidacloprid 	The ordered mesoporous CuFe_2O_4 was successfully synthesized and used as heterogeneous Fenton-like catalyst for removing imidacloprid in the presence of H_2O_2 .
Photocatalytic activity evaluation of tetragonal CuFe_2O_4 nanoparticles for the H_2 evolution under visible light irradiation	H. Yang et al., 2009	<ul style="list-style-type: none"> • Copper ferrite • Visible light • aqueous oxalic acid solution 	Photocatalytic H_2 evolution can take place efficiently on the as-obtained CuFe_2O_4 from aqueous oxalic acid solution under visible light irradiation.

Table 2.6: Previous study done by researcher (continued)

Title	Authors	Parameter	Conclusion
Photocatalytic ozonation of dyes using copper ferrite nanoparticle prepared by co-precipitation method	Mahmoodi, 2011	<ul style="list-style-type: none"> • Copper ferrite • Visible light • Reactive Red 198 (RR198) and Reactive Red 120 (RR120) 	The reaction parameters studies showed that dyes were decolorized and degraded using CF nanoparticle
Facile preparation of sphere-like copper ferrite nanostructures and their enhanced visible-light-induced photocatalytic conversion of benzene	Shen et al., 2013	<ul style="list-style-type: none"> • Copper ferrite • Xenon lamp • Benzene 	The as-prepared CuFe_2O_4 nanospheres demonstrated advancement over CuFe_2O_4 nanoparticles in photocatalytic conversion of benzene under Xe lamp irradiation
Efficient degradation of atrazine by magnetic porous copper ferrite catalyzed peroxymonosulfate oxidation via the formation of hydroxyl and sulfate radicals	Guan et al., 2013	<ul style="list-style-type: none"> • Copper ferrite • atrazine solutions 	The magnetic porous CuFe_2O_4 , synthesized by a sol-gel method, was applied to the catalysis of peroxides. CuFe_2O_4 exhibited a notable catalytic activity to PMS for atrazine degradation but almost no catalytic activity to PDS and H_2O_2 .

2.14 ADVANCED OXIDATION PROCESS

Advanced oxidation process (AOPs) is a chemical treatment that decompose and mineralize organic materials in both liquids and gas phases (Mehrjoui, 2012). AOPs is defined “as near ambient temperature and pressure water treatment processes which involve the generation of hydroxyl radicals in sufficient quantity to effect water purification” (Glaze et al., 1987). AOPs mineralize pollutants into harmless and less compounds such as carbon dioxide and water. This technology destroys chemical structure as compare to conventional methods such as filtration, adsorption which are non-destructive physical separation method. Conventional methods only separate pollutants or transferring them to other phase of waste. Oxidative radicals are highly produced to degrade pollutants. AOPs can be divided into two sections which are methods that do not use radiation and methods that use radiation (photochemical). Besides that, AOPs can also be classified as homogeneous and heterogeneous process.

Table 2.7 shows the examples of AOPs for each category. The efficient of AOPs is based on the highly reactive radicals that having powerful oxidizing species. Hydroxyl radical is the second strongest oxidants after fluorine and it can be produced from many ways according to different type of AOPs. Table 2.8 shows standard reduction potentials of some oxidants.

AOPs involving in two stages. The first stage is forming strong oxidants while the second stage is reacting between oxidants and pollutants (Kommineni et al., 2011). The electrophilic addition of a hydroxyl radical to organic compounds that contain a π bond leading to the formation of organic radicals. Then the hydrogen abstraction by reacting the hydroxyl radical with a saturated aliphatic compound and electron transfer with reduction of the hydroxyl radical into a hydroxyl anion by an organic substrate. The equation of oxidants such as hydroxyl radicals attack onto organic pollutants as shown below (Mota et al., 2008):

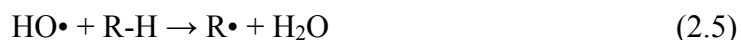


Table 2.7: Types and classification of advanced oxidation processes

Non-photochemical	Photochemical
Homogeneous Processes	
<ul style="list-style-type: none"> • Ozonation in alkaline media (O_3/HO^-) • Ozonation with hydrogen peroxide ($\text{O}_3/\text{H}_2\text{O}_2$) • Fenton ($\text{Fe}^{2+}$ or $\text{Fe}^{3+}/\text{H}_2\text{O}_2$) • Electro-oxidation • Electrohydraulic discharge-ultrasound • Wet air oxidation • Supercritical water oxidation (SCWO) 	<ul style="list-style-type: none"> • Photolysis of water in vacuum ultraviolet (VUV) • UV/H_2O_2 • UV/O_3 • UV/$\text{O}_3/\text{H}_2\text{O}_2$ • Photo-Fenton (Fe^{2+} or $\text{Fe}^{3+}/\text{H}_2\text{O}_2/\text{UV}$)
Heterogeneous Processes	
<ul style="list-style-type: none"> • Catalytic wet air oxidation (CWAO) 	<ul style="list-style-type: none"> • Heterogeneous photocatalysis: ZnO/UV, SnO₂/UV, TiO₂/UV, TiO₂/H₂O₂/UV

Source: Domenech et al. (2001) and Ribeiro et al. (2015)

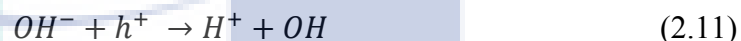
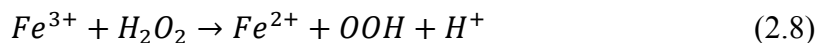
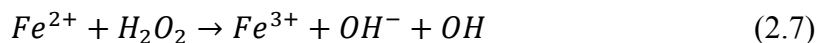
Table 2.8: Standard reduction potential of oxidants compared with normal hydrogen electrode (NHE, $E^\circ = 0$ V)

Oxidant	Oxidation Potential (V)
Fluorine (F ₂)	3.03
Hydroxyl radical (OH•)	2.80
Atomic oxygen	2.42
Ozone (O ₃)	2.07
Hydrogen peroxide (H ₂ O ₂)	1.78
Perhydroxyl radical	1.70
Potassium permanganate (KMnO ₄)	1.68
Hypobromous acid	1.59
Chlorine dioxide (ClO ₂)	1.57
Hypochlorous acid	1.49
Hypoiodous acid	1.45
Chlorine (Cl ₂)	1.36
Bromine (Br ₂)	1.09
Iodine (I ₂)	0.54

Source: Legrini et al., (1993) and Mota et al. (2008)

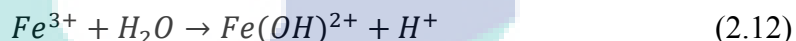
2.14.1 Fenton Reaction

Oxidants such as hydrogen peroxide (H₂O₂) are added to the reaction mixture in order to further enhance the reaction. A Fenton system reaction is shown in Eq. (2.7) to (2.11):

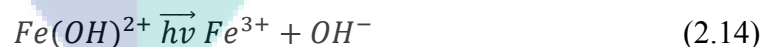


2.14.2 Photo-Fenton Reaction

Photo-Fenton process is a process when Fe^{3+} ions are added to the H_2O_2/UV process. The reaction is shown as following:



When the reaction is exposed to light, it will decompose into Fe^{3+} and OH^- ions as shown in the following equation:



2.14.3 Properties of Hydrogen Peroxide

Hydrogen peroxide (H_2O_2) is a colourless liquid and slightly more viscous than water in its pure form. However, it is normally used in aqueous solution for safety reason. H_2O_2 is the simplest peroxide which consists of a compound with an oxygen-oxygen single bond. It is used as a strong oxidizer, bleaching agent and disinfectant. H_2O_2 is soluble in

water, ether, alcohol but insoluble in petroleum ether (Identity, 1995; Jones and Clark, 1999). Table 2.9 shows the physical properties of H_2O_2 .

Table 2.9: Properties of hydrogen peroxide

Physical Properties	
Odor	Slightly sharp
Appearance	Light blue colour, colourless in solution
Molecular weight	34.0147 g/mol
Density (20°C, 30%)	1.135 g/cm ³
Viscosity	1.245 c.p. at 20°C
Melting point	-0.43°C
Boiling point (760 mm Hg)	150.2°C
Vapor pressure	5 mm Hg at 30°C
Refractive index	1.4061
Acidity	11.75

Source: Jones and Clark (1999) and Pure Water Global Inc. (1995)

2.14.4 Previous Study

In the past few years, researchers have done some research on photo-Fenton in wastewater treatment.

Table 2.10: Previous work done by researcher

Title	Author	Parameter	Conclusion
Magnetic ordered mesoporous copper ferrite as a heterogeneous Fenton catalyst for the degradation of imidacloprid	Y. Wang et al., 2014	<ul style="list-style-type: none"> • CuFe_2O_4 and CoFe_2O_4 • H_2O_2 • Imidacloprid 	The ordered mesoporous CuFe_2O_4 was successfully synthesized and used as heterogeneous Fenton-like catalyst for removing imidacloprid in the presence of H_2O_2 .
Magnetic heterogeneous Fenton catalyst for the degradation of RhB in the presence of oxalic acid	S. Q. Liu et al., 2012	<ul style="list-style-type: none"> • Nickel ferrite • Ultraviolet–visible lamp • Rhodamine B (RhB) 	The resulting magnetic species exhibits photo-Fenton catalytic features for organic pollutants in the presence of oxalic acid
Mesoporous Zinc ferrite: Synthesis, characterization, and photocatalytic activity with H_2O_2 /visible light	Su et al., 2012	<ul style="list-style-type: none"> • Zinc ferrite • Xenon arc lamp • Acid Orange II 	The photocatalytic degradation of AOII in the H_2O_2 – ZnFe_2O_4 –visible light system followed pseudo first-order kinetics.
Decolorization of synthetic dyes by hydrogen peroxide with heterogeneous catalysis by mixed iron oxides	Baldrian et al., 2006	<ul style="list-style-type: none"> • $\text{MO-Fe}_2\text{O}_3$; M: Fe, Co, Cu, Mn • Bromophenol Blue, Chicago Sky Blue 6B, Evans Blue, Cu Phthalocyanine, Eosin Yellowish, Naphthol Blue Black, Phenol Red, Poly B-411 and Reactive Orange 16 	The most effective catalyst $\text{FeO-Fe}_2\text{O}_3$ (25 mg/mL with 100 mmol/L H_2O_2) produced more than 90% decolorization of 50 mg/L Bromophenol Blue, Chicago Sky Blue, Evans Blue and Naphthol Blue Black within 24 h.

CHAPTER 3

METHODOLOGY

3.1 INTRODUCTION

In this chapter, the copper ferrites (CuFe_2O_4) preparation procedure is described followed by the characterization of the photocatalyst. The characterization techniques employed in the current work were nitrogen (N_2) physisorption for textural property determination, UV-vis DRS scanning for band gap energy determination, field emission scanning electron microscopy-energy dispersive X-ray (FESEM-EDX) for surface morphology capturing and element determinations, X-ray diffraction (XRD) technique for obtaining crystalline structure diffraction pattern and particle size analyser to determine the particle size distribution. The methods of photoreaction glycerol degradation, sample analysis, effects of reaction parameters and factorial analysis by Design Expert are presented too.

3.2 MATERIALS

3.2.1 Chemicals

The chemicals needed in this study are listed in the Table 3.1. Apart from the ultrapure water, all the chemicals listed in Table 3.1 were procured either from Sigma-Aldrich, Merck or Fischer Chemical. All these chemicals were used without further

purification. The ultrapure water was obtained from the Millipore Elix 5-UV unit which is readily available in the laboratory of Universiti Malaysia Pahang (UMP). Ultrapure water was used for the catalyst preparation and preparation of different concentrations of reactants.

3.2.2 Gases

The gases required in the study are listed in Table 3.2. All gases used in this research were supplied by MOX-Linde Gases Sdn. Bhd. Table 3.2 also lists the purity of the gases and their application in this study.

Table 3.1: List of chemicals

Chemical	Purity	Brands	Application
Copper (II) nitrate trihydrate $\text{Cu}(\text{NO}_3)_2 \cdot 3\text{H}_2\text{O}$	> 98%	Sigma-Aldrich	Catalyst preparation
Iron (III) nitrate nonahydrate $\text{Fe}(\text{NO}_3)_3 \cdot 9\text{H}_2\text{O}$	> 98%	Sigma-Aldrich	Catalyst preparation
Citric acid ($\text{C}_6\text{H}_8\text{O}_7$)	$\geq 99.5\%$	Sigma-Aldrich	Catalyst preparation
Glycerol ($\text{C}_3\text{H}_8\text{O}_3$)	$\geq 99\%$	Sigma-Aldrich	Photoreaction
Hydrogen peroxide (H_2O_2)	30%	Merck	Photoreaction
Acetonitrile ($\text{C}_2\text{H}_3\text{N}$)	HPLC grade	Fisher Chemical	Mobile phase HPLC

Table 3.2: Lists of gases

Gases	Purity	Application
N_2/He mixture	$\text{N}_2=30.03\%$, He=balance	N_2 physisorption
He	> 99.996%	N_2 physisorption
N_2	> 99.99%	N_2 physisorption

3.3 PHOTOCATALYST PREPARATION

The photocatalyst used in the present study was CuFe_2O_4 . It was synthesized via sol-gel method adapted from previous works (Shen et al., 2013; Yang et al., 2009). Firstly, 0.005 mol $\text{Cu}(\text{NO}_3)_2$ and 0.010 mol $\text{Fe}(\text{NO}_3)_3$ were co-dissolved in 50 ml distilled water. The mixed solution was subsequently added into 100 ml of 0.3 M citric acid solution. This step would produce a transparent mixed sol. During this mixing procedure, the temperature was controlled at around 80°C until transparent and viscous gel was obtained. The as-synthesized gel was subsequently transferred into an oven and kept at 140°C for 3 h. The dried photocatalyst was then air-calcined at 850°C for 3 h employing a ramping rate of $10^\circ\text{C min}^{-1}$. The calcined catalyst was then ground for catalyst characterization and photocatalytic Fenton study.

3.4 CATALYST CHARACTERIZATION

3.4.1 N_2 Physisorption

The specific surface area of photocatalyst was determined by N_2 physisorption. The most commonly employed equation is the Brunauer-Emmett-Teller (BET) model. The BET equation (Brunauer et al., 1938) is derived for multilayer adsorption and based on the relationship between the volume of gas physically adsorbed and the total area of adsorbent as shown in Eq. (3.1):

$$\frac{P}{V(P_s - P)} = \frac{1}{cV_m} + \frac{(c-1)P}{cV_m P_s} \quad (3.1)$$

where

P = gas pressure (Pa)

P_s = saturation pressure of the adsorbate gas (Pa)

V = volume of gas adsorbed (mL)

V_m = volume of gas adsorbed corresponding to monolayer coverage (mL)

c = a characteristic constant of the adsorbate

The empty burette was degassed and weighed. The empty burette was used as baseline of the samples. Around 0.3-0.5 g sample was added into the burette and then installed to the degasser port. The sample was then degassed overnight (6-12 h) under degassing temperature of 573 K to remove the humidity and others gases. It would have a clean surface for adsorption if the sample was degassed overnight at a high temperature. The burette with the sample was measured again to obtain an accurate mass value for the sample. After degassing the sample, the next step was analysing the sample to obtain the surface area of the sample. The burette with the sample was installed to the analysis port of Thermo Scientific Surface Gas Adsorption Porosimeter instrument. The method of unknown surface area was selected for surface acquisition software. Subsequently, N₂ was immersed into the burette to obtain the adsorption and desorption isotherm. The result was compared with the blank burette by deducting the area using He physisorption.

The density of sample which was required during the BET specific surface area calculation, was obtained from the Micromeritics AccPyc II 1340. The 3.5 cm³ sample chamber and sample were weighed. The volume of the sample was measured by He gas displacement at a pressure of 19.5 psig. The density of the sample was measured for eight cycles to enhance the accuracy.

3.4.2 UV-vis DRS

UV-vis DRS is a standard technique used to determine the optical absorption properties of materials. In this study, this technique was used to investigate the band gap energy of the photocatalyst. This technique involves light generation from a source lamp. The light is then dispersed into its constituent wavelengths in a monochromator which results in a narrow band of the dispersed spectrum passing from the exit slit of the monochromator. Suitable optics are used to lead this light, of a narrow wavelength band, to the sample to be measured. A sample with a UV/Visible chromophore sample absorbs a

certain amount of light and the remaining light is detected by a suitable detector in the spectrophotometer (Cecil Instruments, 2006). The sample has to be sufficiently thick that all incident light is absorbed or scattered before reaching the back surface of the sample; typically a thickness of 1 - 3 mm is required (Ebraheem and El-Saied, 2013). In the current work, this analysis was conducted by Lambda 1050 UV/Vis/NIR spectrophotometer.

3.4.3 Field Emission Scanning Electron Microscopy (FESEM) - Energy Dispersive X-ray (EDX)

Field Emission Scanning Microscopy Analysis (FESEM) is a non-destructive analytical technique to investigate molecular surface structures such as sample morphology or texture, sample topography, sample compositions, crystalline structure and orientation of materials. This analysis was carried out using JEOL JSM-7800F. A small amount of sample was put on the sample holder and inserted into the detector. FESEM uses a focused high energy beam of electrons to generate an image or to analyse the specimen. Electron emitters from field emission gun was used. These types of electron emitters can produce up to 1000X the emission of a tungsten filament. However, they required higher vacuum conditions. After the electrons beam exit the electron gun, they are then confined and focused into a thin focused, monochromatic beam using metal apertures and magnetic lenses. Finally, detectors of each type of electrons are placed in the microscopes that collect signals to produce an image of the specimen (Alyamani and Lemine, 2012). Generally, data can be collected from a selected area of the surface or a 3-dimentional image. The magnifications can be adjusted to enlarge the surface of the sample.

Energy Dispersive usually comes with FESEM for better analysis results. In fact, in our analysis, both FESEM-EDX was carried out using the same equipment with the same parameters. Figure 3.1 shows the system of FESEM-EDX.

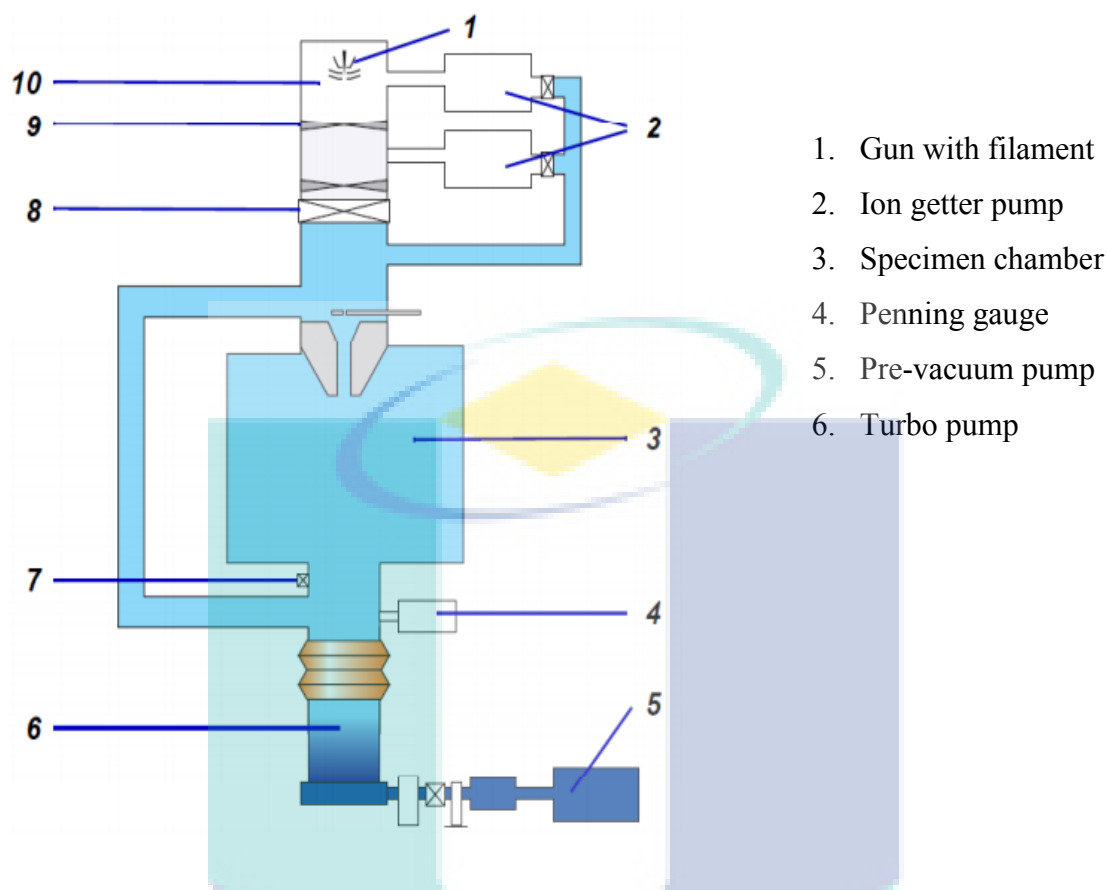


Figure 3.1: FESEM-EDX system

Source: SIGMA FESEM (2012)

3.4.4 X-ray Diffraction (XRD)

X-ray diffraction (XRD) was used to determine the crystal phase structure of the photocatalyst. XRD is a non-destructive analytical technique which is widely used for the identification of structure, crystalline phases, and also sizes of crystallites of natural or synthetic materials (Casbeer et al., 2012). Powder, solids and others can use this technique to determine its structure. The sample full with sample holder will have more accurate results. The analysis in the current work was carried out using Rigaku MiniFlex II. XRD patterns or also known as “fingerprint” varied based on the internal structure of the material and hence the characteristics can be identified.

From the XRD pattern, the mean crystallite size can be calculated by Scherrer equation as shown in Eq. (3.2) (Warren, 1969).

$$D = \frac{k_{sch} \lambda}{\beta_d \times \cos \theta} \quad (3.2)$$

where

D = the crystalline size (nm)

λ = wavelength of X-ray (nm)

β_d = angular width at half maximum intensity (radian)

θ = Bragg's angle degree

k_{Sch} = Scherrer constant and equals to 0.93

XRD measurement was carried out on a Philips X' Pert system using $\text{CuK}\alpha$ ($\lambda = 1.542 \text{ \AA}$) at 30 kV and 15 mA. The specimen was initially ground to fine powder ($< 100 \mu\text{m}$). It was then placed on a glass specimen holder and pressed using a glass slide. Scanning of sample was then performed from 20° to 90° at a speed of 1° min^{-1} . Peaks obtained from the analysis were matched with The International Centre for Diffraction Data (ICDD) database search match interpretation method to determine the types of crystallite phase present.

3.4.5 Particle Size Analyser

Particle size distribution indicates the sizes of particles presenting its proportions in the sample particle measured. Laser diffraction (LD) method is a primary method to examine the size distribution. This method was fast and automated. The LD method is based on the spatial distribution of scattered light, is a function of the particle size of the analysed sample. Smaller particles scatters light of a lower intensity to larger angles while the larger particles scattered light of stronger intensity toward smaller angles (Stojanović et al., 2010). In this work, the size distribution of CuFe_2O_4 was determined by Malvern

Mastersizer 2000 particle size analyser. The sample of CuFe_2O_4 was dispersed in a suitable medium that passed through the focus beam of light and scattered the light at characteristic spatial angles. This equipment used two light sources which are HeNe laser with a wavelength of 633 nm and LED that emits blue light with a wavelength of 455 nm as shown in Figure 3.2. The Mastersizer 2000 software was used to run the analysis and calculate the particle size distribution.

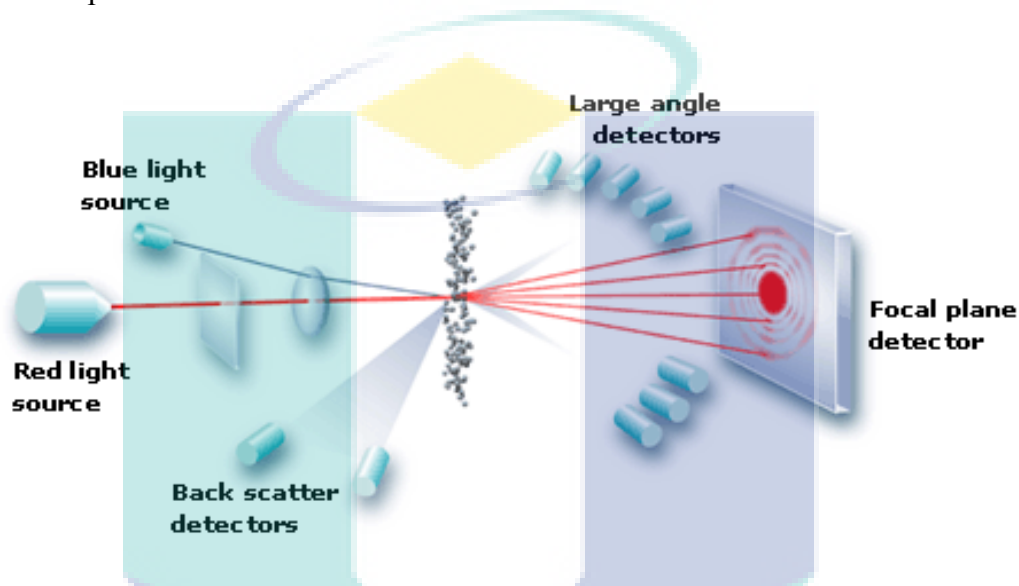


Figure 3.2: Sketch of LD instrument part

Source: Particle Analytical (2015)

3.4.6 Summary of the Catalyst Characterization

Table 3.3 summarizes all the catalyst characterization and the analyses used for characterizing the CuFe_2O_4 .

Table 3.3: Summary of catalyst characterization techniques

Characterization	Analyses	Equipment Used
Specific surface area	BET analysis	Thermo Scientific Surfer
Crystalline structure	XRD analysis	Rigaku MiniFlex II
Surface morphology	FESEM-EDX analysis	JEOL JSM-7800F
Band gap energy	UV-vis adsorption	Lambda 1050
Particle size distribution	Particle size analyser	Malvern Mastersizer 2000

3.5 PHOTOCATALYTIC FENTON REACTION STUDIES

3.5.1 Photocatalytic Reactor

The photocatalytic Fenton reaction experiment was carried out in a stirred batch reactor. The photocatalytic reactor contains two parts as shown in Figure 3.3. The upper part is a quartz cell (300 ml) with a circulating water jacket and the lower part comprised of a Xenon (Xe) lamp (250 W) placed inside the quartz cell. In all the experiments, the reaction temperature was kept at room temperature by the means of circulating water.

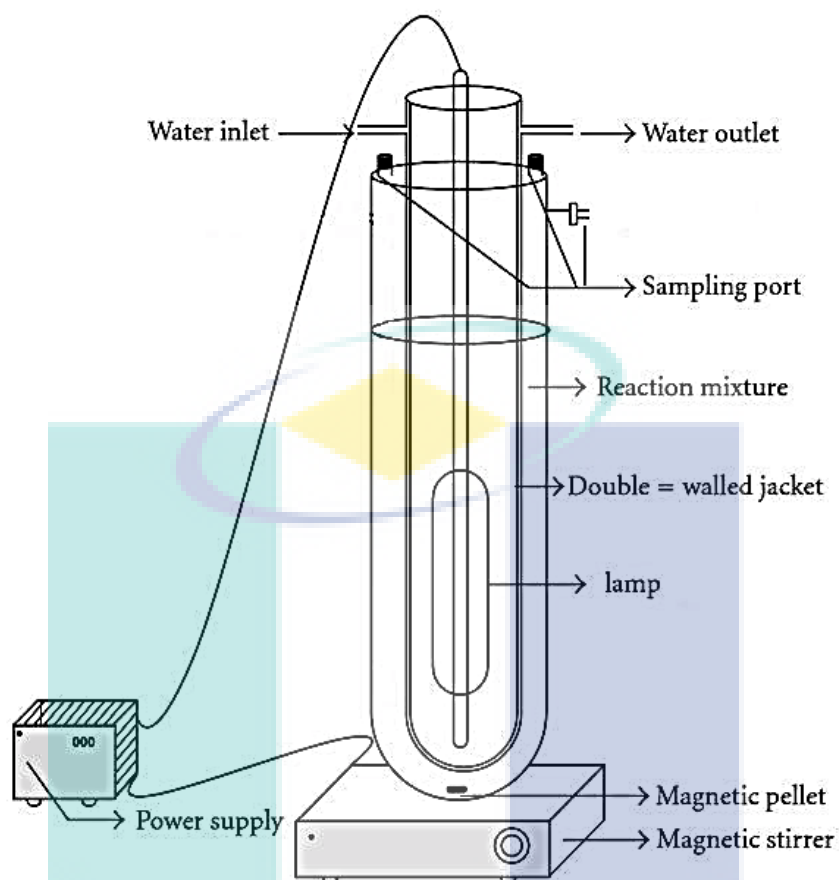


Figure 3.3: The experiment setup for photoreaction studies

Source: Mohamed and Aazam (2012)

3.5.2 Sample Analysis

Quantitative and qualitative analyses of glycerol solution before and after photocatalytic Fenton reaction was carried out using Agilent 1200 Series HPLC equipped with refractive index (RI) detector. The liquid chromatography (LC) column used in this study was Agilent Zorbax Carbohydrate 5 μm (inner diameter of 4.6 and height of 250 mm) column with the flow rate of 1.0 mL/min and the injection volume of 10 μm . The mobile phase used throughout the HPLC analysis was acetonitrile (ACN) diluted with ultrapure water in a ratio of 0.7:0.3. Prior to any HPLC analysis, the mobile phase must be filtered

using nylon membrane with the pore size of 0.2 μm and then degassed using ultrasonic bath at room temperature for 30 min.

3.6 PHOTOCATALYTIC FENTON REACTION

3.6.1 Experimental Procedure

Figure 3.4 shows the experimental setup for conducting the photo-Fenton reaction. For the reaction study, around 200 mL of glycerol solution was irradiated with visible light. Before the experiment, the required amount of photocatalyst was weighed and dispersed into the 200 mL of glycerol solution. Then, the reaction was left in dark while rigorously stirred for 30 min to attain equilibrium. Later, the reactor was exposed to the light to initiate the reaction. About 5 ml of liquid sample was collected each time of sampling, for analysis. The collected samples were subsequently analysed by Agilent 1200 Series HPLC. All the experiments were repeated twice to get an average value.

3.6.2 Photocatalytic Fenton Degradation of Glycerol

In order to be sure that the glycerol decomposition was mainly due to the photocatalytic Fenton effect and not by photodecomposition, comparison experiments were carried out with 0.1 g/L of CuFe_2O_4 and without CuFe_2O_4 photocatalyst in the presence of 68.41 mM glycerol solution and 819.5 mM H_2O_2 under visible light irradiation. In addition, experiment with 0.1 g/L of CuFe_2O_4 in the presence of 68.41 mM glycerol solution and 819.5 mM H_2O_2 was also carried with and without the exposure of light; this study intended to determine whether the catalyst required the light source for the reaction to occur. In the presence of CuFe_2O_4 photocatalyst, the reaction media was left-stirring for 30 min to attain adsorption equilibrium before the visible light was turned on.

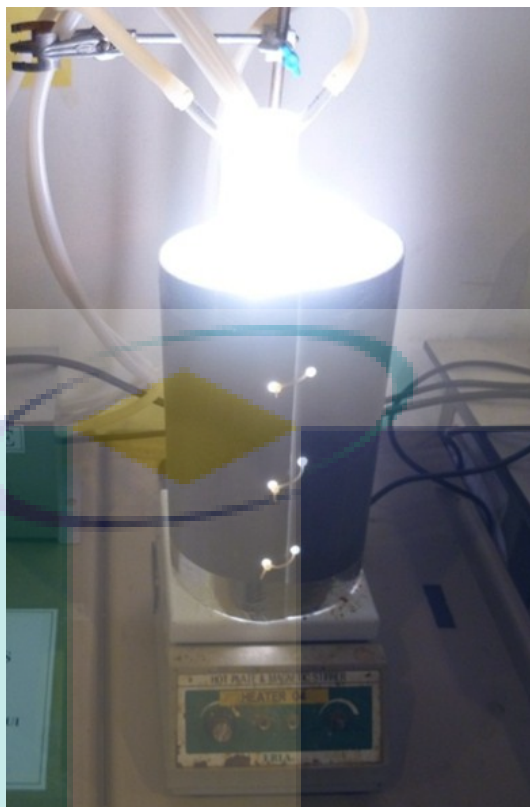


Figure 3.4: The setup of photoreaction

3.6.3 Adsorption Study

An adsorption experiment was conducted at 0.1 g/L CuFe_2O_4 photocatalyst, 68.41 mM glycerol concentration and 819.5 mM H_2O_2 concentration without light irradiation. This experiment was carried out in a quartz beaker wrapped with aluminium foil. Liquid sample was taken after four hours experiment and analysed by Agilent 1200 Series HPLC.

3.6.4 Effect of Operating Parameters

Degradation of glycerol was measured at different operating parameters. The parameters such as catalyst loading, concentration of glycerol and concentration of H_2O_2 considered as an important parameter in this study. All the experiments were conducted in room temperature.

3.6.4.1 Effect of Photocatalyst

The effects of photocatalyst loadings on glycerol degradation were studied by reacting 200 mL of 819.5 mM glycerol concentration and 819.5 mM H₂O₂ concentration. Different amount of CuFe₂O₄ photocatalyst loadings were studied, viz. 0.1, 1.0, 2.0 and 5.0 g/L (Guan et al., 2013; Y. Wang et al., 2014). 0.1g/L CuFe₂O₄ photocatalyst loading was chosen as the minimum loadings because below these loadings, the glycerol degradation is nearly to photolysis.

3.6.4.2 Effect of Initial Glycerol Concentration

The effects of initial glycerol concentration were investigated. 0.1 g/L CuFe₂O₄ was added into 200 mL of glycerol concentration. By referencing to pervious researcher (Augugliaro et al., 2010; Panagiotopoulou et al., 2013) and the limitation of glycerol concentration can be detected by HPLC, the different glycerol concentration selected was 27.36, 41.05, 54.73, 68.41 mM. These experiments were performed at a fixed 819.5 mM H₂O₂ concentration.

3.6.4.3 Effect of Initial H₂O₂ Concentration

The effects of H₂O₂ concentration (163.9, 327.8, 491.7, 655.6 and 819.5 mM) on glycerol degradation was discussed by referencing to pervious researcher (Wang et al., 2014). Besides that, below 163.9mM H₂O₂ concentration, it is insufficient of OH radicals to degrade the glycerol solution. These experiments were conducted in 200 mL of a fixed 68.41 mM glycerol concentration and employing 0.1 g/L of CuFe₂O₄.

3.6.5 Factorial Analysis for Degradation of Glycerol

In general there are several factors that may affects degradation of glycerol, which has been previously discussed. In an un-optimized reaction, there might exist factors which do not have significant, or any effect on the reaction. Classically, experiments were

designed to investigate the effect of each factor in a manner where, one factor is manipulated at a time and all other independent factors are held constant (Lazić, 2004). However, when the number of factors increases, it is difficult to analyze the large amount of data systematically. Factorial analysis was introduced to screen the factors which are relevant to the reaction, and explore possible interaction between factors in a systematic order.

This study applies 24 full factorial experimental design with previously discussed factors using Design Expert version 7.0.0 (Statease Inc., USA). In the factorial study, all the factors has two level which is the high level (+1) and the low level (-1) summarized in Table 3.4. The full factorial experimental design devised 16 experimental runs as listed in Table 3.5 that been carried out and analyzed statistically using Design Expert version 7.0.0 (Statease Inc., USA).

Table 3.4: Factor and their designated low and high value

Factor	Units	Low Value (-1)	High Value (+1)
A: Time	h	1	4
B: Glycerol concentration	mM	27.36	68.4
C: H ₂ O ₂ concentration	mM	163.9	819.5
D: CuFe ₂ O ₄	g/L	0.1	5

3.6.5.1 Validation Experiments

Following the design and analysis of the experiment, the best condition was proposed by the using factorial model to predict the highest possible glycerol degradation rate that can be achieved within the range of factor studied. Experiments were conducted according to the suggested experimental conditions and results of the experiment were compared with the suggested results to verify the significance of the factorial model. An

error below 10% was desired between the predicted and experimental degradation rate of glycerol, calculated using the following equation.

$$Error(\%) = \frac{|\text{predicted value} - \text{experimental value}|}{\text{experimental value}} \times 100\% \quad (3.3)$$

Table 3.5: Proposed runs by Design Expert

Std	Factor 1	Factor 2	Factor 3	Factor 4
	A:Time h	B:Glycerol Concentration mM	C:H ₂ O ₂ Concentration mM	D:CuFe ₂ O ₄ g/L
1	1	27.36	163.9	0.1
2	4	27.36	163.9	0.1
3	1	68.4	163.9	0.1
4	4	68.4	163.9	0.1
5	1	27.36	819.5	0.1
6	4	27.36	819.5	0.1
7	1	68.4	819.5	0.1
8	4	68.4	819.5	0.1
9	1	27.36	163.9	5
10	4	27.36	163.9	5
11	1	68.4	163.9	5
12	4	68.4	163.9	5
13	1	27.36	819.5	5
14	4	27.36	819.5	5
15	1	68.4	819.5	5
16	4	68.4	819.5	5

3.6.6 Measurement of Photocatalytic Reaction Performance

Selection of the responses is an important issue of a preliminary study in any experimental design. A correct definition of research objective means correct selection of the responses. A response has to be fulfil certain conditions such as quantitative, singular, statistically effective, universal, physically realistic, simple, and easily measurable to become a research subject (Lazić, 2004). In this study, degradation rate of glycerol is the chosen response to measure the performance of the photocatalytic Fenton reaction. The photodegradation (X) is given by:

$$X(\%) = \frac{C_{AO} - C_A}{C_{AO}} \times 100 \quad (3.4)$$

where

C_{AO} = the glycerol initial concentration (mM)

C_A = the instantaneous glycerol concentration (mM)

3.7 SAMPLES DETECTION USING HPLC

The collected sample was analysed using Agilent 1200 Series high-performance liquid chromatography (HPLC). Before analysing the samples, the column was flushed with mobile phase until a steady baseline was obtained by the refractive index (RI) detector. The column operating temperature was 30°C while acetonitrile/water as mobile phase was 70%/30%. The flow rate was set at 1.0 mL/min and the sample volume injected into the column was 10 µL. All the samples were always pre-filtered using nylon syringe filter of 0.2 µm to avoid the plugging of the column inert. Post analysis, the column was flushed with pure acetonitrile at the rate of 0.4 mL/min to wash the column and for long term storage.

CHAPTER 4

RESULTS AND DISCUSSION

4.1 INTRODUCTION

This chapter consists of three major sections. Section 4.2 presents the characterization of the CuFe_2O_4 photocatalyst whereby results of the particle size distribution, N_2 -physisorption, FESEM-EDX, XRD and Uv-vis DRS are included to obtain the physicochemical properties. Subsequently, Section 4.3 focuses on the photocatalytic Fenton activity on glycerol as the substrate of interest. Briefly, preliminary works related to the determination of transport resistances, effects of initial catalyst loadings, effects of initial concentration of reactants, mechanism proposition of photocatalytic Fenton, as well as some modelling works are included. Finally, experimental design can be found in Section 4.4 whereby the factorial experimental design is further explained

4.2 FRESH CATALYST CHARACTERIZATION

4.2.1 N_2 -Physisorption

In the BET analysis, data of adsorbed nitrogen in term of volume (V_{ads}) and number of moles (n_{ads}) at different pressures were interpreted using various methods to obtain the analysis results regarding the surface properties of the catalysts.

The isotherm of CuFe_2O_4 is shown in Figure 4.1. The isotherm obtained from plotting the V_{ads} versus P/P^0 provides the information of textural properties of CuFe_2O_4 . The value of the pore volume was taken at $P/P^0 = 0.95$. The two curves in the isotherm plot were the result of the adsorption and desorption of N_2 molecules on the CuFe_2O_4 sample. At low pressure, the N_2 molecules began to fill the pores of the CuFe_2O_4 rapidly and this was manifested by its steep slope with pressure increment at the onset. As the pressure continued to increase, the surface pores were eventually covered by N_2 . The amount of N_2 molecules adsorbed was therefore not so affected by the increase in pressure. This occurred in the middle phase of the isotherm. BET isotherm applies the assumption that all sites on the sample surface are equivalent. However, deviation occurred at high pressures due to the presence of cracks and indents. These surfaces could only hold a few monolayers of nitrogen at lower pressures. High pressure forced the adsorption of nitrogen to form more layers, thus the curve turned steep at the end of the isotherm (cf. Figure 4.1). Moreover, it can be observed that the adsorption and desorption curves have deviated to form hysteresis loop. Generally, adsorption of an equilibrium amount of adsorbate is a reversible process, resulting in a same curve for adsorption and desorption. However, in the case of curved surfaces, such as the mesoporous surface in this case, the amount of N_2 molecules adsorbed upon increasing or decreasing the gas pressure do not coincide over a certain interval of pressures. The capillary condensation is a phenomenon of liquid-gas phase transitions under porous confinement which explains the resulting hysteresis loop. This hysteresis phenomenon showed that the pores on the samples were mesoporous in nature.

For the determination of the surface area of the catalysts, models such as Langmuir method, 2-Parameters Line and 3-Parameters Fit were employed. The graphs for the three methods were plotted as $p/(V_{\text{ads}} P^0)$ versus P/P^0 , $P/(V_{\text{ads}}(P^0-P))$ versus P/P^0 , and V_{ads} versus P/P^0 , respectively. Among the three methods, 2-Parameters Line model showed the highest regression value of 0.9999 (cf. Figure 4.2). Consequently, the estimated BET specific surface area of the synthesized CuFe_2O_4 in the current work was $102.4 \text{ m}^2/\text{g}$. As comparing to the past researcher, there is a slightly difference between the surface area of CuFe_2O_4 whereby the surface area obtained was $122 \text{ m}^2/\text{g}$ (Wang et al., 2014). This could be due to the different preparation method of the photocatalyst.

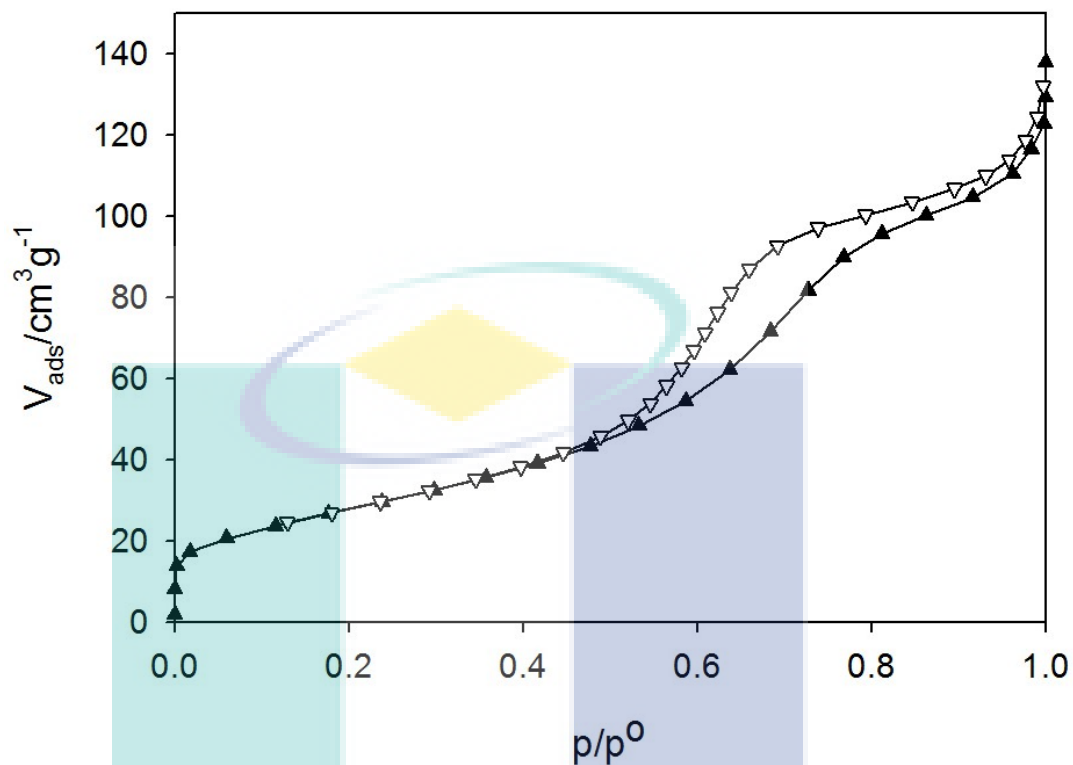


Figure 4.1: Isotherm of CuFe_2O_4 from N_2 Physisorption analysis

The last parameter determined from the N_2 physisorption analysis was the mesopores of the catalyst. The models employed were Barret-Joyner-Halenda (BJH), Cranston and Inkley, Modelless, and Horvath and Kawazoe. All the estimations gave pore diameters that ranged from 100 to 140 nm.

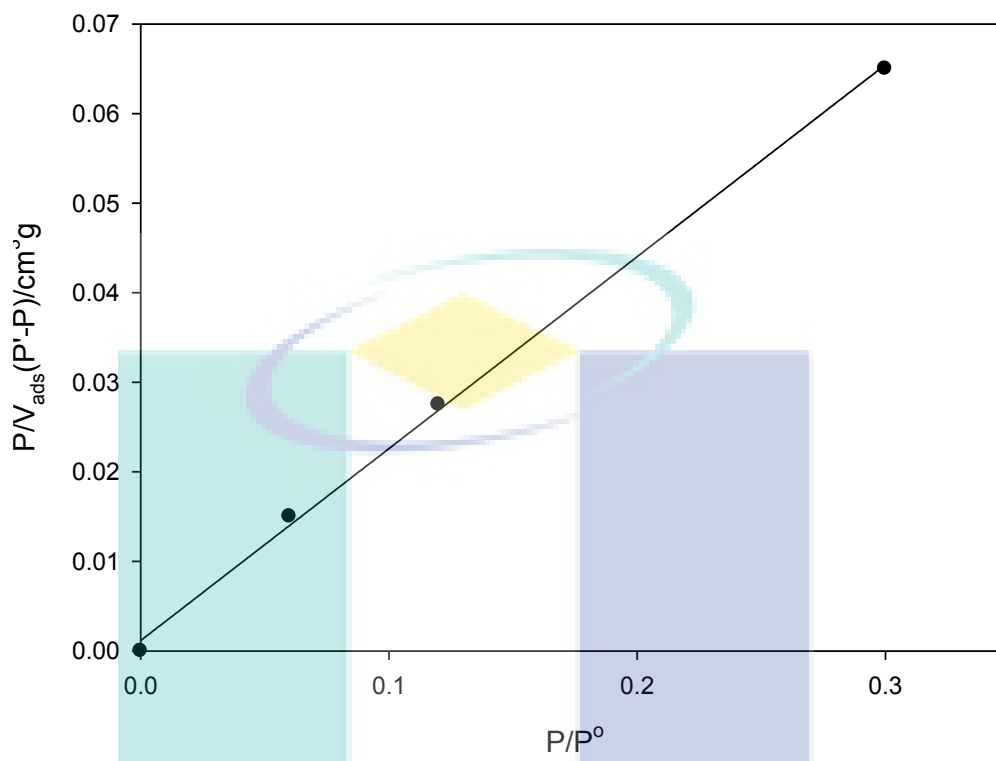
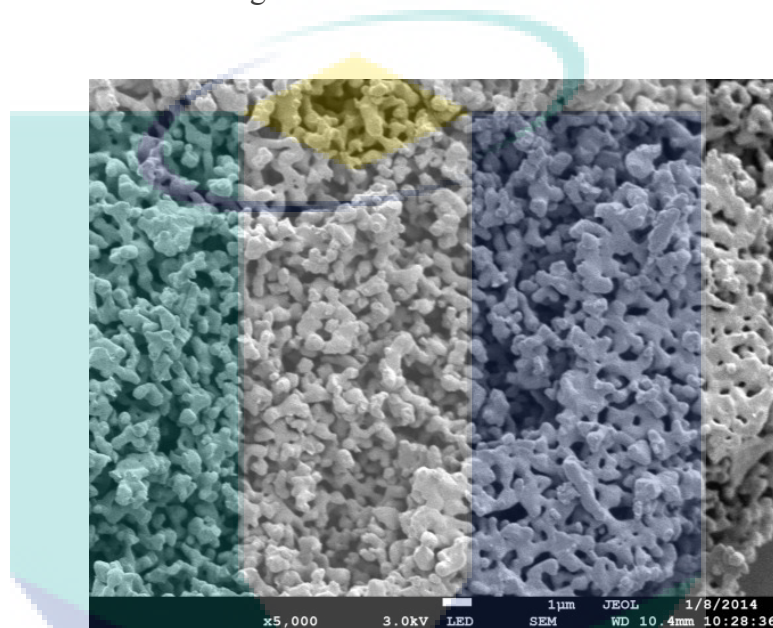


Figure 4.2: Specific surface area determination of CuFe_2O_4 by 2-Parameters Line model

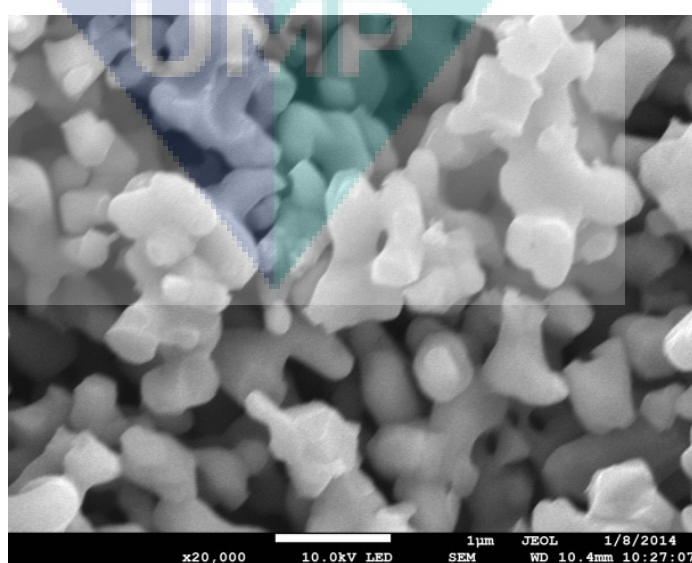
4.2.2 FESEM-EDX Analysis

Most of the past researchers use the technique of SEM to determine the morphology of the samples. As comparing between SEM technique and FESEM technique, FESEM image is more clearly. The FESEM-EDX technique was employed in the current work to examine both the morphology as well as element identifications of fresh CuFe_2O_4 (cf. Figure 4.3). The morphology of the CuFe_2O_4 at different level of magnifications *viz.* $\times 5000$, $\times 20000$ and $\times 50000$, showed solid specimen with irregularly-shaped nanoparticles, albeit with good homogeneity in particle size distribution. Moreover, the particles also appeared fused together, which may be attributed to the high calcination temperature (850°C) employed in this study. Furthermore, it can be observed that the structure was porous with formation of noticeable void volume, consistent with large BET specific surface area

obtained from N₂-physisorption (cf. Section 4.2.1). As comparing to previous study, it also shows solid specimen with irregularly-shaped nanoparticles and the particles appear fused together (Wang et al., 2014). The EDX spectrum taken on the same CuFe₂O₄ photocatalyst showed that the solid was indeed comprised of Cu, Fe and O elements only with 5.50, 64.15 and 26.10 wt%, respectively, unadulterated by any other impurities. The element C detected was attributed to the background.



(a)



(b)

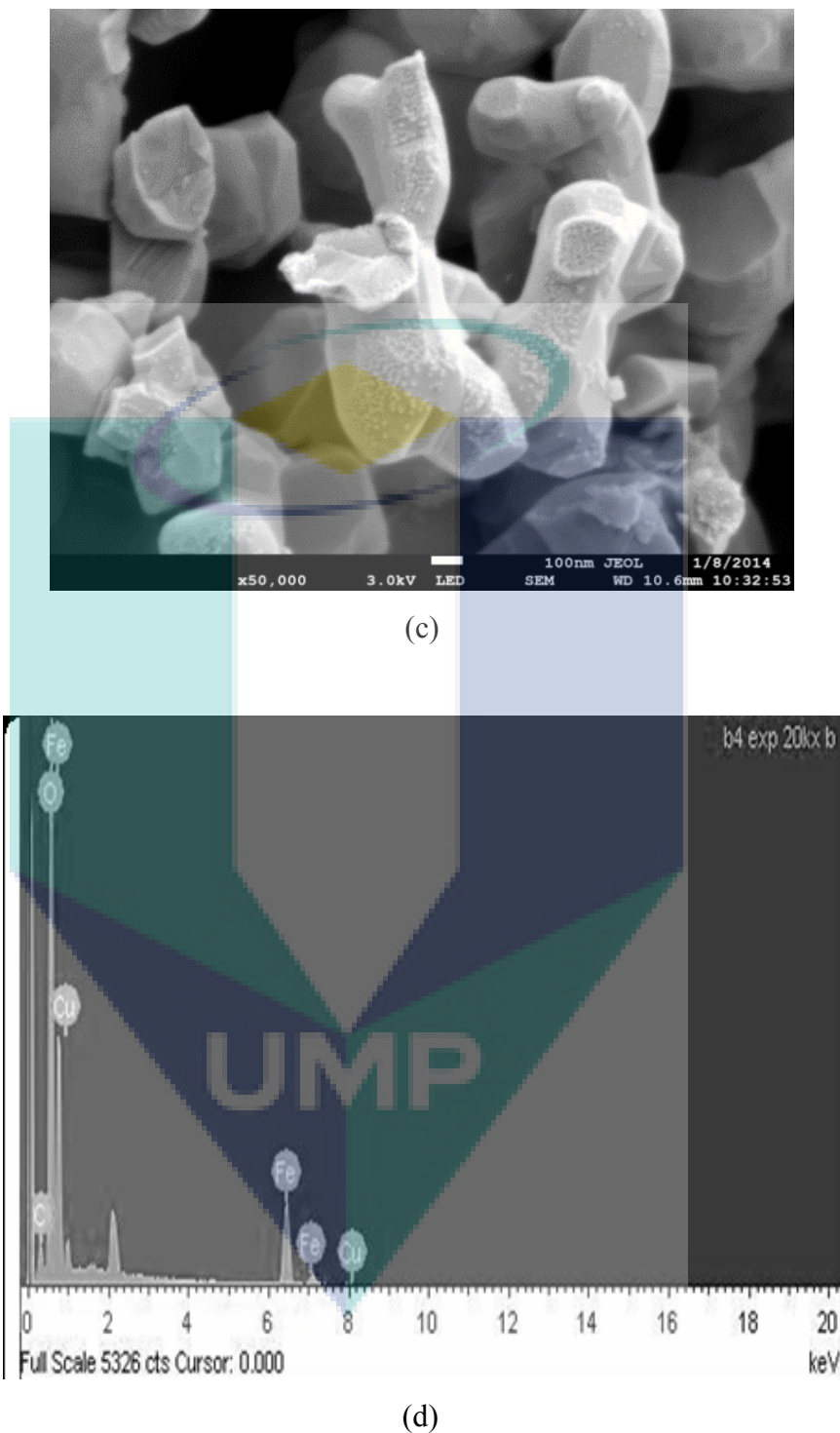


Figure 4.3: (a) to (c) FESEM image of the fresh CuFe_2O_4 at different magnification levels;
(d) EDX image of the fresh CuFe_2O_4 photocatalyst

4.2.3 XRD Analysis

X-ray diffraction (XRD) was used to determine the crystal phase structure of the photocatalyst. Figure 4.4 shows the XRD patterns of the CuFe_2O_4 photocatalyst. The sharp diffracted peaks were an indication of well-defined crystallite structure. Significantly, a new visible light-active compound known as the CuFe_2O_4 crystal was detected. Therefore, it can be surmised that the catalyst formulation and synthesis strategy has successfully produced the desired solid phase. This result was also consistent with the EDX analysis in Section 4.2.2. CuFe_2O_4 is a member of the magnetite series of spinel with 2θ of 18.56° , 30.08° , 34.82° , 36.03° , 37.27° , 54.23° and 62.25° . It takes the form of cubic with lattice parameters $a=5.82 \text{ \AA}$, $b=5.82 \text{ \AA}$ and $c=8.62 \text{ \AA}$. The average crystallite size which was calculated using the Scherrer equation (cf. Eq. (3.2)) showed that the crystallite size of CuFe_2O_4 was 53 nm. Traces of Fe_2O_3 and CuO are also visible, recorded at 2θ of 32.0° and 39.0° , respectively. Researchers have indicate that the CuFe_2O_4 is tetragonal shape (JCPDS 34-0425) with (101), (112), (103), (211), (202) and (224) crystallographic planes (Wang et al., 2014; Yang et al., 2009).

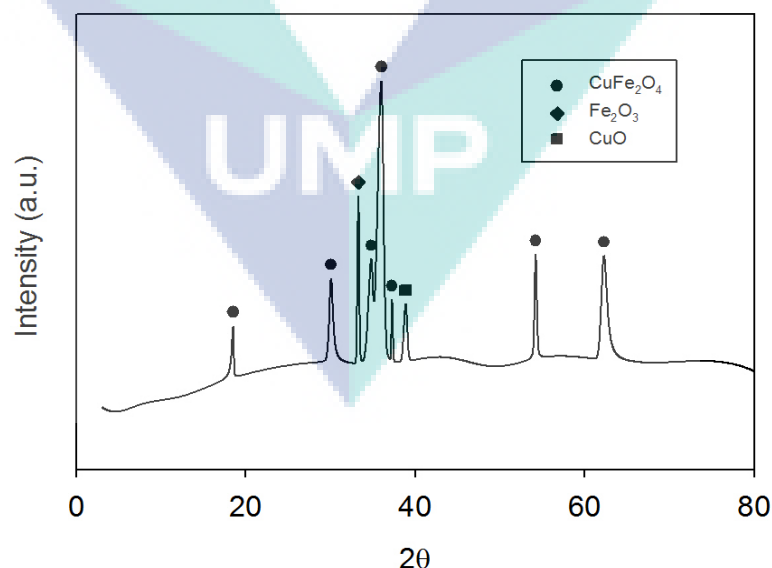


Figure 4.4: XRD pattern of CuFe_2O_4 solid sample

4.2.4 Optical Properties

Figure 4.5 shows the UV-Vis DRS spectrum of CuFe_2O_4 . From the Figure 4.5, it can be estimated that the minimum wavelength required for the prepared CuFe_2O_4 photocatalyst to be active was 785 nm or in other words, the CuFe_2O_4 was active under visible light irradiation of wavelength up to 785 nm. The energy required by photon to generate electron-hole pair in a photocatalyst can be related to its wavelength (Wade, 2005) by the equation $E_{bg} = \frac{1240}{\lambda}$, where λ = wavelength of photon in nm and E_{bg} = band gap of semiconductor in eV. The band gap of the as-synthesized CuFe_2O_4 was obtained by plotting data from UV-vis DRS (cf. Figure 4.5). The band gap was found to be 1.58 eV. The band gap energy magnitude showed that the prepared CuFe_2O_4 has a larger band gap than the one reported by Derbal et al. (2008) with a band gap of 1.32 eV. This could be due to the presence of some CuO (1.6 eV) (Kumar et al., 2013) and Fe_2O_3 (2.2 eV) (Blake, 2001) impurity phase as evinced in the XRD diffractogram (cf. Figure 4.4).

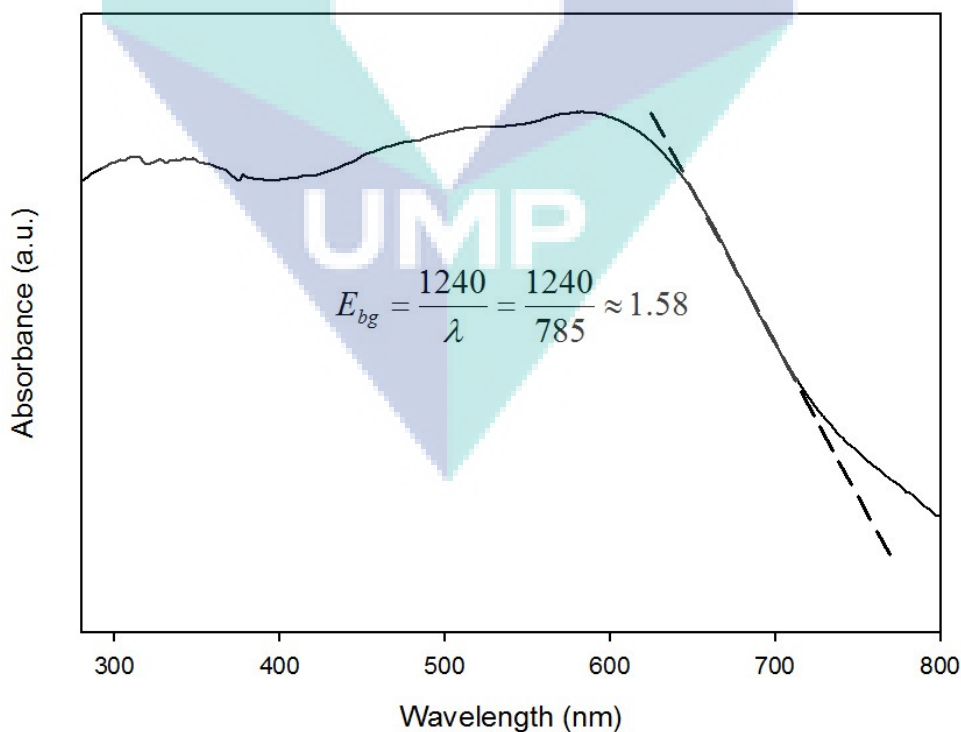


Figure 4.5: Graph of absorbance versus wavelength for as-synthesized CuFe_2O_4

4.2.5 Particle Size Distribution

The particle size of CuFe_2O_4 photocatalyst was also determined using Malvern Mastersizer 2000 models and results obtained is shown in Figure 4.6. It can be observed that the distribution of particle size takes the form of Gaussian shape and exhibits monodispersity. Furthermore, it can be concluded that the average size of the as-synthesized CuFe_2O_4 photocatalyst was *circa* 100 μm . This average particle size was employed in the subsequent preliminary works of photocatalytic Fenton activity of glycerol degradation, to determine the region that was free from mass transport intrusion.

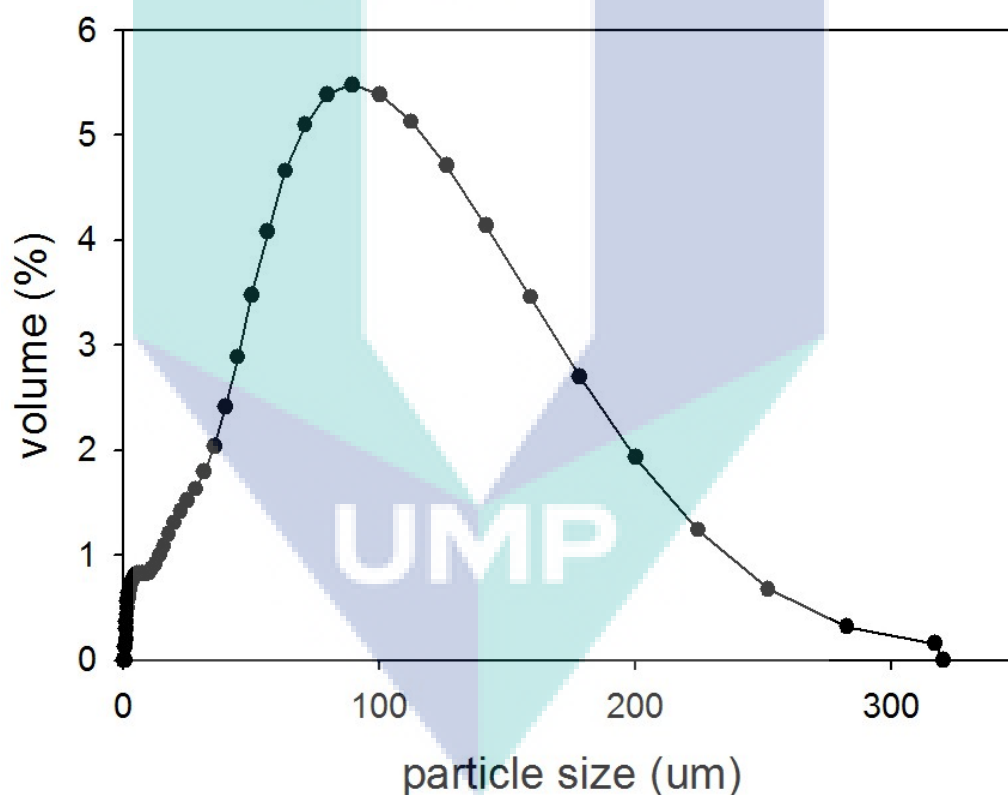


Figure 4.6: Monodispersity of particle size distribution of the CuFe_2O_4

4.3 PHOTOCATALYTIC FENTON ACTIVITY EVALUATION

4.3.1 Transport Resistance Considerations

There are several sequential steps occur during heterogeneous catalytic reactions. It is identified as following:

1. Mass transfer (diffusion) of the reactants from the bulk fluid to the external surface of the catalyst.
2. Transport of reactants by the diffusion process through the pores into the inner particle to reach active catalyst sites.
3. Chemical adsorption of reactants on the internal catalyst surface.
4. Chemical reaction between the chemisorbed reactants to produce products.
5. Desorption of products from the catalyst surface.
6. Diffusion of products through the pores of the particle.
7. Transport of products from the external surface of the particle to the bulk fluid, thus completing the overall catalytic chemical reaction.

Out of the seven steps listed, only steps 3, 4 and 5 are the true representation of chemical reaction. The reacting system must be operated far away from the influence of physical transport limitations as these limitations may mask the kinetic data obtained. Established criteria were engaged to ensure that the current system was free from any transport limitations. The calculation presented in the following section employed reaction conditions carried out at highest concentration of glycerol (68.41 mM glycerol, CuFe_2O_4 loading of 0.1 g/L). Under these conditions, reaction rate for glycerol photocatalytic Fenton degradation was the highest, at $2.30 \times 10^{-5} \text{ kg-mol kg}_{\text{cat}}^{-1} \text{ s}^{-1}$ ($0.1380 \text{ mM min}^{-1}$).

Table 4.1 comprises of significant thermodynamic and kinetic data of the reaction system which was applied in the current work of glycerol photocatalytic Fenton process. Further details are given in Appendix G.

4.3.1.1 External Mass Transfer

External mass transfer occurs due to film layer between the bulk fluid phase and the outer catalyst surface. The criterion developed by Hudgins in 1972 (Hudgins, 1972) is amongst the most commonly employed, and therefore, was the one applied in this study. According to Hudgins, the reaction system is free of external mass transport intrusions if:

$$\frac{r_{\text{exp}} \rho_b d_p r^n(C_A)}{k_c r(C_A)} < 0.3 \quad (4.1a)$$

which can be simplified to (for an n^{th} -order reaction):

$$\frac{r_{\text{exp}} \rho_b d_p |n|}{k_c C_A} < 0.3 \quad (4.1b)$$

where

r_{exp} = experimental reaction rate ($2.30 \times 10^{-5} \text{ kmol} \cdot \text{kg}_{\text{cat}}^{-1} \text{ s}^{-1}$)

ρ_b = bulk density of catalyst (0.1 kg m^{-3})

d_p = average catalyst particle diameter ($1.0 \times 10^{-4} \text{ m}$)

n = reaction rate order

k_c = mass transfer coefficient ($9.88 \times 10^{-4} \text{ m s}^{-1}$)

C_A = concentration of reactant A ($68.41 \times 10^{-3} \text{ kmol m}^{-3}$)

It is well-known that n in general, rarely exceeds three in most reactions. Substituting physical properties of the catalyst and the reaction system into Eq. (4.1b) yielded the term on the left-hand side (LHS) as 1.02×10^{-5} at $n = 3$ which is still very much less than 0.3 (the term on the right-hand side). This confirmed that external mass transfer resistance was practically absent under the experimental conditions.

4.3.1.2 Pore (Intra-particle) Diffusion Limitation

The occurrence of internal diffusion is negligible if (Hudgins, 1972):

$$\frac{r_{\text{exp}} R_p^2 \rho_b r'(C_A)}{3D_{\text{eff}} r(C_A)} < 1 \quad (4.2a)$$

which can be simplified to (for an n^{th} -order reaction):

$$\frac{r_{\text{exp}} R_p^2 \rho_b |n|}{3D_{\text{eff}} C_A} < 1 \quad (4.2b)$$

where

r_{exp} = experimental reaction rate ($2.30 \times 10^{-5} \text{ kmol} \cdot \text{kg}_{\text{cat}}^{-1} \text{ s}^{-1}$)

ρ_b = bed density (0.1 kg m^{-3})

R_p = average catalyst particle radius ($5.0 \times 10^{-5} \text{ m}$)

n = reaction rate order ($n=3$)

C_A = concentration of reactant A ($68.41 \times 10^{-3} \text{ kmol m}^{-3}$)

D_{eff} = effective diffusivity coefficient ($5.48 \times 10^{-10} \text{ m}^2 \text{ s}^{-1}$)

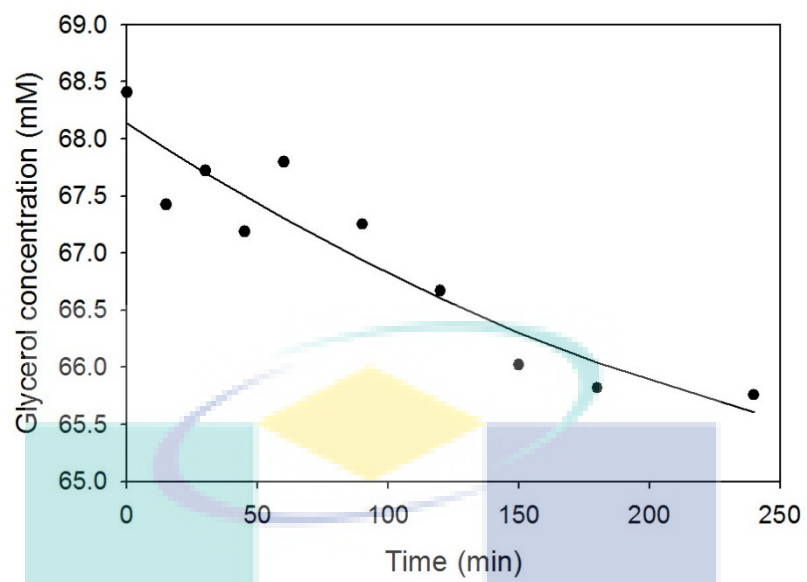
Consequently, substitution of the relevant values gave LHS products as $1.54 \times 10^{-3} \ll 1$ indicating that pore diffusion resistance was negligible.

Table 4.1: Summary of parameters used in mass and heat transport criteria

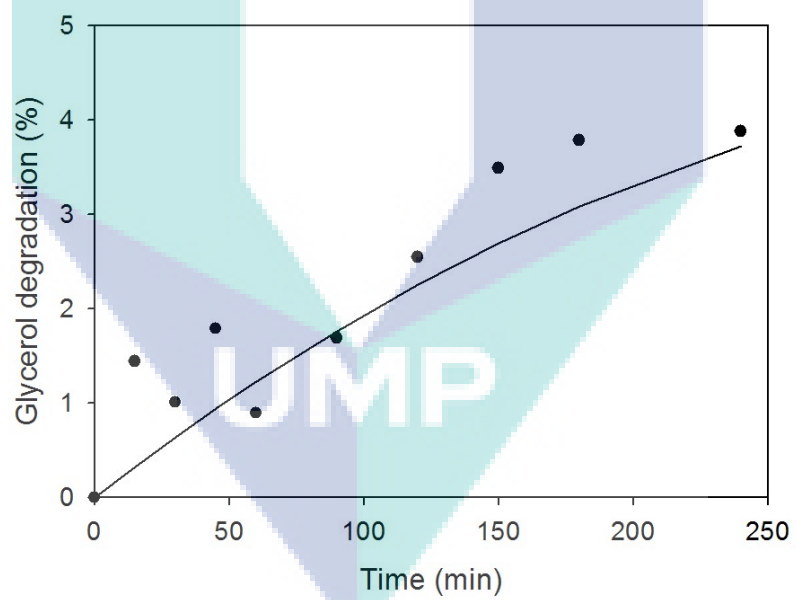
Parameter	Value	Source
ρ_c	5240 kg m ⁻³	Perry and Green
ρ_b	0.1 kg m ⁻³	Experimental condition
ρ_w	999.97 kg m ⁻³	Experimental condition
d_p	1.0×10 ⁻⁴ m	Experimental condition
μ	8.9×10 ⁻⁴ Pa s ⁻¹	Perry and Green
T	298 K	Experimental condition
D_{AB}	1.095×10 ⁻⁹ m ² s ⁻¹	Estimation for C ₃ H ₈ O ₃ –H ₂ O
D_{eff}	5.47×10 ⁻¹⁰ m ² s ⁻¹	0.5× D_{AB}
k_c	9.88×10 ⁻⁴ m s ⁻¹	Theoretical computation
U	2.75 m s ⁻¹	Experimental condition
C_A	68.41 mol m ⁻³	Theoretical computation
ε	0.999	Experimental condition
n	3	Assumption

4.3.2 Adsorption Study

Adsorption study was carried out to determine both the glycerol and H₂O₂ uptakes by the CuFe₂O₄ at room temperature. In the current study, the adsorption run was carried out at a loading of 0.1 g/L CuFe₂O₄ photocatalyst and reactant concentrations that were comprised of 68.41 mM glycerol and 819.5 mM of H₂O₂. It can be observed from Figure 4.7 that without light irradiation, the glycerol concentration only dropped slightly over the course of 4 h, which corresponds to less than 4.0% adsorption (refers to Figure 4.7(b)). Similar trend was also exhibited by the transient H₂O₂ concentration profiles as shown in Figure 4.87(d) which clearly demonstrate an average adsorption of 2.0% compared to its initial concentration level. In the absence of light source, chemical reaction rate was slow and practically may be negligible. Consequently, this has demonstrated that light source was a primary driving force in activating the current reaction.



(a)



(b)

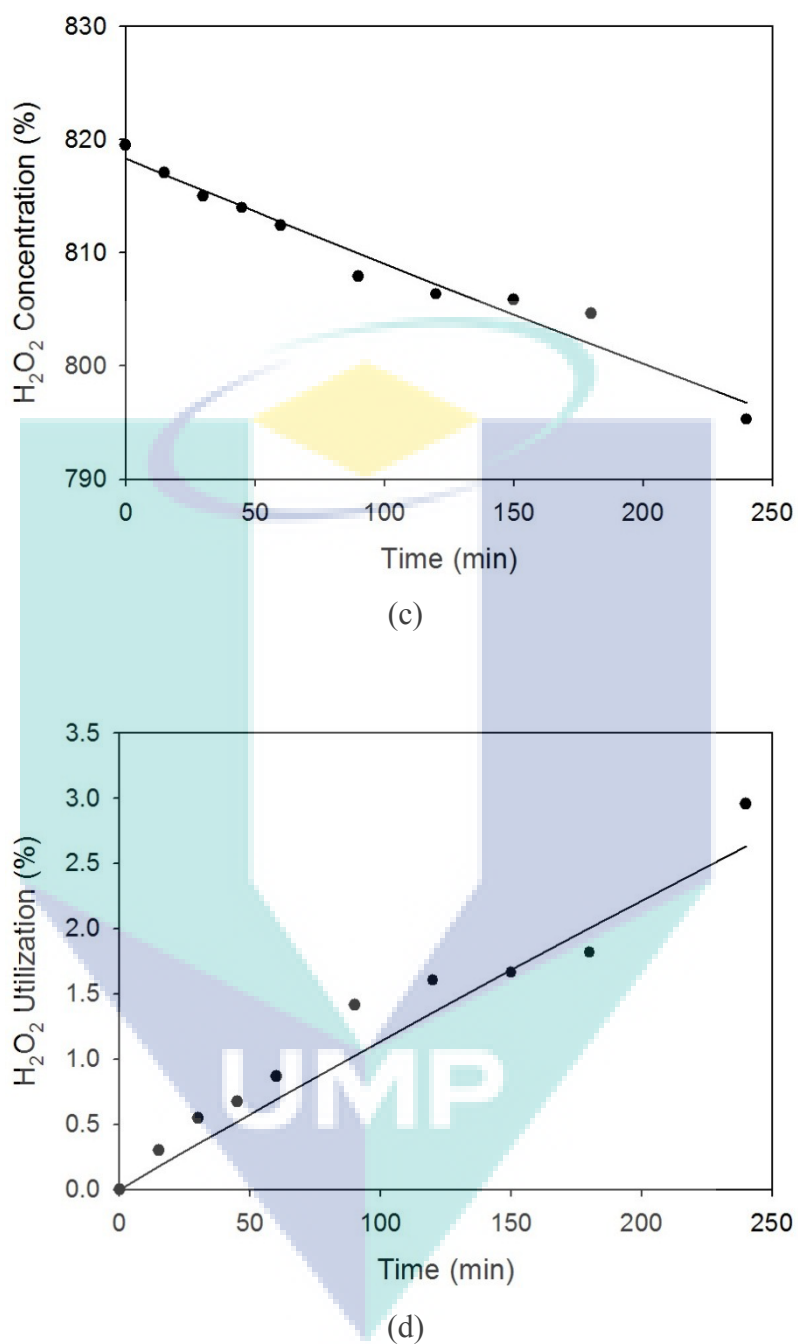


Figure 4.7: Transient profiles of (a) C₃H₈O₃ concentration, (b) C₃H₈O₃ adsorption (%), (c) H₂O₂ concentration and (d) H₂O₂ adsorption (%) at 0.1 g/L CuFe₂O₄ photocatalyst, 68.41 mM glycerol and 819.5 mM H₂O₂ under dark environment

4.3.3 Effects of Initial Catalyst Loading

Experiments for determination of the effect of initial catalyst loading were carried out at 68.4 mM of glycerol and 819.5 mM of H₂O₂. The lower boundary limit of catalyst loadings was set at 0.1 g/L, as loading below this threshold was practically difficult to handle. All the experiment runs were under 250 W of visible light irradiation. Experiments were running for four hours because there is no much degradation of glycerol after four hours.

Figure 4.8 and Figure 4.9 show the transient concentration profiles of glycerol and H₂O₂ and their transient conversion, respectively. The concentration profiles of both glycerol and H₂O₂ (refers to Figure 4.8(a) and Figure 4.9(a)) showed a significant downward trend, symptomatic of progressive chemical reaction. The blank run (without catalyst) indicates that photolysis reaction occurred and achieved glycerol degradation of 17.7% (cf. Figure 4.8) and H₂O₂ utilization of 8.0% (cf. Figure 4.9) after 4 h of reaction. In the presence of CuFe₂O₄ photocatalyst, the onset of photocatalytic Fenton reaction has increased substantially the degradation of glycerol, i.e. at 0.1 g/L of photocatalyst loading, the degradation of glycerol can attain 27.0% and peaked at almost 40.0% of glycerol degradation when 5.0 g/L of CuFe₂O₄ photocatalyst loading was employed. By increasing the photocatalyst loadings from 0.1 to 5.0 g/L, the number of active sites would have increased in tandem, consequently, the glycerol degradation also increased. Indeed, as can be seen in Figure 4.8(b), the glycerol degradation percentage has incrementally increased with catalyst loading. This was exhibited by 38.0% (5.0 g/L) > 36.0% (2.0 g/L) > 30.0% (1.0 g/L) > 27.0% (0.1 g/L).

As aforementioned, H₂O₂ concentration as in Figure 4.9 also dropped with reaction time, in tandem with the trend exhibited by the glycerol concentration. The highest H₂O₂ consumption was recorded for the 5.0 g/L (35.0%) whilst it was 22.0% for the CuFe₂O₄ loading of 0.1 g/L, which was an impressive result, considering that it only involved a small amount of catalyst.

Although the results from the variations in initial photocatalyst loading showed that 5.0 g/L consistently yielded highest utilization of both reactants, a minimum 0.1 g/L of CuFe_2O_4 photocatalyst also gave significant consumption, hence was chosen as the preferred loading for the subsequent investigation.

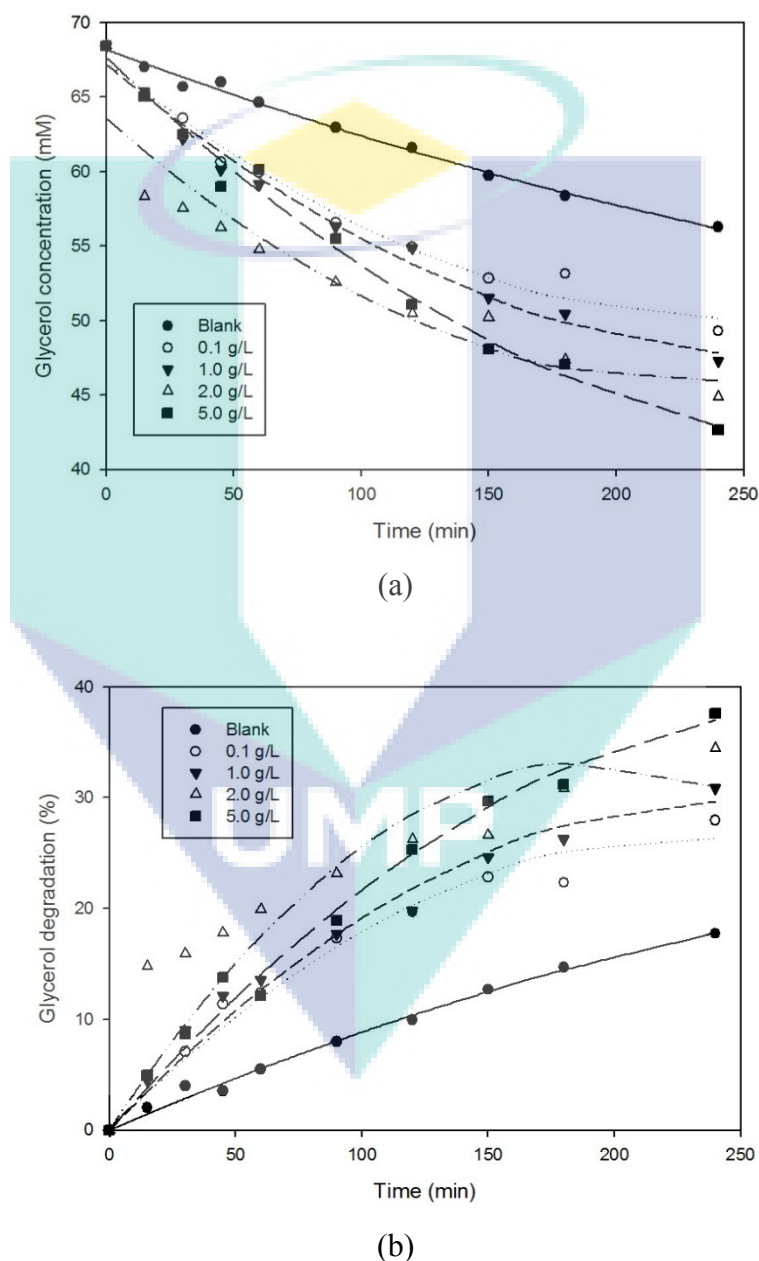


Figure 4.8: Transient profiles of (a) glycerol concentration and (b) glycerol degradation (%) at different photocatalyst loadings

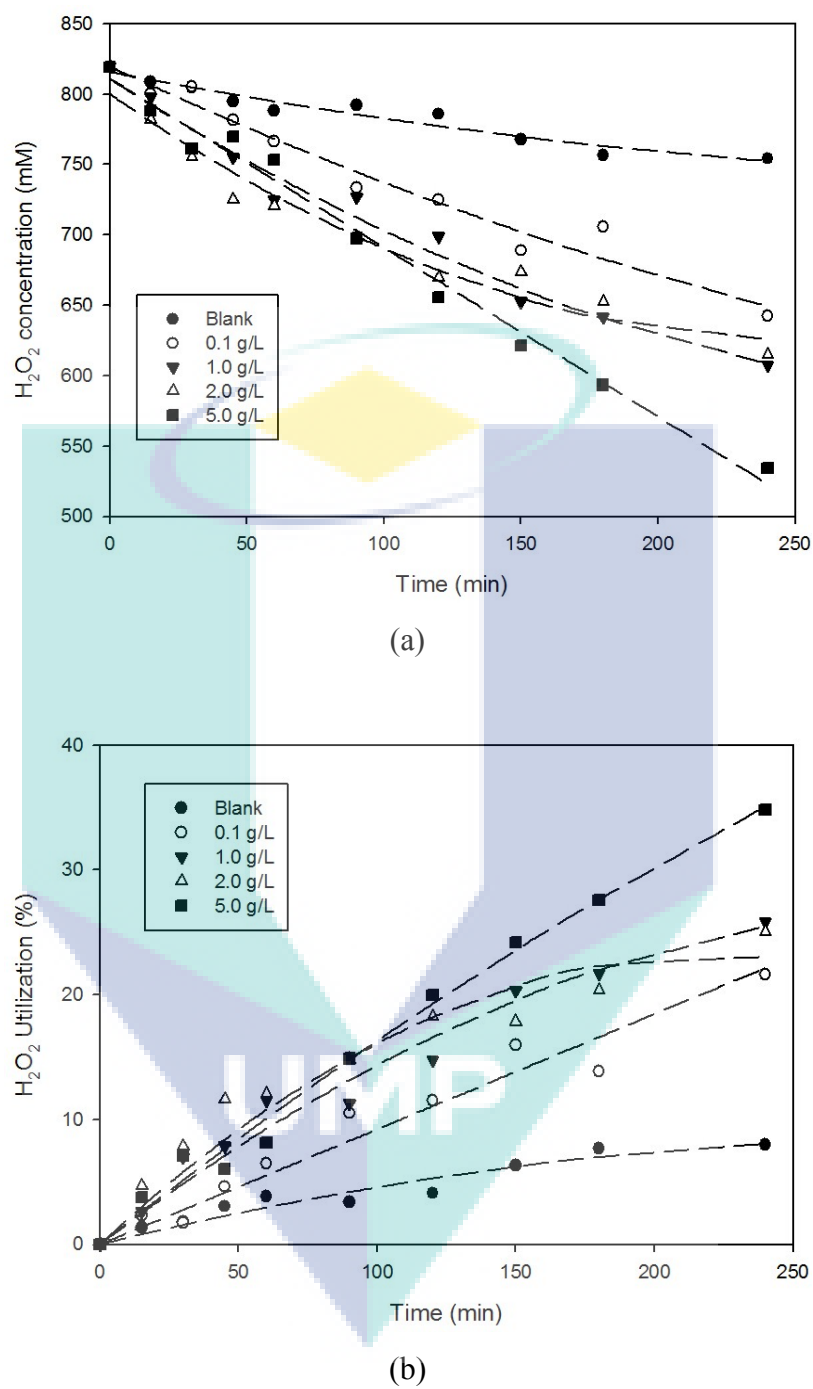


Figure 4.9: (a) H₂O₂ concentration (b) H₂O₂ utilization versus time at different photocatalyst loadings

The results shown in Figure 4.8 demonstrated that the photocatalytic degradation rate has a non-linear dependency on catalyst loading with maximum at 5.0 g/L. In fact, at high catalyst loadings (2.0 and 5.0 g/L), the effective light intensity has obviously diminished because of the increased solution opacity. The data in Figure 4.8 was further regressed and differentiated using Polymath software[®] to obtain the glycerol decomposition rate, $\left(-\frac{dC_{glycerol}}{dt}\right)$. As the reaction duration was relatively short (240 min) and the reaction may be accompanied by some deactivation of catalyst, the method of initial reaction rate was employed (Folger, 2008). It was found that the reaction rate may be presented by an empirical equation, written:

$$\left(-r_{glycerol}\right) = \left(-\frac{dC_{glycerol}}{dt}\right) = \frac{kW_{catalyst}}{(\alpha + W_{catalyst})} \quad (4.3)$$

where

$W_{catalyst}$ = the catalyst weight per unit volume of solution (g L^{-1})

k = pseudo-rate constant for the catalyst loading (mM min^{-1})

α = parameter that indicates volumetric light shielding effect (g L^{-1})

Figure 4.10 shows glycerol photocatalytic Fenton degradation rate at different photocatalyst loadings with a correlation coefficient R^2 of 0.99. The denominator in the Langmuir-Hinshelwood type of equation indicates the particle-particle interaction.

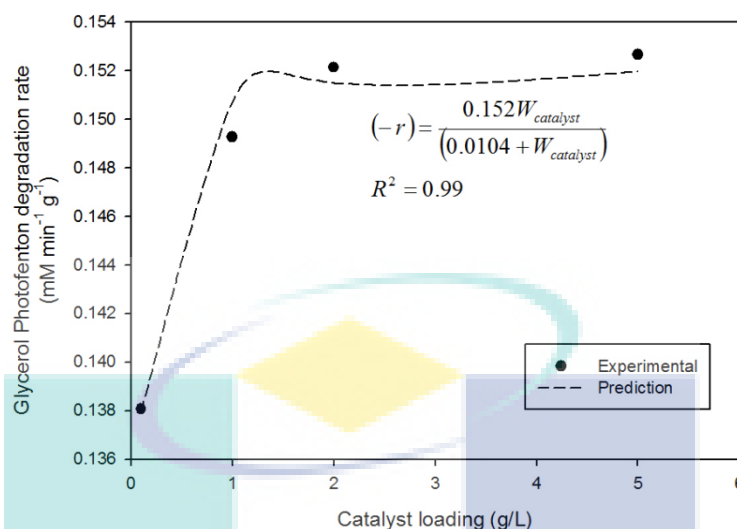


Figure 4.10: Glycerol photocatalytic Fenton degradation rate at different photocatalyst

4.3.4 Effects of Initial Concentration of Glycerol

The investigation of reactant concentration on the kinetics of photocatalytic Fenton degradation of glycerol was carried out to examine the glycerol conversion. In order to study the effect of initial glycerol concentration on glycerol decomposition, the initial concentration was varied from 27.36 mM to 68.41 mM in the presence of 0.1 g/L of CuFe_2O_4 and 819.5 mM H_2O_2 . As aforementioned, loading of 0.1 g/L was chosen instead of the other catalyst loadings as this minimum loading was able to yield significant reaction rate.

As shown in Figure 4.11(a), all the transient concentration profiles exhibit non-linear downward trend. However, by increasing the initial glycerol concentration, the glycerol degradation has decreased (refers to Figure 4.11(b)). Indeed, at 27.36 mM initial glycerol concentration, degradation rate was nearly 60.0%. In contrast, when the initial glycerol concentration was 68.41 mM, the degradation has dropped to attain about 30.0% only. The concentration profiles of H_2O_2 that correspond to the Figure 4.11 is presented in Figure 4.12 and exhibit similar downward trend indicating that photocatalytic Fenton

reaction of glycerol has indeed occurred (simultaneous consumption of both glycerol and H_2O_2). This serves to confirm that H_2O_2 indeed directly partake in the reaction.

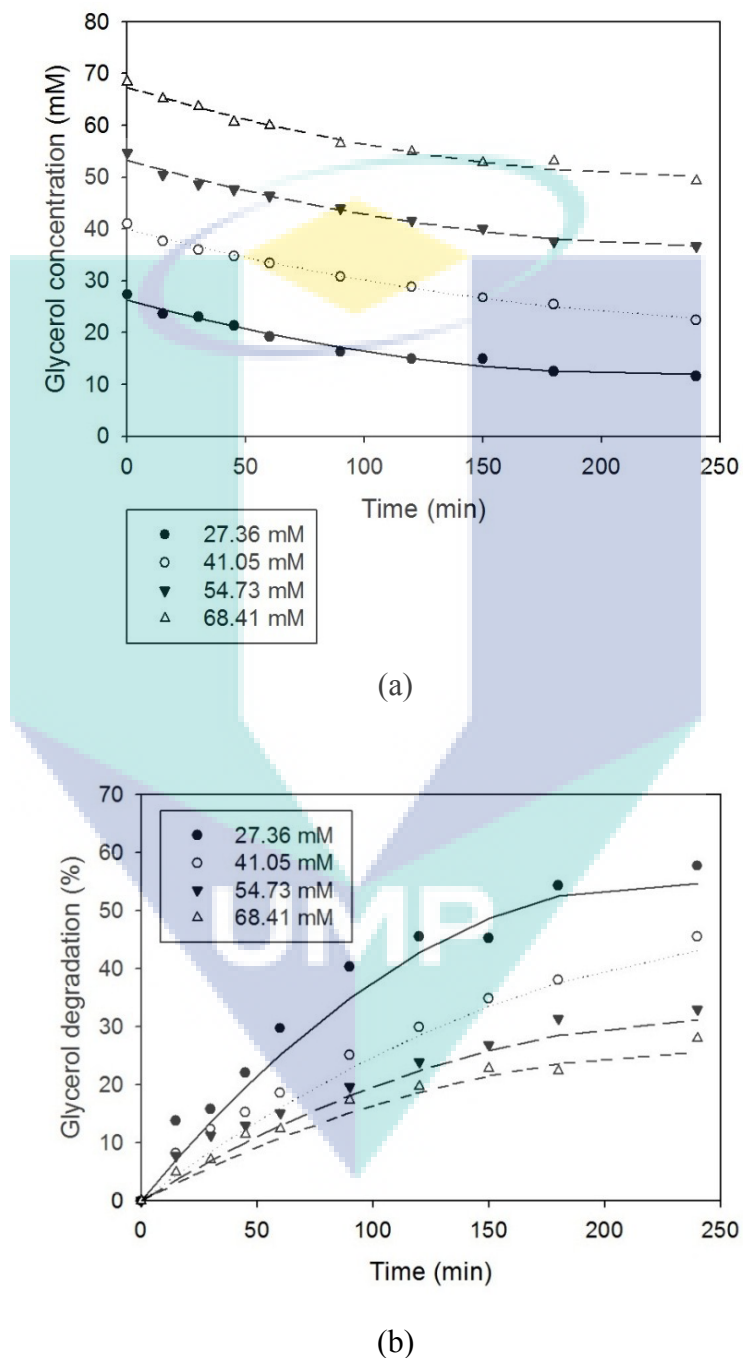
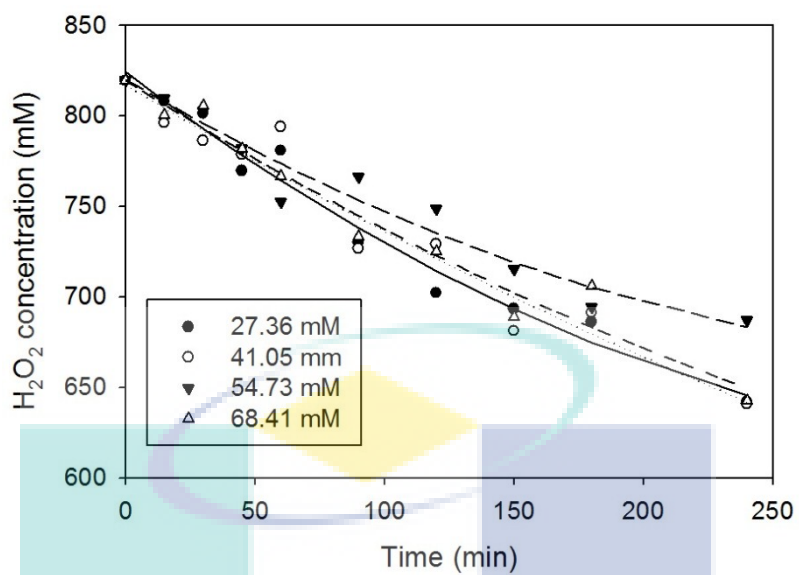
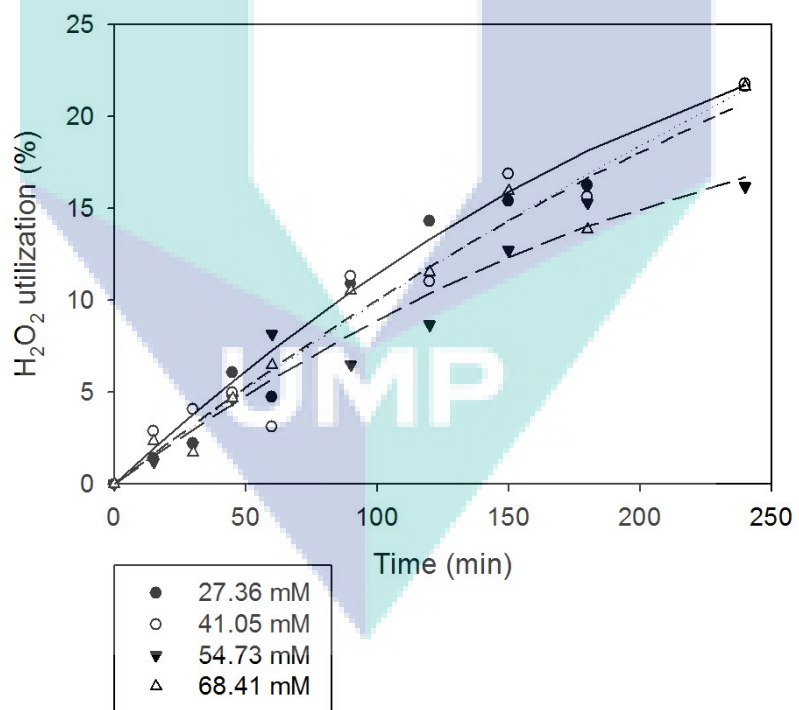


Figure 4.11: Transient profiles of (a) glycerol concentration and (b) glycerol degradation (%) at different initial glycerol concentrations



(a)

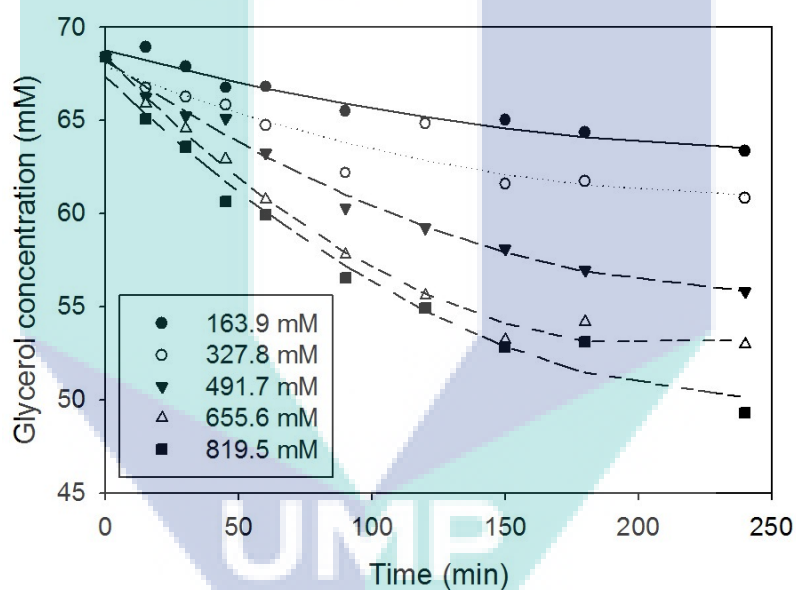


(b)

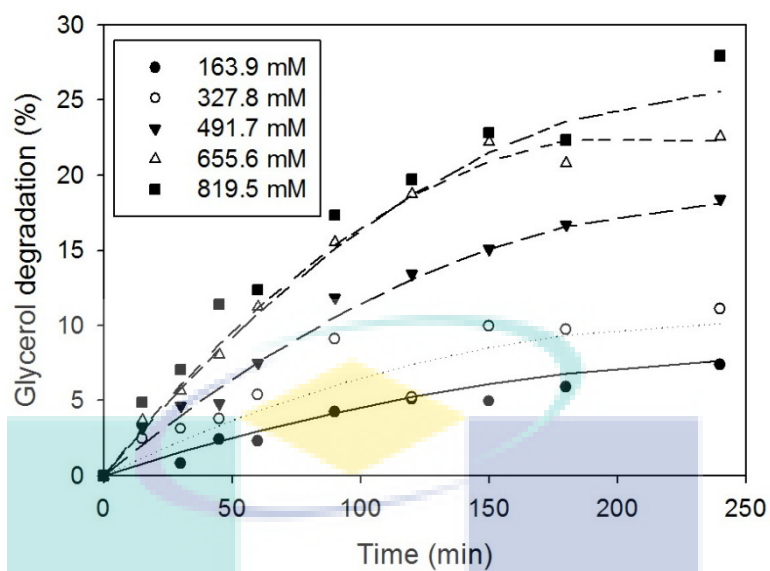
Figure 4.12: Transient profiles of (a) H_2O_2 concentration and (b) H_2O_2 utilization at different initial glycerol concentration

4.3.5 Effects of Initial H₂O₂ Concentration

Initial H₂O₂ concentration will also affect glycerol decomposition. Effect of H₂O₂ from 163.9 mM to 819.5 mM has been studied at constant 68.4 mM glycerol concentration and at loading of 0.1 g/L CuFe₂O₄ as shown in Figure 4.13 and Figure 4.14. Increasing H₂O₂ concentration will produce more •OH radical and then increase the degradation rate of glycerol. At 163.9 mM initial H₂O₂ concentration, the degradation rate is 5%. As increasing the initial H₂O₂ concentration from 163.9 mM to 819.5 mM, the degradation rate is also increasing from 5.0% to 25.0%.

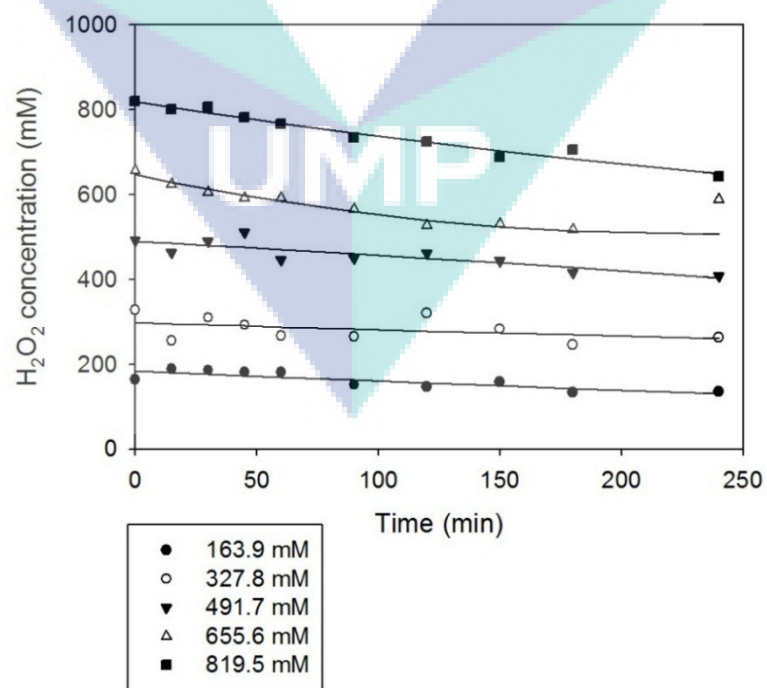


(a)



(b)

Figure 4.13: (a) Glycerol concentration (b) glycerol degradation versus time at different initial H_2O_2 concentration



(a)

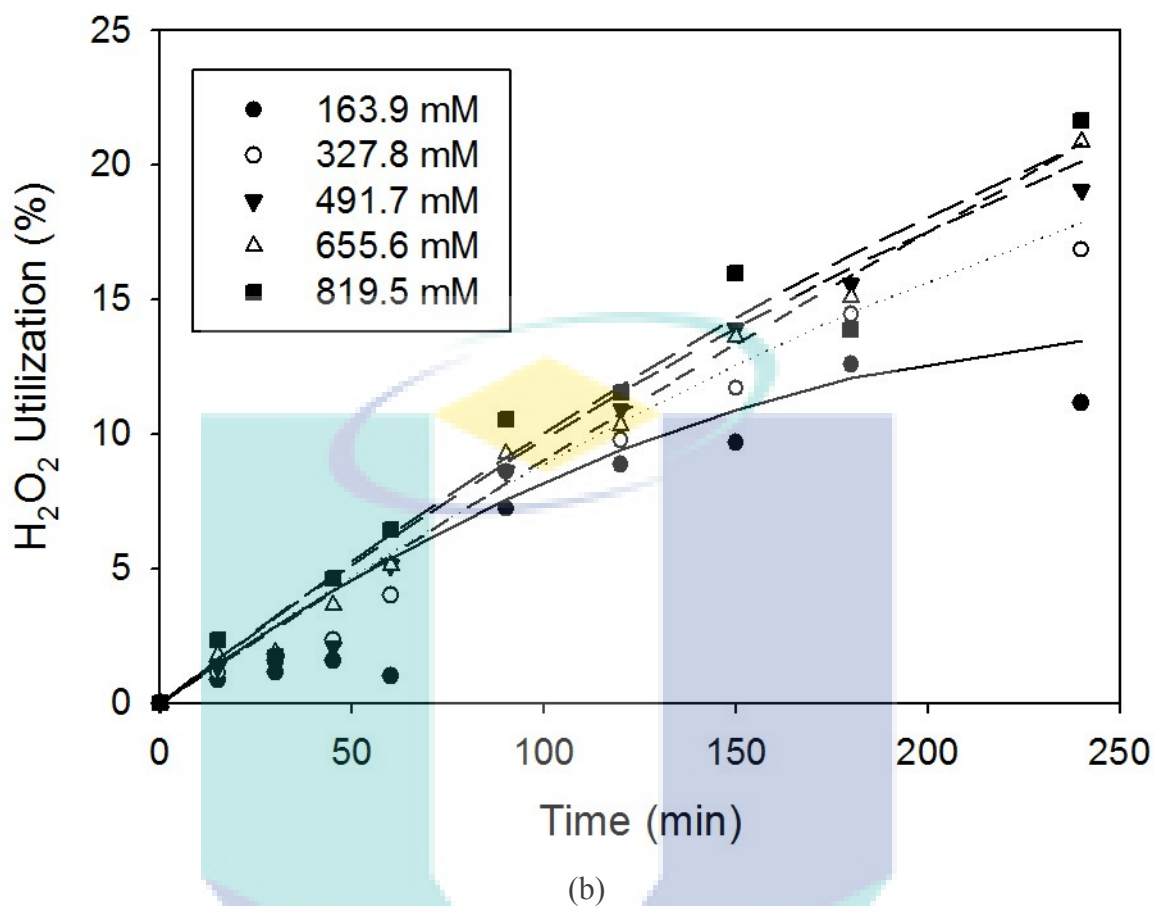


Figure 4.14: (a) H_2O_2 concentration (b) H_2O_2 utilization versus time at different initial H_2O_2 concentration

4.3.6 Power Law Modelling

The results obtained from the variation of initial reactant concentrations demonstrated that the concentrations of both $\text{C}_3\text{H}_8\text{O}_3$ and H_2O_2 affect the rate of photocatalytic Fenton degradation of glycerol. When the transient concentration data were subjected to non-linear regression, then finite differentiation of the resulting regression results, the initial rate of glycerol decomposition was obtained by setting reaction time, $t = 0$ min. The values are summarized in Table 4.2.

Table 4.2: Summary of initial rate of glycerol degradation computed from the differentiation of transient concentration profiles of glycerol

C_{glycerol} (mM)	$C_{\text{H}_2\text{O}_2}$ (mM)	$-r_{\text{glycerol}}^o$ (mM min ⁻¹)
0	0	0
68.4	163.9	0.0380989
68.4	327.8	0.0551275
68.4	491.7	0.0971941
68.4	655.6	0.1487462
68.4	819.5	0.1380215
27.35	819.5	0.1278486
41.05	819.5	0.11808
54.73	819.5	0.13011

Accordingly, the initial rate of photocatalytic Fenton degradation of glycerol can be described by Power Law model which takes the form of:

$$(-r_{\text{glycerol}}^o) = k_{\text{app}} C_{\text{glycerol}}^{\alpha} C_{\text{H}_2\text{O}_2}^{\beta} \quad (4.4)$$

where

$(-r_{\text{glycerol}}^o)$ = initial rate of glycerol photocatalytic Fenton degradation (mM/min)

k_{app} = apparent specific reaction rate

C_{glycerol} and $C_{\text{H}_2\text{O}_2}$ = reactants' initial concentration (mM)

α and β = the orders of reaction

A non-linear regression of the initial rate data collected over different reactant concentrations, was performed using Polymath software in-built with Levenberg-Marquardt optimization method. The resulting parameter estimates are provided in Table 4.3 with reasonably excellent adherence to the Power Law Model judging by the regression

coefficient R^2 of 0.94. Significantly, the order of reactions were fractional, typical characteristic of chemical reaction system, with order of reactions associated with H_2O_2 (0.80) was 4-folds higher than the order of reaction with respect to glycerol (0.20). This confirmed that H_2O_2 was playing a major role in degrading glycerol. The adequacy of power law model may be seen from the parity plot in Figure 4.15. It shows a reasonably good agreement between predicted and observed specific rates.

Table 4.3: Values of kinetic parameters from power law equation

Variable	Value	95% Confidence	R^2
k_{app}	2.78×10^{-4}	6.78×10^{-5}	
α	0.198734	0.060	0.94
β	0.805445	0.037	

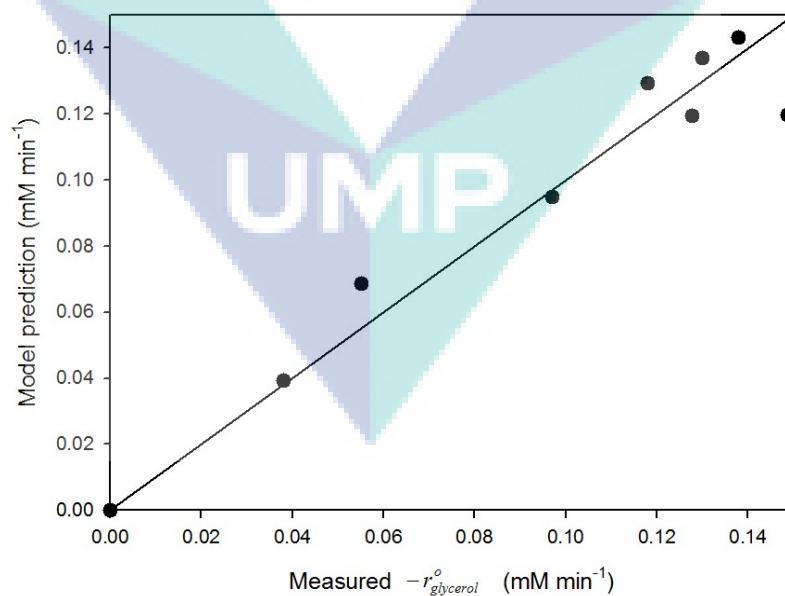


Figure 4.15: Parity plot showing the adequacy of power law modelling

Additionally, as the residual plot depicted in Figure 4.16 evinces no obvious pattern; hence it can be safely assumed that the Power Law model is sufficient to capture the degradation trend.

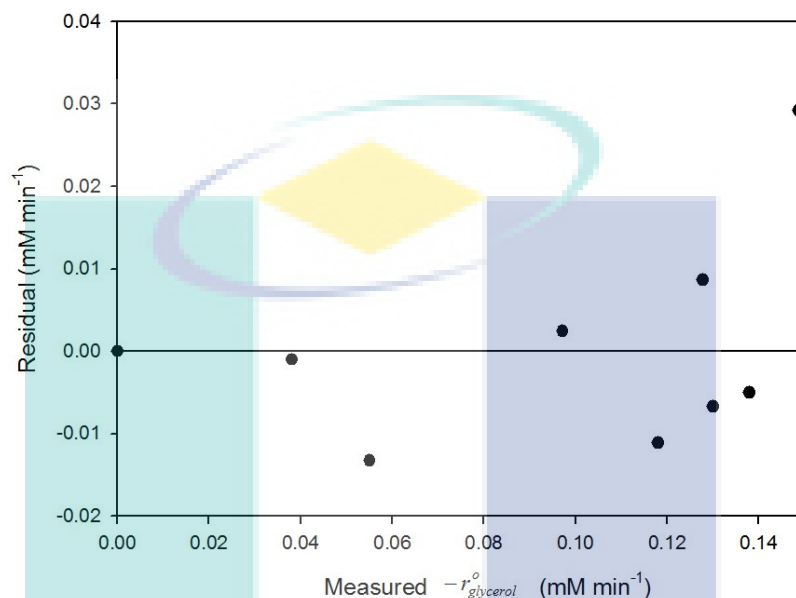


Figure 4.16: Residual plot showing random distribution of error

4.3.7 Mechanisms of Photocatalytic Fenton Degradation of Glycerol

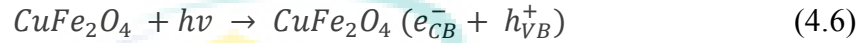
From the trends observed in Figure 4.13 to Figure 4.14, the mechanism of photocatalysis Fenton degradation of glycerol is proposed as follows:

One of the chemical pathways to produce $\bullet\text{OH}$ radicals is as shown in Eq. (4.5):

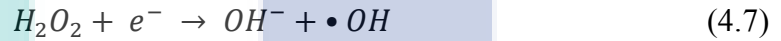


The step in Eq. (4.5) to generate hydroxyl radical would likely occur in the homogeneous phase. Indeed, as shown in all the blank runs (without the presence of CuFe_2O_4 photocatalyst), reaction in Eq. (4.5) indeed has occurred upon contact between the

H_2O_2 and visible light. However, since the glycerol degradation percentage was substantially lower compared to the results obtained for the cases that involved $CuFe_2O_4$ loading from 0.1 to 5.0 g/L, it can therefore be concluded that semiconductor material such as $CuFe_2O_4$ also has concurrently absorbed light energy during the irradiation to produce electron-hole pair (Shahid et al., 2013) at the photocatalyst surface as in Eq. (4.6).



Subsequently, more hydroxyl radical ($\bullet OH$) was generated from H_2O_2 (as in Eq. (4.7)) and to some extent albeit minor, via the water molecules breakdown (Eq. (4.8)) and also through reaction between hydroxyl ion (OH^-) and hole (cf. Eq. (4.9)).



The final step would involve the attack of adsorbed glycerol substrate by the $\bullet OH$ radicals, most likely mineralized into simple molecules such as CO_2 and H_2 .

Based on the outlined photocatalytic Fenton mechanisms, the Langmuir-Hinshelwood (LH) model as shown in Eq. (4.10) can be employed to model the initial rate data as summarized earlier in Table 4.2.

$$\left(-r_{glycerol}^o\right) = \frac{k_{rxn} C_{glycerol} C_{H_2O_2}}{1 + K_{glycerol} C_{glycerol} + K_{H_2O_2} C_{H_2O_2}} \quad (4.10)$$

where

k_{rxn} = reaction rate constant

$K_{glycerol}$ = Adsorption constant for glycerol

$K_{H_2O_2}$ = Adsorption constant for H_2O_2

Once again, a non-linear regression of the initial rate data was performed using Polymath software in-built with Levenberg-Marquardt optimization method. The resulting parameter estimates are provided in Table 4.4 with reasonably excellent adherence to the LH Model ($R^2 = 0.93$). The glycerol adsorption constant ($K_{glycerol}$) was 1.010, which was larger than the adsorption constant belonging to the H_2O_2 reactant (0.033). This indicates that glycerol was chemisorbed onto the surface of $CuFe_2O_4$ before being attacked by the hydroxyl radical, whilst the H_2O_2 was predominantly present in the glycerol solution due to the much weaker chemisorption magnitude. Significantly, this is consistent with the mechanisms in Eq. (4.5) to (4.9) which posit that the breaking of H_2O_2 occurred without the need to chemisorb.

Table 4.4: Values of kinetic parameters Eq. (4.10)

Variable	Value	95% Confidence	R^2
k_{rxn}	2.60×10^{-4}	6.78×10^{-5}	
$K_{glycerol}$	1.010	0.0015	0.93
$K_{H_2O_2}$	0.033	1.13×10^{-4}	

The adequacy of Langmuir-Hinshelwood model may be seen from the parity plot in Figure 4.17. It shows a reasonably good agreement between predicted and observed specific rates.

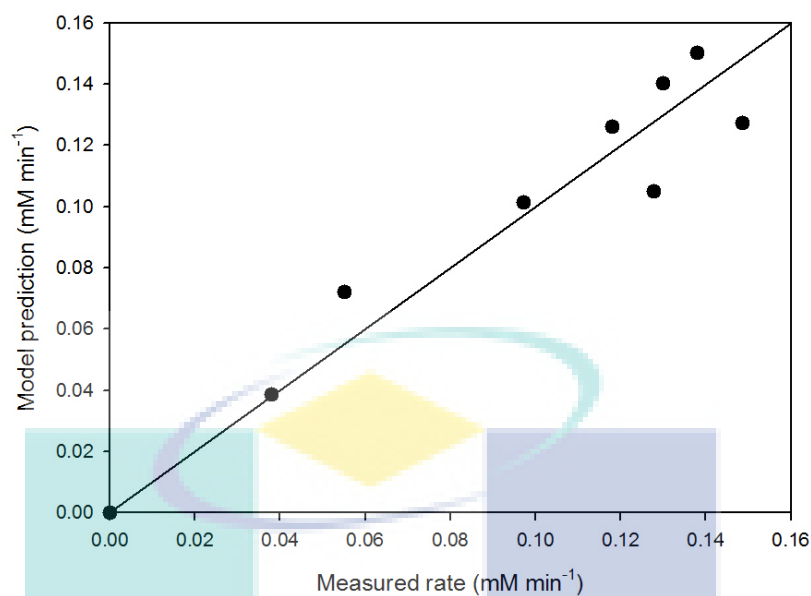


Figure 4.17: Parity plot showing the adequacy of Langmuir-Hinshelwood modelling

Furthermore, as the residual plot depicted in Figure 4.18 shows a random pattern, hence it can be safely assumed that the Langmuir-Hinshelwood model was sufficient to capture the degradation trend.

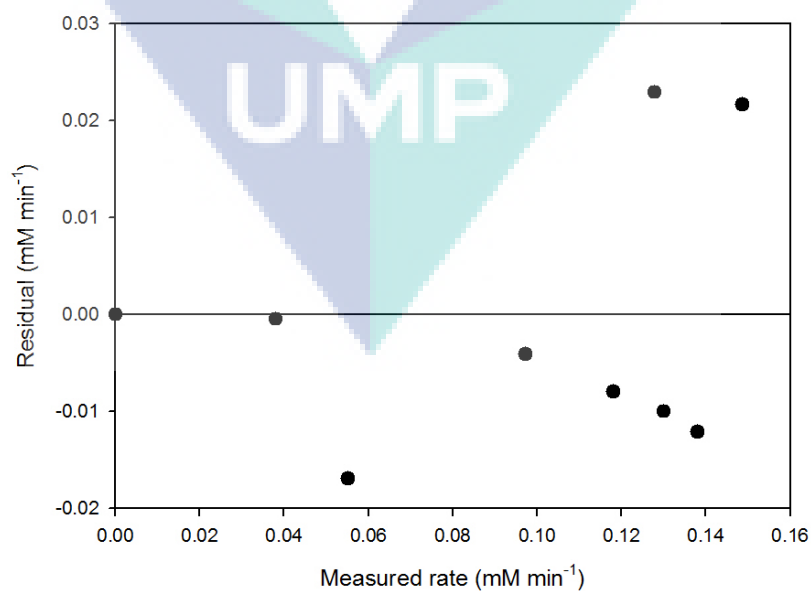


Figure 4.18: Residual plot showing random distribution of error

4.4 EXPERIMENTAL DESIGN ANALYSIS

4.4.1 Experimental Design Table

Experimental works based on the experimental design have been carried out and data obtained was summarized in Table 4.5. The response for the experimental design was the degradation rate of glycerol.

4.4.2 Factorial Analysis on Glycerol Degradation

Figure 4.19 shows the main effects of factors in Pareto chart by conferring t-value limit. According to the Pareto chart, effects above the t-value limit are considered 99% confidence level. It can be seen that H₂O₂ concentration demonstrates the most significant effect in this study. In contrast, effects below t-value limit are not likely to be significant. An effect is said to be positive when an increase in its level resulted in an increase in the response which coloured in orange while blue colour shows negative effect when increasing its level resulting response to be decrease.

4.4.3 Statistical Analysis and Analysis of Variance (ANOVA)

The model equation of this study in coded factor is shown in Eq. (4.11) while the ANOVA analysis is summarized in Table 4.6. The model with the selected terms was analyzed and found to be significant. The p-values were used as a tool to check the significance of each of the effect, which in turn may indicate the pattern of the interactions between the factors. The smaller the value of p, the more significant was the corresponding coefficient. P-value less than 0.05 indicate significant model terms and values greater than 0.05 indicate the model terms that are not significant.

$$\begin{aligned} \text{Degradation (\%)} = & 22.49 + 8.22 * A - 7.39 * B + 11.77 * C + 2.96 * D \\ & + 5.49 * A * C - 4.35 * B * C \end{aligned} \quad (4.11)$$

where

A = time

B = glycerol concentration

C = H₂O₂ concentration

D = CuFe₂O₄ photocatalyst loadings.

Table 4.5: Result in Experimental Design

Std	Factor 1	Factor 2	Factor 3	Factor 4	Response 1
	A:Time	B:Glycerol	C:H₂O₂	D:CuFe₂O₄	Degradation
	h	Concentration	Concentration	Photocatalyst	%
		mM	mM	g/L	
1	1	27.36	163.90	0.1	8.74
2	4	27.36	163.90	0.1	9.97
3	1	68.40	163.90	0.1	2.34
4	4	68.40	163.90	0.1	7.43
5	1	27.36	819.50	0.1	29.72
6	4	27.36	819.50	0.1	57.71
7	1	68.40	819.50	0.1	12.38
8	4	68.40	819.50	0.1	27.93
9	1	27.36	163.90	5	14.61
10	4	27.36	163.90	5	21.70
11	1	68.40	163.90	5	6.28
12	4	68.40	163.90	5	14.70
13	1	27.36	819.50	5	27.97
14	4	27.36	819.50	5	68.58
15	1	68.40	819.50	5	12.12
16	4	68.40	819.50	5	37.61

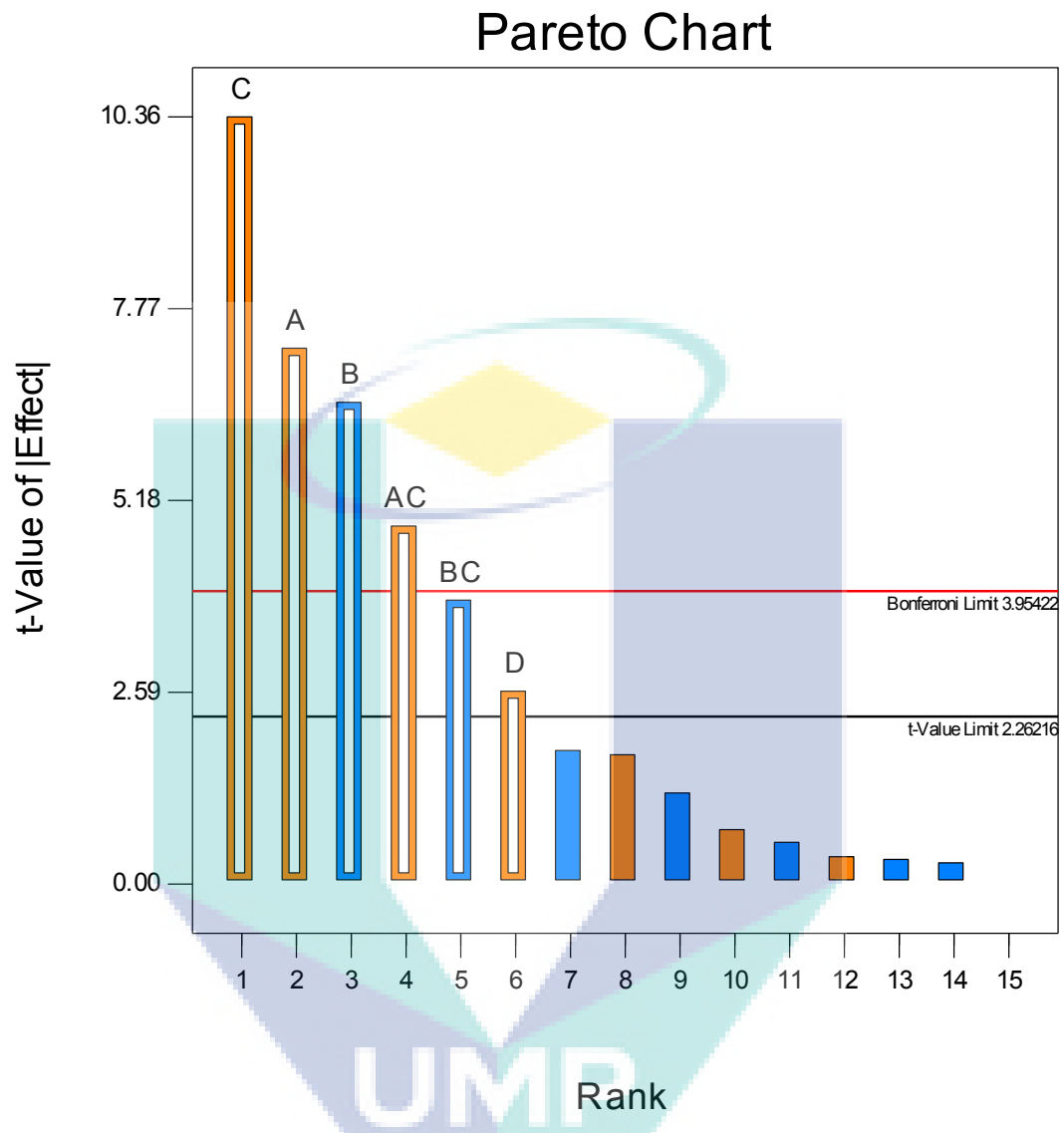


Figure 4.19: Pareto chart for t-value of effects

Table 4.6: ANOVA analysis of model

Source	Sum of Squares	df	Mean Square	F Value	p-value Prob > F	
Model	5094.099	6	849.0164	41.11545	< 0.0001	significant
A-time	1080.186	1	1080.186	52.31034	< 0.0001	
B-glycerol concentration	873.212	1	873.212	42.28717	0.0001	
C-H ₂ O ₂ concentration	2215.186	1	2215.186	107.2752	< 0.0001	
D-CuFe ₂ O ₄	140.0446	1	140.0446	6.781963	0.0285	
AC	482.2404	1	482.2404	23.35353	0.0009	
BC	303.2294	1	303.2294	14.68454	0.0040	
Residual	185.8461	9	20.64957			
Cor Total	5279.945	15				

The parameter such as the coefficient of determination (R^2), adjusted- R^2 , predicted- R^2 , coefficient of variance (CV), prediction residual error sum of squares (PRESS), adequate precision and the lack of fit test were used to determine the goodness of fit of a model. These parameter values can be taken from the ANOVA table. Table 4.7 summarizes the parameter used to test goodness of fit of the model.

Coefficient of determination (R^2) is the proportion of variation in the response due to the model and it suggested that R^2 for a good model should be close to one. The R^2 of 0.965 was obtained for the model, which is an indication of satisfactory result since the value is close to one. Addition of new variable to the model will affect the R^2 value. Therefore, adjusted R^2 is preferred to evaluate the model. To get a high degree correlation between actual and predicted values, the adjusted R^2 should be more than 90%. Adjusted R^2 of 94% was obtained for the model implying that all the selected term that are significant were included and non-significance were left out.

The coefficient of variation (CV) is the standard deviation expressed as a percentage of the mean and is calculated by dividing the standard deviation by the mean value and multiplying by 100. Generally, CV value should be less than 10% for a good fit to the model. The CV of this model is 20.2% which is higher than 10%.

The amount of variation in new data explained by the model is measured by predicted- R^2 . As a general rule, predicted- R^2 should be close to one for a good fit. Predicted- R^2 of 0.89 was obtained for this model.

Predicted Residual Error Sum of Squares (PRESS) value means an overall measurement of the discrepancy between the data and the estimation model. A good fit of the model should have smaller discrepancy. PRESS value 587.4 was obtained for this model.

The signal to noise ratio was measured by adequate precision test. A ratio greater than 4 is desirable. The adequate precision of this model is 20.181 indicates an adequate signal and this model can be used to navigate the design space.

Figure 4.20 shows the relationship between the predicted and experimental values for each response factor. The graph indicated that the predicted value were almost same as actual value.

Table 4.7: Parameter used to test goodness of fit of the model

Parameter	Value
Std. Dev.	4.54418
Mean	22.4858
CV %	20.20911
PRESS	587.3656
R-Squared	0.964801
Adj R-Squared	0.941336
Pred R-Squared	0.888755
Adeq Precision	20.18107

4.4.4 Response Surface of Glycerol Degradation

The interaction effects of factors upon the responses are depicted in the three-dimensional surface plots. Figure 4.21 shows the 3-D response surface plot of glycerol degradation at different function. The glycerol degraded faster as increasing the H₂O₂ concentration (Figure 4.21(a)). Degradation of glycerol shows higher degradation rate at 27.36 mM initial glycerol and 819.5 mM H₂O₂ (Figure 4.21(b)).

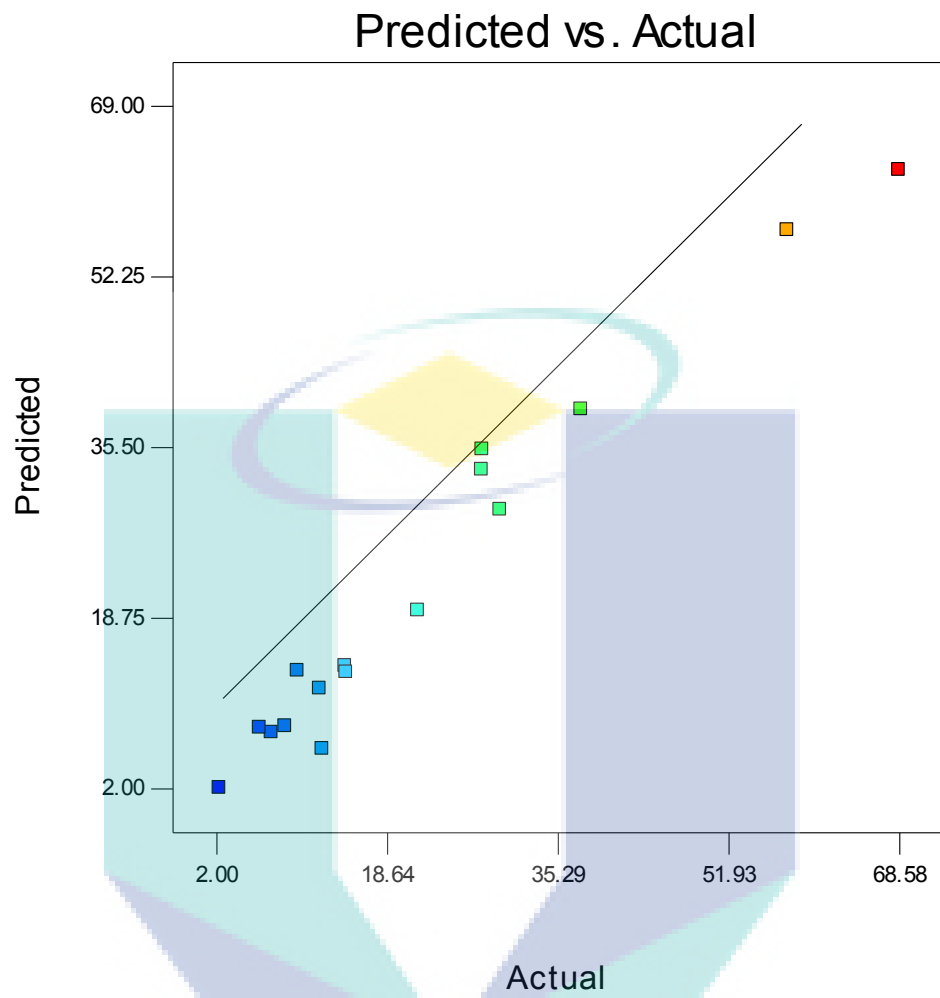


Figure 4.20: Comparison between predicted result and experimental result of factorial design

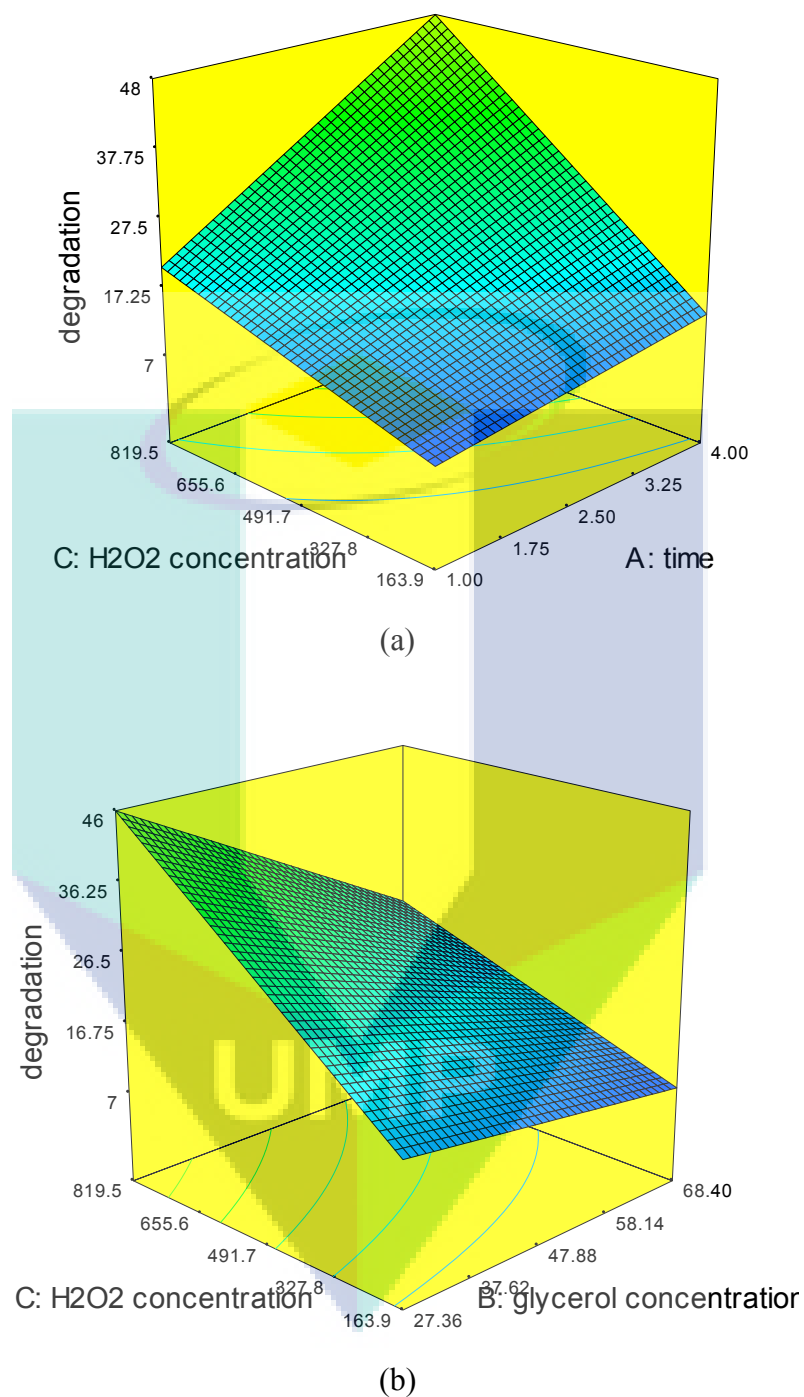


Figure 4.21: Response surface plot of glycerol degradation as a function of: (a) different H₂O₂ concentration and time at fixed initial glycerol concentration and photocatalyst loading; (b) different initial glycerol concentration and H₂O₂ concentration at fixed time and photocatalyst loading

4.4.5 Prediction of Best Point

The verification of the experimental data was carried out by calculating numerically with the developed model where the objective was to degrade the initial glycerol concentration. The best experimental conditions for factors in glycerol degradation were shown in Table 4.8. The experiment was performed according to the suggested experimental conditions as and result was presented in Table 4.9. Based on the predicted and experimental results presented, the experimental values were in good agreement with the predicted values proposed by the model with error from 0.07% to 0.4%.

Table 4.8: Suggested best condition of factor in glycerol degradation

Factors	Best Condition
A-Time	4 h
B-Glycerol concentration	27.41 mM
C-H ₂ O ₂ concentration	819.5 mM
D-CuFe ₂ O ₄	5.0 g/L

Table 4.9: Comparison between predicted and experimental value for best condition

Response	Experimental Value	Error
Glycerol degradation	62.3	0.51%
	62.2	0.68%
	62.0	1.00%
Predicted value	62.62	
Desirability	0.910	

CHAPTER 5

CONCLUSIONS AND RECOMMENDATIONS

5.1 CONCLUSIONS

From the catalyst characterization and photocatalytic Fenton reaction studies, several important conclusions can be drawn. The conclusions are written in bullet point format to directly provide the answers to the scopes of research. Therefore, the major conclusions are:

1. The CuFe_2O_4 photocatalyst prepared via sol-gel technique from showed significantly-improved photocatalytic Fenton activity towards the glycerol solution (27.0 to 68.5 mM) under the 250 W visible light irradiation.
2. Physicochemical characterization of the CuFe_2O_4 photocatalyst showed that the photocatalyst possessed BET specific surface area of $104.0 \text{ m}^2/\text{g}$. Interestingly, the rather large BET specific surface area was also corroborated by the FESEM images which showed porous structure. In addition, the XRD diffractogram showed that visible light-active component, CuFe_2O_4 , was successfully synthesized with crystallite size that ranged from 5.0 to 90.0 nm. Significantly, diffuse reflective UV-vis spectrum of CuFe_2O_4 confirmed that the band gap energy was 1.60 eV and falls under the visible light region.

3. The photocatalytic Fenton effects towards glycerol degradation were determined via HPLC measurements of glycerol samples pre- and post-experiments. It was determined from the blank run study that visible light was an integral part of the reaction. Without the visible light irradiation, glycerol degradation was low (< 4.0%). In contrast, when visible light was present, the glycerol degradation improved markedly to attain 17.7% after 4 h of visible light irradiation in the absence of CuFe_2O_4 photocatalyst. This can be attributed to the photo-activated splitting of H_2O_2 into hydroxyl ($\bullet\text{OH}$) radical. In the presence of CuFe_2O_4 photocatalyst, the photocatalytic Fenton degradation of glycerol improved substantially to record nearly 40.0% degradation at catalyst loading of 5.0 g/L. This has demonstrated that the CuFe_2O_4 under the visible light was capable of generating additional hydroxyl radicals to attack glycerol.
4. For the effects of initial concentration of reactants, it was found that the initial degradation rate of glycerol can be captured using both Power-Law modelling as well as Langmuir-Hinshelwood. Significantly, from the Power Law modelling, order of reaction with respect to the glycerol (0.20) and H_2O_2 (0.80) was found to be fractional, typical representation of chemical kinetics expression. Furthermore, via the Langmuir-Hinshelwood model, adsorption constant related to H_2O_2 was found to be much weaker compared to the adsorption constant of glycerol. This indicates that H_2O_2 splitting into hydroxyl radical occurred in the bulk phase, via direct attack by visible light irradiation whilst the glycerol substrate needs to chemisorb on the catalyst surface before being attacked by the hydroxyl radicals

5.2 RECOMMENDATIONS

Three recommendations are suggested for future works:

1. Some activity characterization with sophisticated spectroscopic technique i.e. FTIR, XRD is to be incorporated to determine the actual surface photocatalytic mechanism during Fenton degradation over the CuFe_2O_4 photocatalysts.
2. The effect of temperature was not investigated in the current study as the scopes of research only strictly covered the photocatalytic effect. However, temperature may influence the thermal catalytic aspect of the reaction and hence is to be recommended for future studies, i.e. at 40°C , 60°C and 80°C .
3. Different types of visible light responsive catalyst systems can be employed for testing with glycerol such as N-doped TiO_2 that has found increasing popularity.
4. Concentration of as-prepared glycerol solution can be further increased to mimic concentration of crude glycerol or to use crude glycerol in the photocatalytic Fenton degradation study.
5. To increase the ratios of Cu:Fe, i.e. 1:2, 1:3, 1:4 in the photocatalyst formulation to investigate its photodegradation ability.

REFERENCES

- Aazam, E. S. 2014. Photocatalytic oxidation of methylene blue dye under visible light by Ni doped Ag₂S nanoparticles. *Journal of Industrial and Engineering Chemistry*, **20**(6): 4033–4038.
- Aita, Y., Komatsu, M., Yin, S., and Sato, T. 2004. Phase-compositional control and visible light photocatalytic activity of nitrogen-doped titania via solvothermal process. *Journal of Solid State Chemistry*, **177**(9): 3235–3238.
- Alyamani, a, and Lemine, O. 2012. FE-SEM Characterization of Some Nanomaterial. *Intech*, (1): 463–472.
- Ameta, N., Sharma, J., Sharma, S., Kumar, S., and Punjabi, P. B. 2012. Copper modified iron oxide as heterogeneous photo-Fenton reagent for the degradation of coomase brilliant blue R-250. *Indian Journal of Chemistry - Section A Inorganic, Physical, Theoretical and Analytical Chemistry*, **51**: 943–948.
- askIITians. 2015. Glycerol or Glycerine. *Alcohols Phenols and Ethers*. Retrieved March 2, 2015, from <http://www.askitians.com/iit-jee-chemistry/organic-chemistry/glycerol.aspx>
- Augugliaro, V., El Nazer, H. a H., Loddo, V., Mele, a., Palmisano, G., Palmisano, L., and Yurdakal, S. 2010. Partial photocatalytic oxidation of glycerol in TiO₂ water suspensions. *Catalysis Today*, **151**(1-2): 21–28.
- Baldrian, P., Merhautová, V., Gabriel, J., Nerud, F., Stopka, P., Hrubý, M., and Beneš, M. J. 2006. Decolorization of synthetic dyes by hydrogen peroxide with heterogeneous catalysis by mixed iron oxides. *Applied Catalysis B: Environmental*, **66**(3-4): 258–264.
- Blake, D. M. 2001. *Bibliography of work on the heterogeneous photocatalytic removal of hazardous compounds from water and air*. Colorado.
- Brunauer, S., Emmett, P. H., and Teller, E. 1938. Adsorption of Gases in Multimolecular Layers. *Journal of the American Chemical Society*, **60**(2): 309–319.

- Bühler, W., Dinjus, E., Ederer, H. J., Kruse, a., and Mas, C. 2002. Ionic reactions and pyrolysis of glycerol as competing reaction pathways in near- and supercritical water. *Journal of Supercritical Fluids*, **22**(1): 37–53.
- Casbeer, E., Sharma, V. K., and Li, X. Z. 2012. Synthesis and photocatalytic activity of ferrites under visible light: A review. *Separation and Purification Technology*, **87**: 1–14.
- Cecil Instruments. 2006. Principles and applications of reflectance spectrophotometry. *LabPlus International*, (October): 0–2.
- Chacó, J. M., Leal, M. T., Sánchez, M., and Bandala, E. R. 2006. Solar photocatalytic degradation of azo-dyes by photo-Fenton process. *Dyes and Pigments*, **69**(3): 144–150.
- Chen, S.-Z., Zhang, P.-Y., Zhuang, D.-M., and Zhu, W.-P. 2004. Investigation of nitrogen doped TiO₂ photocatalytic films prepared by reactive magnetron sputtering. *Catalysis Communications*, **5**(11): 677–680.
- Ciriminna, R., Pina, C. Della, Rossi, M., and Pagliaro, M. 2014. Understanding the glycerol market. *European Journal of Lipid Science and Technology*, 1–8.
- Clean Correct. 2015. Nano-How it Works. Retrieved April 3, 2015, from <http://cleancorrect.com/products/nano-technology/nano-how-it-works/>
- Cong, Y., Zhang, J., Chen, F., and Anpo, M. 2007. Synthesis and characterization of nitrogen-doped TiO₂ nanophotocatalyst with high visible light activity. *Journal of Physical Chemistry C*, **111**(19): 6976–6982.
- Daskalaki, V. M., and Kondarides, D. I. 2009. Efficient production of hydrogen by photo-induced reforming of glycerol at ambient conditions. *Catalysis Today*, **144**(1-2): 75–80.
- Derbal, a., Omeiri, S., Bouguelia, a., and Trari, M. 2008. Characterization of new heterosystem CuFeO₂/SnO₂ application to visible-light induced hydrogen evolution. *International Journal of Hydrogen Energy*, **33**(16): 4274–4282.
- Diwald, O., Thompson, T. L., Zubkov, T., Goralski, E. G., Walck, S. D., and Tates, J. T. 2004. Photochemical Activity of Nitrogen-Doped Rutile TiO₂(110) in Visible Light. *The Journal of Physical Chemistry B*, **108**(19): 6004–6008.
- Domenech, X., Jardim, W. F., and Litter, I. M. 2001. Procesos Avanzados De Oxidación Para La Eliminación De Contaminantes. cap 01 do livro Eliminación de Contaminantes por Fotocatálisis Heterogénea, editado por Miguel A. Blesa (para CYTED).

- Ebraheem, S., and El-Saied, A. 2013. Band Gap Determination from Diffuse Reflectance Measurements of Irradiated Lead Borate Glass System Doped with TiO₂ by Using Diffuse Reflectance Technique. *Materials Sciences and Applications*, **04**(05): 324–329.
- Folger, H. S. 2008. *Elements of Chemical Reaction Engineering*. Prentice-Hall.
- Glaze, W. H., Kang, J.-W., and Chapin, D. H. 1987. The Chemistry of Water Treatment Processes Involving Ozone, Hydrogen Peroxide and Ultraviolet Radiation. *Ozone: Science & Engineering*.
- Gregg, F., and Goodwin, C. 2008. *SVO: Powering Your Vehicle With Straight Vegetable Oil*. New Society Publishers.
- Gregory, S. R. 1991. Properties of glycerine. In E. Jungermann & N. O. V. Sonntag (Eds.), *Glycerine: A Key Cosmetic Ingredient*. CRC Press.
- Guan, Y. H., Ma, J., Ren, Y. M., Liu, Y. L., Xiao, J. Y., Lin, L. Q., and Zhang, C. 2013. Efficient degradation of atrazine by magnetic porous copper ferrite catalyzed peroxy monosulfate oxidation via the formation of hydroxyl and sulfate radicals. *Water Research*, **47**(14): 5431–5438.
- Haque, M. M., Bahnemann, D., and Muneer, M. 2003. Photocatalytic Degradation of Organic Pollutants : Mechanisms and Kinetics, **3**.
- Hashimoto, K., Irie, H., and Fujishima, A. 2005. Photocatalysis: A Historical Overview and Future Prospects. *Japanese Journal of Applied Physics*, **44**(12): 8269–8285.
- Hudgins, R. R. 1972. A general criterion for avoiding film diffusion control in heterogeneous catalytic reaction. *The Canadian Journal of Chemical Engineering*, **50**(3): 427–430.
- Identity, I. C. 1995. Chemical Summary for Hydrogen Peroxide, (7722): 1–11.
- Jedsukontorn, T., Meeyoo, V., Saito, N., and Hunsom, M. 2015. Route of glycerol conversion and product generation via TiO₂-induced photocatalytic oxidation in the presence of H₂O₂. *Chemical Engineering Journal*, **281**: 252–264.
- Jones, C. W., and Clark, J. H. 1999. Introduction to the Preparation and Properties of Hydrogen Peroxide, 1–35.
- Kameyama, T. 2006. Robust Science & Technology for Safe and Secure Life Space-Photocatalyst. *AIST's Photocatalyst*.

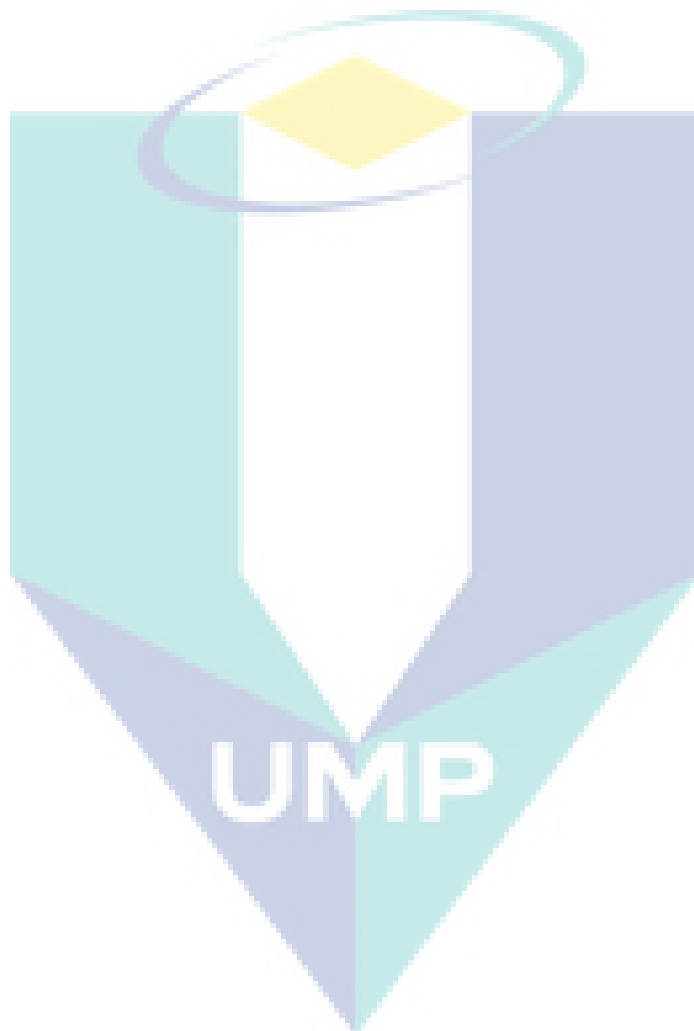
- Kommineni, S., Zoekler, J., Stocking, A., Liang, S., Flores, A., Rodriguez, R., ... Brown, A. 2011. Advanced Oxidation Processes. In *Treatment Technologies for the Removal of Methyl Tertiary Butyl Ether (MTBE) from Drinking Water: Air Stripping, Advanced Oxidation Processes, Granular Activated Carbon, Synthetic Resin Sorbents* (Vol. 32, pp. 377–408).
- Kumar, V., Masudi-Panah, S., Tan, C. C., Wong, T. K. S., Chi, D. Z., and K, D. G. 2013. Copper Oxide Based Low Cost Thin Film Solar Cells. *Ieee*, 443–445.
- Lam, M. K., Lee, K. T., and Mohamed, A. R. 2010. Homogeneous, heterogeneous and enzymatic catalysis for transesterification of high free fatty acid oil (waste cooking oil) to biodiesel: A review. *Biotechnology Advances*, **28**(4): 500–518.
- Lazić, Ž. R. 2004. *Design of Experiments in Chemical Engineering*. Weinheim, FRG: Wiley-VCH Verlag GmbH & Co. KGaA.
- Legrini, O., Oliveros, E., and Braun, A. 1993. Photochemical processes for water treatment. *Chemical Reviews*, **93**(2): 671–698.
- Li, L., Du, W., Liu, D., Wang, L., and Li, Z. 2006. Lipase-catalyzed transesterification of rapeseed oils for biodiesel production with a novel organic solvent as the reaction medium. *Journal of Molecular Catalysis B: Enzymatic*, **43**(1-4): 58–62.
- Liu, S. Q., Feng, L. R., Xu, N., Chen, Z. G., and Wang, X. M. 2012. Magnetic nickel ferrite as a heterogeneous photo-Fenton catalyst for the degradation of rhodamine B in the presence of oxalic acid. *Chemical Engineering Journal*, **203**: 432–439.
- Liu, Y., Koh, C. M. J., and Ji, L. 2011. Bioconversion of crude glycerol to glycolipids in *Ustilago maydis*. *Bioresource Technology*, **102**(4): 3927–3933.
- Lopes, P. a. L., Mascarenhas, A. J. S., and Silva, L. a. 2015. Sonochemical synthesis of Cd_{1-x}Zn_xS solid solutions for application in photocatalytic reforming of glycerol to produce hydrogen. *Journal of Alloys and Compounds*, **649**: 332–336.
- Mahmoodi, N. M. 2011. Photocatalytic ozonation of dyes using copper ferrite nanoparticle prepared by co-precipitation method. *Desalination*, **279**(1-3): 332–337.
- Mehrjouei, M. 2012. *Advanced oxidation processes for water treatment : Reactor design and case studies*. Brandenburgischen Technischen Universität.
- Meireles, B. a., and Pereira, V. L. P. 2013. Synthesis of bio-additives: Transesterification of ethyl acetate with glycerol using homogeneous or heterogeneous acid catalysts. *Journal of the Brazilian Chemical Society*, **24**(1): 17–25.

- Minero, C., Bedini, A., and Maurino, V. 2012. Glycerol as a probe molecule to uncover oxidation mechanism in photocatalysis. *Applied Catalysis B: Environmental*, **128**: 135–143.
- Mohamed, R. M., and Aazam, E. S. 2012. Photocatalytic Oxidation of Carbon Monoxide over NiO/SnO₂ Nanocomposites under UV Irradiation. *Journal of Nanotechnology*, **2012**: 1–9.
- Mota, a. L. N., Albuquerque, L. F., Beltrame, L. T. C., Chiavone-Filho, O., Machulek, a. J., and Nascimento, C. a. O. 2008. Advanced Oxidation Processes and Their Application in the Petroleum Industry: a Review. *Brazilian Journal of Petroleum and Gas*, **2**(3): 122–142.
- Nakata, K., and Fujishima, A. 2012. TiO₂ photocatalysis: Design and applications. *Journal of Photochemistry and Photobiology C: Photochemistry Reviews*, **13**(3): 169–189.
- Organization for Economic Cooperation and, and Development. 2002. *Screening Initial Data Set (SIDS) Initial Assessment Report For SIAM 14*.
- Pagliari, B. M., Rossi, M., and Pagliari, M. 2008. Glycerol: Properties and Production. In M. Rossi (Ed.), *Future of Glycerol New Usage for a Versatile Raw Material*.
- Panagiotopoulou, P., Karamerou, E. E., and Kondarides, D. I. 2013. Kinetics and mechanism of glycerol photo-oxidation and photo-reforming reactions in aqueous TiO₂ and Pt/TiO₂ suspensions. *Catalysis Today*, **209**: 91–98.
- Particle Analytical. 2015. Laser diffraction theory.
- Quispe, C. a G., Coronado, C. J. R., and Carvalho, J. a. 2013. Glycerol: Production, consumption, prices, characterization and new trends in combustion. *Renewable and Sustainable Energy Reviews*, **27**: 475–493.
- Ribeiro, A. R., Nunes, O. C., Pereira, M. F. R., and Silva, A. M. T. 2015. An overview on the advanced oxidation processes applied for the treatment of water pollutants defined in the recently launched Directive 2013/39/EU. *Environment International*, **75**: 33–51.
- Russell, M. 2012. Fats and Oil. Retrieved April 3, 2015, from http://mhchem.org/221/COTW/fats_and_oils/FatsANDOils.html
- Sadanandam, G., Lalitha, K., Kumari, V. D., Shankar, M. V., and Subrahmanyam, M. 2013. Cobalt doped TiO₂: A stable and efficient photocatalyst for continuous hydrogen production from glycerol: Water mixtures under solar light irradiation. *International Journal of Hydrogen Energy*, **38**(23): 9655–9664.

- Sakthivel, S. And Kisch, H. 2003. Photocatalytic and Photoelectrochemical Properties of Nitrogen-Doped Titanium Dioxide. *A European Journal of Chemical Physics and Physical Chemistry*, **4**: 487–490.
- Sano, T., Negishi, N., Koike, K., Takeuchia, K., and Matsuzawaa, S. 2004. Preparation of a visible light-responsive photocatalyst from a complex of Ti^{4+} with a nitrogen-containing ligand. *Journal of Materials Chemistry*, **14**: 380–384.
- Saponification. 2015. Retrieved from <http://nsb.wikidot.com/c-9-5-5-1>
- Sartale, S. D., Lokhande, C. D., and Muller, M. 2003. Electrochemical synthesis of nanocrystalline $CuFe_2O_4$ thin films from non-aqueous (ethylene glycol) medium. *Materials Chemistry and Physics*, **80**(1): 120–128.
- Sato, S. 1986. Photocatalytic activity of NO_x -doped TiO_2 in the visible light region. *Chemical Physics Letters*, **123**(1-2): 126–128.
- Sevas Educational Society. 2003. Glycerol Pollution Control & Safety. Retrieved April 2, 2015, from http://www.sbioinformatics.com/design_thesis/Glycerol/Glycerol_Pollution-2520control&Safety.pdf
- Shahid, M., Jingling, L., Ali, Z., Shakir, I., Warsi, M. F., Parveenf, R., and Nadeem, M. 2013. Photocatalytic degradation of methylene blue on magnetically separable $FePc/Fe_3O_4$ nanocomposite under visible irradiation. *Materials Chemistry and Physics*, **139**: 566–571.
- Sheldon, R. A. 2014. Green and sustainable manufacture of chemicals from biomass: state of the art. *Green Chemistry*, **16**: 950–963.
- Shen, Y., Wu, Y., Xu, H., Fu, J., Li, X., Zhao, Q., and Hou, Y. 2013. Facile preparation of sphere-like copper ferrite nanostructures and their enhanced visible-light-induced photocatalytic conversion of benzene. *Materials Research Bulletin*, **48**(10): 4216–4222.
- Shihong, X., Daolun, F., and Wenfeng, S. 2009. Preparations and photocatalytic properties of visible-light-active zinc ferrite-doped tio_2 photocatalyst. *Journal of Physical Chemistry C*, **113**(6): 2463–2467.
- Siles López, J. Á., Martín Santos, M. D. L. Á., Chica Pérez, A. F., and Martín Martín, A. 2009. Anaerobic digestion of glycerol derived from biodiesel manufacturing. *Bioresource Technology*, **100**(23): 5609–5615.
- Stojanović, Z., Marković, S., and Uskoković, D. 2010. Measurement of particle size distribution using laser light diffraction. *Tehnika-Novi Materijali*.

- Su, M., He, C., Sharma, V. K., Abou Asi, M., Xia, D., Li, X., ... Xiong, Y. 2012. Mesoporous zinc ferrite: Synthesis, characterization, and photocatalytic activity with H₂O₂/visible light. *Journal of Hazardous Materials*, **211-212**: 95–103.
- Tamalampudi, S., Talukder, M. R., Hama, S., Numata, T., Kondo, A., and Fukuda, H. 2008. Enzymatic production of biodiesel from Jatropha oil: A comparative study of immobilized-whole cell and commercial lipases as a biocatalyst. *Biochemical Engineering Journal*, **39**(1): 185–189.
- Tan, H. W., Abdul Aziz, a. R., and Aroua, M. K. 2013. Glycerol production and its applications as a raw material: A review. *Renewable and Sustainable Energy Reviews*, **27**: 118–127.
- The Soap and Detergent Association. 1990. *Glycerine: An Overview*. Glycerine & Oleochemical Division. Park Avenue South, New York.
- TitanPE Tech. (Shanghai) Inc. 2008. Mechanism of Photocatalysis. *TiPE™ Library*. Retrieved April 3, 2015, from <http://www.tipe.com.cn/library/kb2502.htm>
- U.S. Energy Information Administration. 2015. Frequently Asked Questions. *Monthly Energy Review*. Retrieved April 28, 2015, from <http://www.eia.gov/tools/faqs/faq.cfm?id=427&t=3>
- Wade, J. 2005. *An Investigation of TiO₂-ZnFe₂O₄ Nanocomposites for Visible Light Photocatalysis*. University of South Florida.
- Wang, Y., Zhao, H., Li, M., Fan, J., and Zhao, G. 2014. Magnetic ordered mesoporous copper ferrite as a heterogeneous Fenton catalyst for the degradation of imidacloprid. *Applied Catalysis B: Environmental*, **147**: 534–545.
- Wang, Z., Zhuge, J., Fang, H., and Prior, B. a. 2001. Glycerol production by microbial fermentation: A review. *Biotechnology Advances*, **19**(3): 201–223.
- Warren, B. E. 1969. *X-ray Diffraction*. Courier Corporation.
- Xu, L., and Wang, J. 2012. Magnetic nanoscaled Fe₃O₄/CeO₂ composite as an efficient fenton-like heterogeneous catalyst for degradation of 4-chlorophenol. *Environmental Science and Technology*, **46**(18): 10145–10153.
- Yang, F., Hanna, M., and Sun, R. 2012. Value-added uses for crude glycerol--a byproduct of biodiesel production. *Biotechnology for Biofuels*, **5**(13): 1–10.
- Yang, H., Yan, J., Lu, Z., Cheng, X., and Tang, Y. 2009. Photocatalytic activity evaluation of tetragonal CuFe₂O₄ nanoparticles for the H₂ evolution under visible light irradiation. *Journal of Alloys and Compounds*, **476**(1-2): 715–719.

- Yin, S., Yamaki, H., Zhang, Q., Komatsu, M., Wang, J., Tang, Q., ... Sato, T. 2004. Mechanochemical synthesis of nitrogen-doped titania and its visible light induced NO_x destruction ability. *Solid State Ionics*, **172**(1-4): 205–209.
- Yuan, Z., Wang, J., Wang, L., Xie, W., Chen, P., Hou, Z., and Zheng, X. 2010. Biodiesel derived glycerol hydrogenolysis to 1,2-propanediol on Cu/MgO catalysts. *Bioresource Technology*, **101**(18): 7088–7092.



APPENDIX A CATALYST PREPARATION

Sample calculation during the catalyst preparation as listed as below:

Metal = Cu ($M = 63.546 \text{ g mol}^{-1}$)

Metal salt used = $\text{Cu}(\text{NO}_3)_2 \cdot 3\text{H}_2\text{O}$ ($M = 241.60 \text{ g mol}^{-1}$)

Basis = 20 g of photocatalst

Weigh of $\text{Cu}(\text{NO}_3)_2 \cdot 3\text{H}_2\text{O}$ salt required

$$= 20 \text{ g} \times 241.60 \text{ g mol}^{-1} / 63.446 \text{ g mol}^{-1} = 76.14 \text{ g}$$

Metal = Fe ($M = 55.845 \text{ g mol}^{-1}$)

Metal salt used = $\text{Fe}(\text{NO}_3)_3 \cdot 9\text{H}_2\text{O}$ ($M = 404.00 \text{ g mol}^{-1}$)

Basis = 20 g of photocatalst

Weigh of $\text{Fe}(\text{NO}_3)_3 \cdot 9\text{H}_2\text{O}$ salt required

$$= 20 \text{ g} \times 404.00 \text{ g mol}^{-1} / 55.845 \text{ g mol}^{-1} = 144.67 \text{ g}$$

The image contains a large, semi-transparent watermark of the UMP logo. The logo is a shield-like shape composed of several overlapping triangles in shades of teal, light blue, and yellow. The letters 'UMP' are printed in a bold, white, sans-serif font across the bottom center of the shield.

UMP

APPENDIX B

HPLC CALIBRATION

Figure B.1 shows the typical HPLC chromatogram that was obtained from the HPLC analysis. It shows that the peak at retention time of 3.150 min was H₂O, at retention time of 3.930 min was H₂O₂ and at retention time of 4.643 min was C₃H₈O₃. Generally, the peak elution was excellent as complete separation between peaks can be obtained and that the Gaussian-alike peaks with flat baseline were recorded. Consequently, this has demonstrated the validity of the current HPLC analysis.

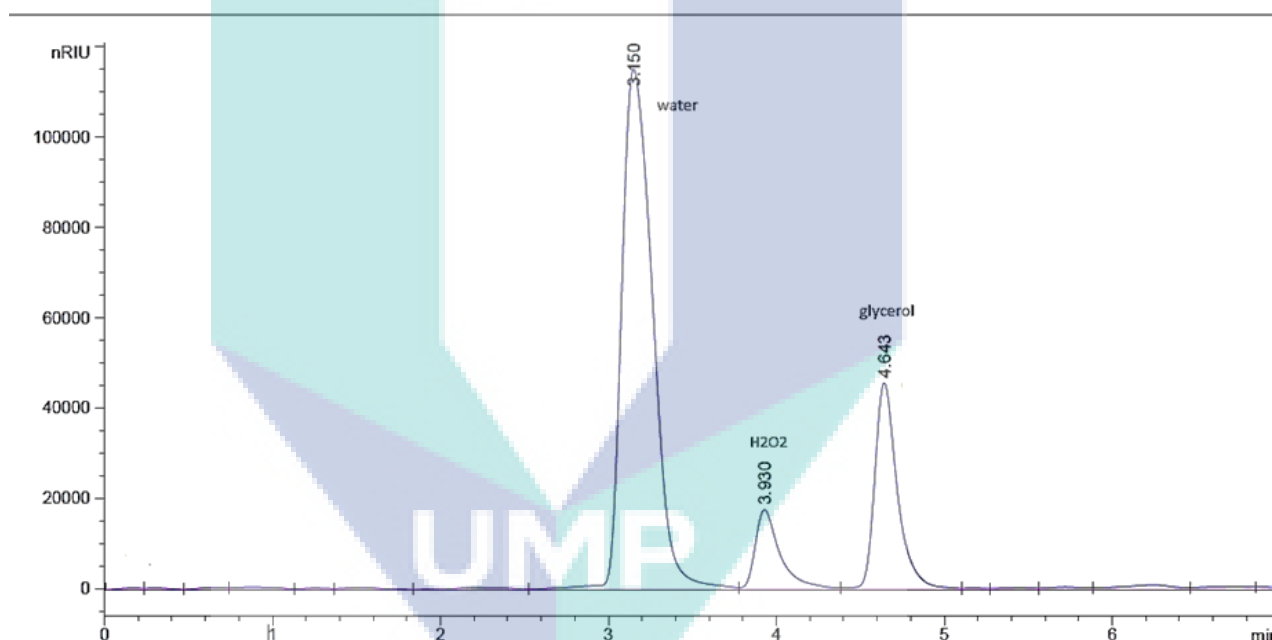


Figure B.1: PLC chromatogram obtained from the HPLC instrument

Moreover, before the commencement of reaction studies, the standard calibration curves for both glycerol and H₂O₂ were obtained. For C₃H₈O₃ solution, the concentration employed for the standard samples were ranged between 27.36 and 68.41 mM, as shown in Figure B.2(a). It is to be noted that the choice of lower limit concentration of C₃H₈O₃ solution (27.36 mM) was solely due to the detection limit of HPLC instrument.

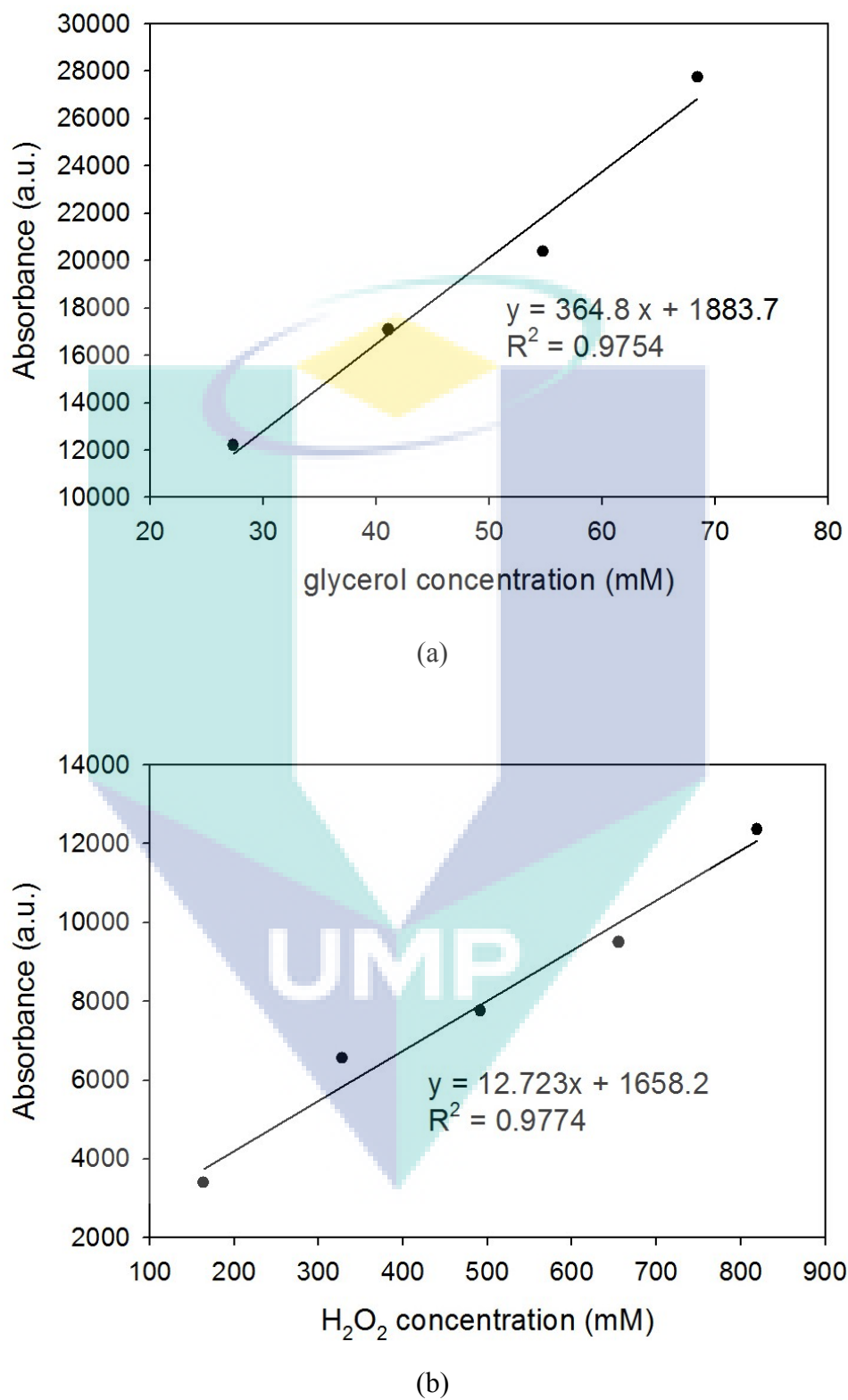
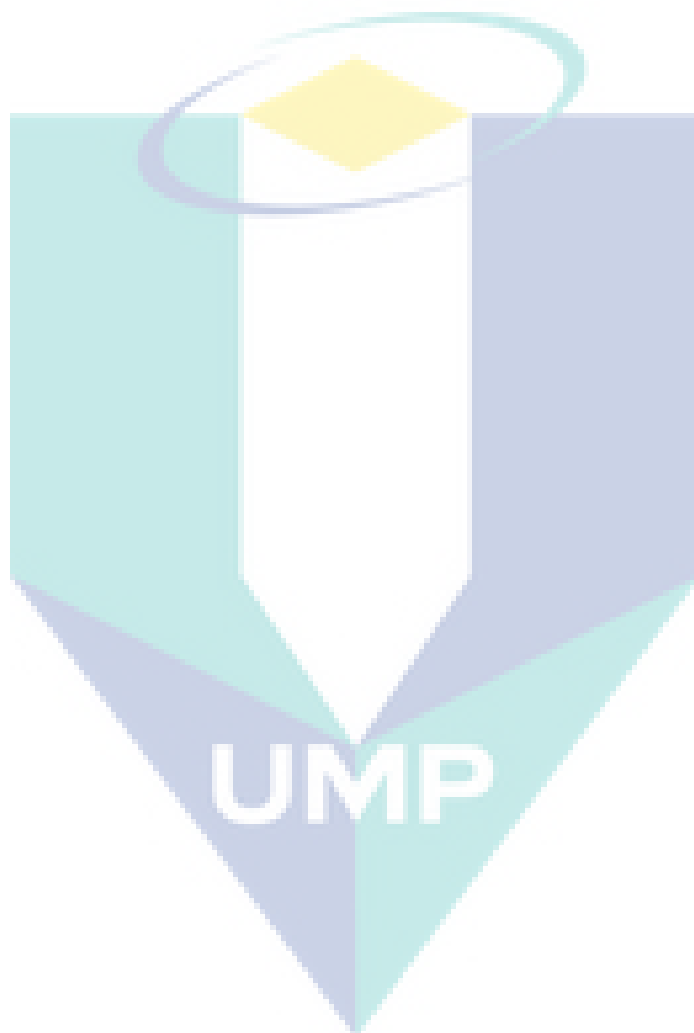


Figure B.2: Standard calibration curves for (a) C₃H₈O₃ solution and (b) H₂O₂ solution

For H₂O₂ standard calibration curve (cf. Figure **Error! Reference source not found**.B.2 (a)), as can be observed, a good linearity can be obtained in terms of response factor (HPLC signal as a function of H₂O₂ concentration) with $R^2 = 0.98$.



APPENDIX C
BET REPORT

Table C.1: Data from BET surface analyser

Adsorption Data		Desorption Data	
p/p^0	V_{ads} (cm ³ /g)	p/p^0	V_{ads} (cm ³ /g)
6.40E-05	1.9641	0.9978	131.97
0.00012	8.1508	0.9903	124.37
0.0025	13.787	0.9773	118.59
0.0178	17.313	0.9581	113.72
0.0599	20.7	0.9316	109.95
0.1161	23.782	0.8956	106.8
0.1767	26.702	0.8469	103.5
0.2385	29.618	0.7934	100.28
0.2982	32.557	0.7393	97.091
0.3576	35.674	0.6921	92.722
0.4172	39.203	0.6596	86.856
0.4775	43.456	0.6391	81.217
0.533	48.362	0.6234	76.242
0.5868	54.503	0.6088	71.238
0.6381	62.344	0.5961	66.911
0.6847	71.764	0.5826	62.742
0.7275	81.768	0.5652	58.24
0.768	89.939	0.5466	53.911
0.8124	95.731	0.521	49.652
0.8631	100.2	0.4892	45.714
0.9163	104.7	0.4467	41.734
0.9624	110.57	0.3979	38.225
0.9834	116.61	0.3456	35.16
0.9982	122.63	0.292	32.396
0.9998	129.35	0.2365	29.657
1	137.89	0.1807	27.015
		0.1297	24.578

Surface Area (B.E.T.) 2 Parameters Line

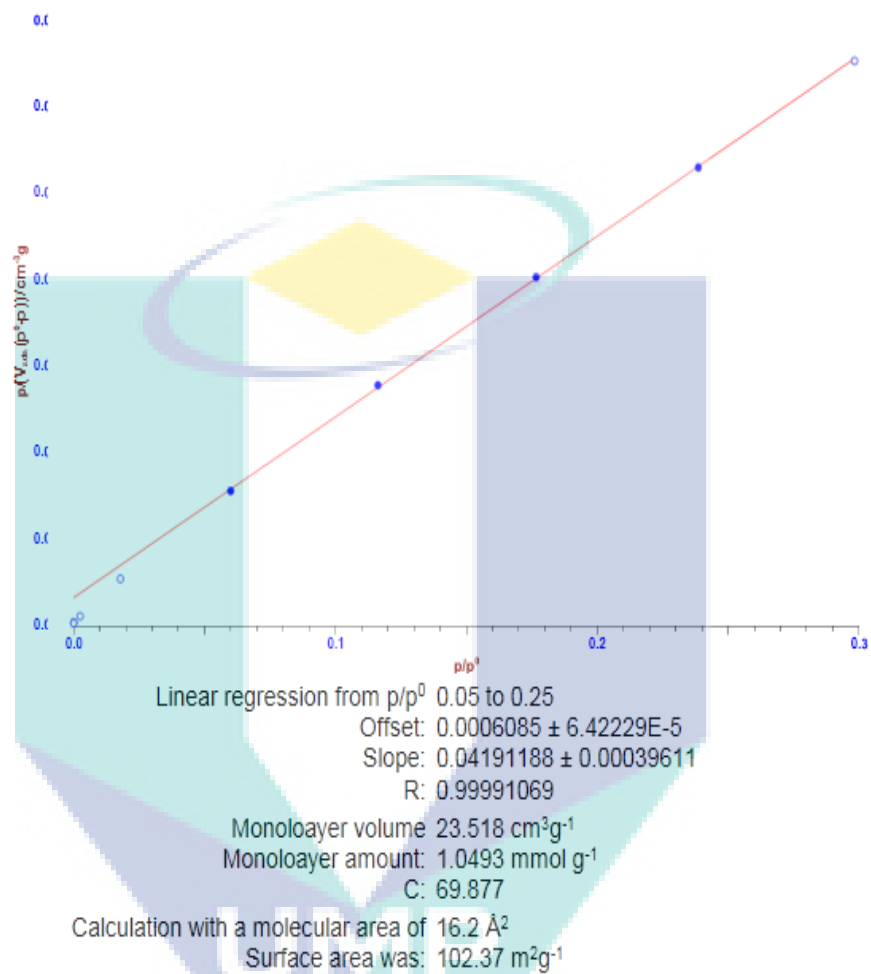


Figure C.1. Surface Area (B.E.T.) 2 Parameter Line

APPENDIX D
MASTERSIZER REPORT

Table D.1: Data from Mastersizer Analysis Report

Size (μm)	Volume (%)	Size (μm)	Volume (%)	Size (μm)	Volume (%)
0.02	0	1.002	0.2	50.238	3.48
0.022	0	1.125	0.3	56.368	4.08
0.025	0	1.262	0.37	63.246	4.66
0.028	0	1.416	0.44	70.963	5.1
0.032	0	1.589	0.5	79.621	5.39
0.036	0	1.783	0.56	89.337	5.48
0.04	0	2	0.6	100.237	5.39
0.045	0	2.244	0.64	112.468	5.13
0.05	0	2.518	0.67	126.191	4.71
0.056	0	2.825	0.7	141.589	4.14
0.063	0	3.17	0.73	158.866	3.46
0.071	0	3.557	0.76	178.25	2.7
0.08	0	3.991	0.78	200	1.93
0.089	0	4.477	0.8	224.404	1.24
0.1	0	5.024	0.81	251.785	0.68
0.112	0	5.637	0.82	282.508	0.32
0.126	0	6.325	0.82	316.979	0.16
0.142	0	7.096	0.82	355.656	0.2
0.159	0	7.962	0.82	399.052	0
0.178	0	8.934	0.82	447.744	0
0.2	0	10.024	0.84	502.377	0
0.224	0	11.247	0.87	563.677	0
0.252	0	12.619	0.92	632.456	0
0.283	0	14.159	1	709.627	0
0.317	0	15.887	1.09	796.214	0
0.356	0	17.825	1.2	893.367	0
0.399	0	20	1.31	1002.374	0
0.448	0	22.44	1.42	1124.683	0
0.502	0	25.179	1.52	1261.915	0
0.564	0	28.251	1.63	1415.892	0
0.632	0	31.698	1.8	1588.656	0
0.71	0	35.566	2.04	1782.502	0
0.796	0	39.905	2.41	2000	0
0.893	0.13	44.774	2.89		

APPENDIX E
XRD REPORT

Table E.1: XRD Data

2-theta (deg)	d (ang.)	Height (cps)	Int. I (cps/deg)	FWHM (deg)	Size	Phase name
18.56(8)	4.78(2)	15(4)	6.4(8)	0.27(8)	312(88)	copper ferrite, (1,0,1)
30.082(16)	2.9682(16)	25(5)	17.3(10)	0.51(4)	170(14)	copper ferrite, (1,1,2)
33.30(2)	2.6883(17)	53(7)	13.4(7)	0.226(17)	383(29)	Unknown
34.82(5)	2.575(3)	29(5)	19.8(16)	0.62(5)	141(11)	copper ferrite, (1,0,3)
36.03(3)	2.4910(19)	83(9)	73(3)	0.80(3)	109(4)	copper ferrite, (2,1,1)
37.27(4)	2.411(3)	23(5)	3.6(6)	0.15(4)	588(148)	copper ferrite, (2,0,2)
38.87(7)	2.315(4)	17(4)	8.3(12)	0.45(6)	195(26)	Unknown
54.23(5)	1.6900(15)	37(6)	11.4(13)	0.24(6)	396(100)	copper ferrite, (3,1,2)
62.25(5)	1.4901(11)	31(6)	31.3(16)	0.75(5)	129(9)	copper ferrite, (2,2,4)

APPENDIX F
EXPERIMENTAL DATA

Table F.1: Experimental glycerol concentration-time data of different photocatalyst loadings at 68.4 mM glycerol concentration and 819.5 mM H₂O₂ concentration

Time	blank	0.1 g/L	1.0 g/L	2.0 g/L	5.0 g/L
0	68.42	68.42	68.42	68.42	68.42
15	67.03528144	65.09101553	65.35917467	58.29234917	65.03887456
30	65.68451606	63.57822965	62.23190492	57.53054217	62.4875484
45	66.00752191	60.63318447	60.10489575	56.25169587	58.99196609
60	64.64969547	59.944888	59.13528452	54.78357311	60.12359504
90	62.9497833	56.54562316	56.30294607	52.57773216	55.48058609
120	61.60097097	54.93449151	54.86928841	50.48113262	51.10108962
150	59.73444788	52.81488462	51.54447723	50.20829511	48.09461465
180	58.38473415	53.13480296	50.45117455	47.34668023	47.0595902
240	56.27633226	49.30288286	47.30130949	44.84122936	42.67811471

Table F.2: Experimental glycerol degradation rate-time data of different photocatalyst loadings at 68.4 mM glycerol concentration and 819.5 mM H₂O₂ concentration

Time	blank	0.1 g/L	1.0 g/L	2.0 g/L	5.0 g/L
0	0	0	0	0	0
15	2.023850564	4.865513697	4.473582771	14.80217894	4.941720894
30	3.998076497	7.07654246	9.044278109	15.91560629	8.670639583
45	3.525983764	11.38090548	12.15303165	17.78471811	13.77964617
60	5.510529864	12.38689272	13.57017755	19.93046899	12.12570149
90	7.995055103	17.35512547	17.70981282	23.15443998	18.91174205
120	9.966426522	19.70989256	19.80519086	26.21874799	25.31264305
150	12.69446378	22.80782721	24.66460504	26.61751664	29.70678946
180	14.66715267	22.34024706	26.26253354	30.7999412	31.21954078
240	17.74871053	27.94083183	30.86625331	34.46181034	37.62333425

Table F.3: Experimental H₂O₂ concentration-time data of different photocatalyst loadings at 68.4 mM glycerol concentration and 819.5 mM H₂O₂ concentration

Time	blank	0.1 g/L	1.0 g/L	2.0 g/L	5.0 g/L
0	819.5	819.5	819.5	819.5	819.5
15	808.6011229	800.3862306	797.8068654	781.4495713	788.4475015
30	804.5906973	805.5241051	762.2499813	755.0842041	761.279446
45	794.5044393	781.5634595	755.0388154	724.6598743	769.8213294
60	788.2066414	766.5911286	724.8784443	720.6121562	753.0161323
90	791.9951017	733.280185	726.9173116	698.0370518	697.5045305
120	785.8929344	725.0497133	698.7238349	669.795277	655.7797976
150	767.5901946	688.7990763	652.7191048	673.394822	621.3023742
180	756.6725069	705.9482555	641.6628234	652.4334082	593.3097539
240	754.0992131	642.2932308	607.5070448	614.594471	534.1099661

Table F.4: Experimental H₂O₂ consumption rate-time data of different photocatalyst loadings at 68.4 mM glycerol concentration and 819.5 mM H₂O₂ concentration

Time	blank	0.1 g/L	1.0 g/L	2.0 g/L	5.0 g/L
0	0	0	0	0	0
15	1.329942294	2.332369669	2.647118312	4.643127355	3.789200545
30	1.819316987	1.705417318	6.985969331	7.860377781	7.104399516
45	3.050098931	4.629230078	7.86591636	11.57292565	6.062070847
60	3.818591648	6.456238119	11.5462545	12.06685098	8.112735533
90	3.356302421	10.52102685	11.29746045	14.82159221	14.88657346
120	4.100923201	11.5253553	14.73778708	18.26781244	19.97806009
150	6.334326467	15.94886196	20.35154303	17.82857571	24.18518924
180	7.66656414	13.85622263	21.70069269	20.38640535	27.60100624
240	7.980571917	21.62376683	25.86857294	25.00372531	34.82489737

Table F.5: Experimental glycerol concentration-time data of different initial H₂O₂ concentration at 68.4 mM glycerol concentration and 0.1 g/L CuFe₂O₄ loadings

Time	163.9 mM	327.8 mM	491.7 mM	655.6 mM	819.5 mM
0	68.4	68.4	68.4	68.4	68.4
15	68.92281076	66.71225594	66.24087235	65.88045607	65.07198863
30	67.85199839	66.25936202	65.23076058	64.54071307	63.55964496
45	66.75263667	65.80945064	65.12095585	62.8978398	60.61546065
60	66.80695017	64.71613478	63.26056443	60.72471435	59.92736538
90	65.50022041	62.17840516	60.30421917	57.76776236	56.52909418
120	64.89766252	64.8243101	59.21918795	55.57785136	54.91843349
150	65.00897844	61.57154004	58.08581997	53.20654456	52.79944619
180	64.35342449	61.74194479	56.96205357	54.17207241	53.11927101
240	63.32956006	60.81285562	55.79500759	52.95189333	49.28847103

Table F.6: Experimental glycerol degradation rate-time data of different initial H₂O₂ concentration at 68.4 mM glycerol concentration and 0.1 g/L CuFe₂O₄ loadings

Time	163.9 mM	327.8 mM	491.7 mM	655.6 mM	819.5 mM
0	0	0	0	0	0
15	-0.764343219	2.467462072	3.156619376	3.68354375	4.865513697
30	0.801171938	3.129587686	4.633390963	5.642232353	7.07654246
45	2.408425916	3.787352859	4.793924203	8.044093859	11.38090548
60	2.329020222	5.385767861	7.513794687	11.22117786	12.38689272
90	4.239443845	9.095898884	11.83593689	15.54420707	17.35512547
120	5.120376431	5.227616809	13.42223983	18.74583135	19.70989256
150	4.957633865	9.983128597	15.07921057	22.21265415	22.80782721
180	5.916046063	9.733998846	16.72214391	20.80106373	22.34024706
240	7.412923882	11.09231635	18.42835148	22.58495128	27.94083183

Table F.7: Experimental H₂O₂ concentration-time data of different initial H₂O₂ concentration at 68.4 mM glycerol concentration and 0.1 g/L CuFe₂O₄ loadings

Time	163.9 mM	327.8 mM	491.7 mM	655.6 mM	819.5 mM
0	163.9	327.8	491.7	655.6	819.5
15	162.4750024	324.1514258	485.0562671	644.091066	800.3862306
30	162.0591265	322.6838422	483.6514781	643.37701	805.5241051
45	161.3211897	320.1414035	481.4205832	631.878025	781.5634595
60	162.2541568	314.690291	466.5337244	622.195748	766.5911286
90	152.0726887	299.6184609	449.394905	594.967853	733.280185
120	149.3527227	295.7977114	438.149282	587.95074	725.0497133
150	148.0563666	289.467466	423.3262686	566.499922	688.7990763
180	143.3033672	280.5161095	415.2309681	556.7933	705.9482555
240	145.6193186	272.5744284	398.0045613	518.822587	642.2932308

Table F.8: Experimental H₂O₂ consumption rate-time data of different initial H₂O₂ concentration at 68.4 mM glycerol concentration and 0.1 g/L CuFe₂O₄ loadings

Time	163.9 mM	327.8 mM	491.7 mM	655.6 mM	819.5 mM
0	0	0	0	0	0
15	0.869431096	1.113048881	1.351176107	1.75548105	2.332369669
30	1.123168707	1.560755895	1.636876533	1.8643975	1.705417318
45	1.573404683	2.336362558	2.09058711	3.61836108	4.629230078
60	1.004175237	3.999301099	5.11821754	5.09521848	6.456238119
90	7.216175283	8.597174836	8.603842794	9.24834452	10.52102685
120	8.875703068	9.762748187	10.8909331	10.3186791	11.5253553
150	9.666646372	11.69387859	13.90557889	13.5906159	15.94886196
180	12.56658499	14.42461577	15.55196906	15.0711866	13.85622263
240	11.15355793	16.84733727	19.0554075	20.8629367	21.62376683

Table F.9: Experimental glycerol concentration-time data of different initial glycerol concentration at 0.1 g/L CuFe₂O₄ loadings and 819.5 mM H₂O₂ concentration

Time	27.36 mM	41.05 mM	54.73 mM	68.41 mM
0	27.36	41.05	54.73	68.41
15	23.5843457	37.6694562	50.5116621	65.0815021
30	23.0509904	35.9637459	48.5852516	63.5689373
45	21.3169579	34.8077633	47.6376697	60.6243226
60	19.230893	33.4096682	46.4438417	59.9361267
90	16.3319574	30.7610021	43.9719795	56.5373587
120	14.9114648	28.7725823	41.654542	54.9264625
150	14.9880713	26.7598026	40.05835	52.8071654
180	12.5144342	25.4294984	37.562755	53.127037
240	11.5687259	22.3846006	36.663933	49.2956769

Table F.10: Experimental glycerol degradation rate-time data of different initial glycerol concentration at 0.1 g/L CuFe₂O₄ loadings and 819.5 mM H₂O₂ concentration

Time	27.36 mM	41.05 mM	54.73 mM	68.41 mM
0	0	0	0	0
15	13.7999061	8.23518592	7.70754237	4.8655137
30	15.749304	12.3903875	11.227386	7.07654246
45	22.0871422	15.2064231	12.9587617	11.3809055
60	29.7116483	18.6122578	15.1400664	12.3868927
90	40.3071734	25.0645503	19.6565331	17.3551255
120	45.4990323	29.9084475	23.8908423	19.7098926
150	45.2190375	34.8116868	26.8073268	22.8078272
180	54.2601091	38.0523792	31.367157	22.3402471
240	57.7166452	45.4699132	33.0094409	27.9408318

Table F.11: Experimental H₂O₂ concentration-time data of different initial glycerol concentration at 0.1 g/L CuFe₂O₄ loadings and 819.5 mM H₂O₂ concentration

Time	27.36 mM	41.05 mM	54.73 mM	68.41 mM
0	819.5	819.5	819.5	819.5
15	808.029592	796.033632	809.742773	800.386231
30	801.293971	786.226192	802.171809	805.524105
45	769.666473	778.771056	781.733952	781.56346
60	780.847549	794.025816	752.549912	766.591129
90	730.116416	726.791428	766.186816	733.280185
120	702.178838	729.156569	748.532289	725.049713
150	693.215137	681.251046	715.334327	688.799076
180	686.197017	691.263149	694.153231	705.948256
240	642.141444	640.936823	686.881863	642.293231

Table F.12: Experimental H₂O₂ consumption rate-time data of different initial glycerol concentration at 0.1 g/L CuFe₂O₄ loadings and 819.5 mM H₂O₂ concentration

Time	27.36 mM	41.05 mM	54.73 mM	68.41 mM
0	0	0	0	0
15	1.39968369	2.86349818	1.19063171	2.33236967
30	2.22160213	4.06025723	2.11448338	1.70541732
45	6.08096733	4.96997481	4.6084256	4.62923008
60	4.71658952	3.10850319	8.1696263	6.45623812
90	10.9070878	11.3128215	6.50557459	10.5210268
120	14.3161881	11.0242136	8.65987928	11.5253553
150	15.4099894	16.8699151	12.7108813	15.948862
180	16.2663799	15.6481819	15.2955179	13.8562226
240	21.6422887	21.7892834	16.1828111	21.6237668

APPENDIX G
CALCULATION FOR EXTERNAL MASS TRANSFER

Density of water solution = 999.94 kg m^{-3}

From experimental work employing catalyst loading of 0.1 g/L , the catalyst bed density should be equals to $\rho_b = 0.1 \text{ kg m}^{-3}$

$$\rho_c = 5240 \text{ kg m}^{-3}$$

$$\rho_b = (1 - \varepsilon)\rho_c$$

$$\varepsilon = 0.999$$

$$\varepsilon J_D = \frac{0.765}{\text{Re}^{0.82}} + \frac{0.365}{\text{Re}^{0.386}}, \text{ As such } J_D = 0.0313$$

$$\text{Sc} = \frac{u}{\rho_g D_{AB}}$$

Estimation of D_{AB} using Wilke-Chang equation (dilute liquid phase) for $\text{C}_3\text{H}_8\text{O}_3$ - H_2O system:

$$D_{AB} = 1.173 \times 10^{-16} (\phi M_B)^{1/2} \frac{T}{\mu_B V_A^{0.6}}$$

where

$$T = 298 \text{ K}$$

$$\phi = 2.6 \text{ (Association parameter of the solvent (water) = 2.6 for water in Geankoplis)}$$

$$V_A = 0.0962 \text{ (From Table 6.3-2 of Geankoplis textbook)}$$

$$M_B = 18.0 \text{ (for H}_2\text{O)}$$

$$D_{AB} = 1.10 \times 10^{-9} \text{ m}^2 \text{ s}^{-1}$$

Therefore, the $\text{Sc} = 813.0$

$$k_c = 9.88 \times 10^{-4} \text{ m s}^{-1}$$

Hudgins criterion, normally n is less than 3, the maximum. n is the overall reaction order.

$$\frac{-r_{\text{exp}} \rho_b d_p |n|}{k_c C_{Ab}} < 0.3$$

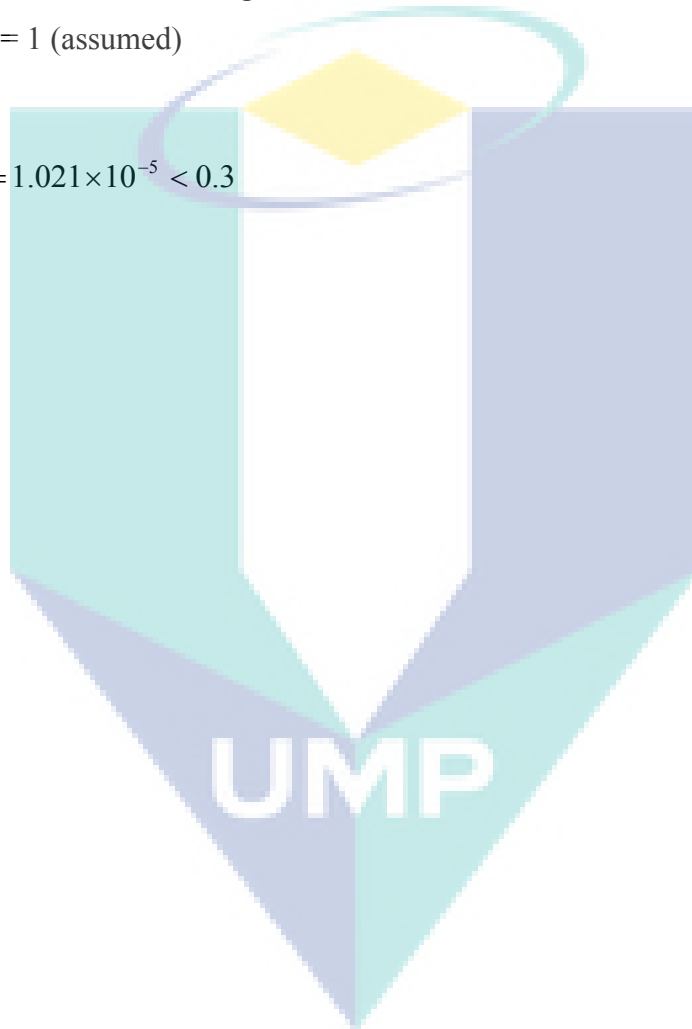
$$\text{So, } C_{Ab} = 0.06841 \text{ kmol m}^{-3}$$

$$-r_{\text{exp}} = 2.3007 \times 10^{-5} \text{ kmol kg}^{-1} \text{ s}^{-1}$$

$$\text{Rxn } |n| = 1 \text{ (assumed)}$$

So,

$$\frac{r_{\text{exp}} \rho_b d_p |n|}{k_c C_{Ab}} = 1.021 \times 10^{-5} < 0.3$$



APPENDIX H

CALCULATION FOR INTERNAL MASS TRANSFER

Weisz-Prater Criterion:

The extent of pore diffusion limitation may be neglected provided that the following Weisz-Prater criterion is fulfilled :

$$\frac{-r_A \rho_b R^2}{D_e C_{As}} < 1$$

C_{AS} is surface concentration. However, since it is proven that external mass transfer is negligible, $C_{AS} = C_{Ab}$

$$-r_{\text{exp}} = 2.3007 \times 10^{-5} \text{ kmol kg}^{-1} \text{ s}^{-1}$$

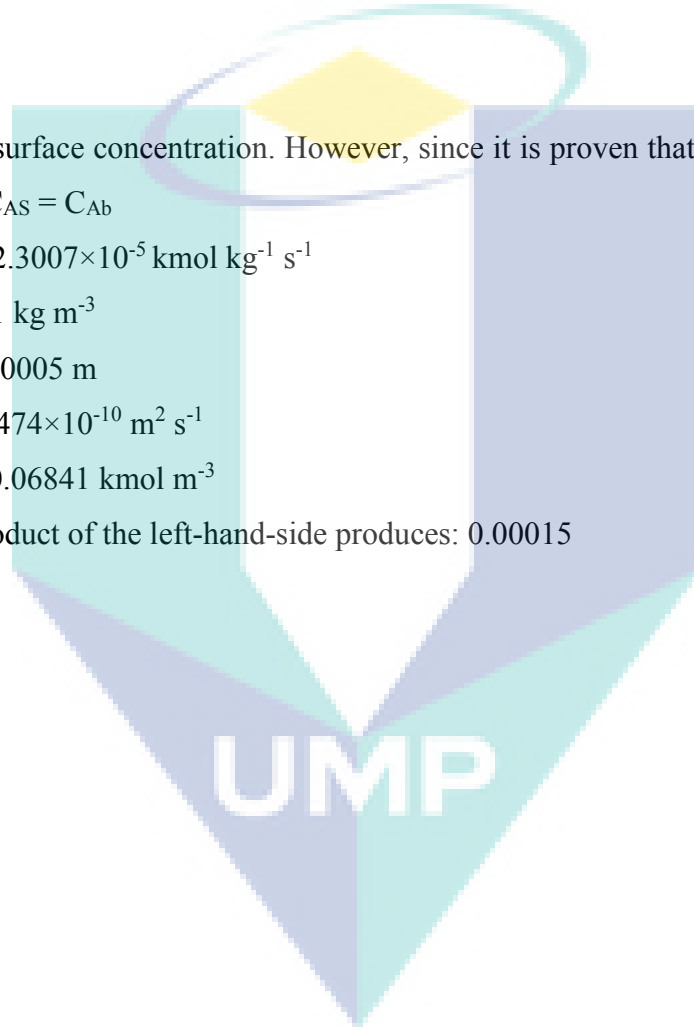
$$\rho_b = 0.1 \text{ kg m}^{-3}$$

$$R = 0.00005 \text{ m}$$

$$D_e = 5.474 \times 10^{-10} \text{ m}^2 \text{ s}^{-1}$$

$$C_{AS} = 0.06841 \text{ kmol m}^{-3}$$

The product of the left-hand-side produces: 0.00015



APPENDIX I

PUBLICATIONS AND CONFERENCES

Journals:

1. Ng, K. H., Deraman, M. R., Ang, C. H., Chong, S. K., Kong, Z. Y., Khan, M. R. and Cheng, C. K. (2014). Photo-treatment of palm oil mills effluent (POME) over Cu/TiO₂ photocatalyst. *Bulletin of Chemical Reaction Engineering & Catalysis*, 9(2), 2014, 121-127.
2. Kong, Z. Y., Wong, N. X., Lum, S. W., Tan, S. Z., Khan, R. and Cheng, C. K. (2014). The application of magnesium ferrite photocatalyst for photo treatment of methylene blue. *Procedia Engineering*.

Conferences:

1. Ng, K. H., Kong, Z. Y., Ang, C. H., Chong, S. K. and Cheng, C. K. (2014). Photo-treatment of palm oil mills effluent (POME) over Cu/TiO₂ photocatalyst. *Proceeding of the 23rd International Symposium on Chemical Reaction Engineering and 7th Asia-Pacific Chemical Reaction Engineering Symposium (ISCRE23 & APCRE7)*, 7-10 September 2014, Centara Grand and Bangkok Convention Centre, Bangkok, Thailand.
2. Ang, C. H., Kong, Z. Y., Ng, K. H., Chong, S. K. and Cheng, C. K. (2014). A study into the photoreaction of glycerol aqueous solution. *Proceeding of the 23rd International Symposium on Chemical Reaction Engineering and 7th Asia-Pacific Chemical Reaction Engineering Symposium (ISCRE23 & APCRE7)*, 7-10 September 2014, Centara Grand and Bangkok Convention Centre, Bangkok, Thailand.

3. Kong, Z. Y., Wong, N. X., Lum, S. W., Tan, S. Z., Khan, M. R. and Cheng, C. K. (2014). The application of magnesium ferrite photocatalyst for photo treatment of methylene blue. Proceeding of the 27th Symposium of Malaysian Chemical Engineers in Conjunction with 21th Regional Symposium on Chemical Engineering (SOMChE & RSCE 2014), 29-30 October 2014, Taylor's University Lakeside Campus, Subang, Malaysia.
4. Kong, Z. Y., Wong, N. X., Khan M. R. and Cheng, C. K. (2014). The application of magnesium ferrite photocatalyst for photo treatment of POME. Proceeding of the National Conference for Postgraduate research (NCON-PGR 2015), 24-25 January 2015, Universiti Malaysia Pahang, Gambang, Malaysia.

